RUPRECHT-KARLS-UNIVERSITÄT HEIDELBERG

Thomas Berndt

Exclusive Pomeron- and Odderon Induced Photoproduction of ω- and f_2 Mesons at HERA

Dissertation

HD-KIP-01-22

KIRCHHOFF-INSTITUT FÜR PHYSIK

Dissertation

submitted to the

Combined Faculties for the Natural Sciences and for Mathematics

of the Ruperto - Carola - University of Heidelberg, Germany,

for the degree of

Doctor of Natural Sciences

presented by

Diplom–Physiker: Thomas Berndt
born in: Mannheim

Oral examination: 5^{th} December, 2001

Exclusive Pomeron- and Odderon Induced Photoproduction of ω- and f_2 Mesons at HERA

Referees: Prof. Dr. Karlheinz Meier
Prof. Dr. Hans Günter Dosch

Abstract

The topics of this thesis are the analyses of exclusive photoproduction of ω- and f_2-mesons at mean γp centre of mass energies of $\langle W \rangle \approx 200$ GeV at HERA.
The former process is thought to be induced by photon-Pomeron interactions, and its cross section is measured to be $\sigma(\gamma p \to \omega p) = (1.3 \pm 0.2(\text{stat}) \pm 0.2(\text{syst}))\,\mu\text{b}$, where the decay $\omega \to \pi^0\gamma \to 3\gamma$ is used to analyse the events. The diffractive slope b describing the exponential fall of $\mathrm{d}\sigma/\mathrm{d}|t| \propto \exp(-b|t|)$ is measured by analysing the acceptance corrected differential distribution $\mathrm{d}N/\mathrm{d}|t|$. The value found for this parameter amounts to $b = (10.7 \pm 1.1(\text{stat}) \pm 2.0(\text{syst}))\,\text{GeV}^{-2}$. The corrected differential cross section $\mathrm{d}\sigma/\mathrm{d}|t|$ is also found to be in accordance with the prediction of the Stochastic Vacuum Model for ρ^0-photoproduction scaled by a factor of 2/9. The decay angular distributions $\mathrm{d}N/\mathrm{d}\cos\vartheta^*$ and $\mathrm{d}N/\mathrm{d}\varphi^*$ are found to be compatible with s-channel helicity conservation.
The predictions of the Stochastic Vacuum Model for Odderon induced f_2-photoproduction of 21 nb cannot be confirmed, but a 95 % confidence level upper limit on the cross section of $\sigma(\gamma p \to f_2 X) < 12.4\,\text{nb}$ is given. The contributions of the f_2 are looked for in the $\pi^0\pi^0$ mass spectrum, where the f_2 is thought to contribute via its decay $f_2 \to \pi^0\pi^0 \to 4\gamma$.

Zusammenfassung

Thema dieser Arbeit ist die Analyse exklusiver Photoproduktion der Mesonen ω und f_2 bei einer mittleren γp-Schwerpunktsenergie von $\langle W \rangle \approx 200$ GeV bei HERA.
Von ersterem Prozeß wird angenommen, daß er durch Photon-Pomeron Wechselwirkung vermittelt wird. Für den entsprechenden Wirkungsquerschnitt wird $\sigma(\gamma p \to \omega p) = (1.3 \pm 0.2(\text{stat}) \pm 0.2(\text{syst}))\,\mu\text{b}$ gemessen, wobei der Zerfall $\omega \to \pi^0\gamma \to 3\gamma$ zur Analyse der Ereignisse verwendet wird. Die logarithmische Steigung b, die den exponentiellen Abfall $\mathrm{d}\sigma/\mathrm{d}|t| \propto \exp(-b|t|)$ des differentiellen Wirkungsquerschnitts charakterisiert, wird durch die Analyse der akzeptanzkorrigierten differentiellen Verteilung $\mathrm{d}N/\mathrm{d}|t|$ gemessen. Der Wert, der für diesen Parameter gefunden wird, beträgt $b = (10.7 \pm 1.1(\text{stat}) \pm 2.0(\text{syst}))\,\text{GeV}^{-2}$. Für den korrigierten differentiellen Wirkungsquerschnitt $\mathrm{d}\sigma/\mathrm{d}|t|$ wird auch Übereinstimmung mit einer Vorhersage des Modell des Stochastischen Vakuums für ρ^0-Photoproduktion gefunden, wobei diese mit einem Faktor 2/9 versehen wird. Für die Zerfallswinkelverteilungen $\mathrm{d}N/\mathrm{d}\cos\vartheta^*$ und $\mathrm{d}N/\mathrm{d}\varphi^*$ wird Verträglichkeit mit s-Kanal-Helizitätserhaltung gefunden.
Die Vorhersage des Modells des Stochastischen Vakuums von 21 nb für Odderon-induzierte f_2-Photoproduktion kann nicht bestätigt werden, sondern es wird auf einem Konfidenz-Niveau von 95 % eine obere Grenze für den Wirkungsquerschnitt von $\sigma(\gamma p \to f_2 X) < 12.4\,\text{nb}$ angegeben. Die Beiträge des f_2's werden im $\pi^0\pi^0$-Massenspektrum gesucht, in dem das f_2 über seinen Zerfall $f_2 \to \pi^0\pi^0 \to 4\gamma$ beitragen soll.

Contents

List of Figures

List of Tables

Introduction

The subject of this thesis is the analysis of exclusive photoproduction of the mesons ω and f_2 at HERA using the H1 detector. Both mesons are analysed in purely photonic final states, namely $\omega \to \pi^0\gamma \to 3\gamma$ and $f_2 \to \pi^0\pi^0 \to 4\gamma$, respectively, and thus allow for a good measurement of the energies of the decay-products in the H1-backward electromagnetic calorimeter SpaCal. The former analysis stands in a long tradition of experiments and the latter is an (interim) completion of searches performed by the H1-group at the Kirchhoff-Institut für Physik.

The tradition of vector meson photoproduction goes back to end of last century's sixties. As the theory of strong interactions was lacking in these times phenomenological prescriptions were used to describe the data. The main ingredients of this phenomenology have been Regge theory and vector meson dominance. This has not changed since the advent of QCD as microscopic theory of strong interactions, because QCD is not applicable in these reactions since the strong coupling constant is in general not small enough for the perturbation series to converge. Though in some cases perturbation theory can be applied, when either some hard scale is present, or in the case when heavy mesons are involved the mass sets the scale. For these cases it has been possible to obtain a prescription of the processes based on perturbative QCD and allows to some extend to link the concepts used in Regge theory with the fundamental degrees of freedom of QCD, namely gluons.

Regge theory has been very successful in describing the behaviour of cross sections by the notion of the exchange of trajectories, which are attributed to specific particles. But one of these trajectories cannot be associated with any known particle, and this Pomeron trajectory – as it is called – was introduced to describe the rise of the cross section at large energies. It is commonly believed that the Pomeron is associated with gluonic degrees of freedom and thus one anticipates glue-balls to lie on this trajectory. In a similar way, a further trajectory was introduced with odd C-parity as opposed to the Pomeron which is even under C-parity, and therefore this trajectory was named Odderon.

In contrast to the Pomeron that rests on solid experimental and to some extend also on theoretical grounds, the Odderon has not been observed in soft processes so far, though in perturbative QCD both the Odderon and the Pomeron appear equally, respectively as the exchange of three and two gluons.

In this context this thesis is settled: The ω is thought to be produced by Pomeron induced γp interaction and the f_2 by Odderon induced reactions. And the picture sketched in the previous paragraph is confirmed anew. The Pomeron process is confirmed within the expectations of Regge theory and vector meson dominance, in contrast to the Odderon where only a limit on the cross section for exclusive f_2 photoproduction can be given.

This work is a further piece in the mosaic drawn by the various measurements and phenomenological prescriptions of soft QCD. And the hope is that the sum of all the pieces somewhen may give a picture, where the whole is more than just the sum of its parts.

In the first chapter the physics background is sketched and some phenomenological models are briefly discussed. The second chapter gives a short description of the H1 detector. The third chapter is concerned with the basic event selection, the strategy of the trigger and how it is simulated and the reconstruction of the kinematic variables used in the analyses presented. Before the actual analyses a chapter describing the Monte Carlo models used to describe the expected signals and background sources is included as chapter four. The following two chapters present the analyses of the ω and the f_2 meson, where in chapter five the cross section for exclusive ω-photoproduction at a mean photon-proton centre of mass energy of 200 GeV is measured, the differential cross section $\mathrm{d}\sigma/\mathrm{d}|t|$ for events in the ω-mass region is fitted to determine the diffractive slope and it is compared to a prediction of the Stochastic Vacuum Model. This is followed by fitting the decay angular distributions with the expectations of s-channel helicity conservation. Before summarising this chapter a discussion of the systematic uncertainties is given. The next chapter is concerned with the exclusive photoproduction of f_2-mesons mediated by Odderon exchange. The structure of this analysis is analogous to the one presented in the previous chapter, but no cross section can be measured, but a limit on the production is derived instead. This work closes with a summary of the findings of this thesis and combines them with the results obtained in [1, 2, 3]. There, also conclusions are drawn and some questions are raised. Perspectives and possibilities of how to gain more insight in the future are given.

Chapter 1

Physics Background

1.1 Kinematics

At HERA electrons[1] are scattered off protons having four-momenta of

$$k = (27.55, 0, 0, -27.55)\,\text{GeV} \quad ; \quad p = (820, 0, 0, 820)\,\text{GeV}\,, \tag{1.1}$$

respectively[2], defining the z-direction of H1 coordinate system as the direction of flight of the incoming proton. Here and in the following units are used where $\hbar = c = 1$.

For single photon exchange kinematics at HERA can be fully described by the invariants s, x, y and Q^2, defined as

$$\begin{aligned} s &= (k+p)^2 && (1.2)\\ Q^2 &= -q^2 = -(k-k')^2 && (1.3)\\ x &= \frac{Q^2}{2\,kp} && (1.4)\\ y &= \frac{pq}{kq}\,, && (1.5) \end{aligned}$$

where $\sqrt{s} = 301$ GeV is the centre of mass energy, x is the Bjorken scaling variable, giving the longitudinal momentum fraction of the parton in the proton that enters the interaction with the exchanged vector boson. The other variable introduced by Bjorken is y, called inelasticity, as in the rest frame of the proton it gives the relative amount of energy transferred from the electron on the proton. Both x and y are restricted to values $\in [0, 1]$. If $x = 1$ the scattering occurs elastically. The virtuality Q^2 is a measure of the off-shellness of the exchanged boson and can be interpreted as a measure of the strength of the interaction. By means of the Heisenberg uncertainty principle Q^2 is related to the resolution, i.e. a photon can resolve distances down to $d \sim 1/\sqrt{Q^2}$.

Often a further variable is used: the centre of mass energy squared of the system consisting of the exchanged boson and the proton,

$$W^2 = (q+p)^2\,. \tag{1.6}$$

Kinematics gets more complicated, if aside from the boson on the lepton side, a further boson from the proton side is emitted – be it another photon, a gluon or something else.

[1] In the following the term electron is also used for positron for simplicity.

[2] In 1998 the proton energy was increased to 920 GeV.

Then, a further variable describing the four-momentum transfer is introduced in analogy to the virtuality Q^2, but referring to the proton vertex:

$$t = (p - p')^2 . \tag{1.7}$$

In the case where only one boson is exchanged, $t = q^2 = -Q^2$.

The four variables s, x, y and Q^2 defined in equations (1.2) – (1.5) are not independent of each other, but obey the relation

$$Q^2 = xys , \tag{1.8}$$

where masses have been neglected.

In the analyses presented in chapters 5 and 6 the variable Σ will be exploited, which is defined as

$$\Sigma = \sum_i p_i^0 - p_i^3 = \sum_i p_i^- = \sum_i (E - p_z)_i , \tag{1.9}$$

where the sum runs over all particles i in the final state. The upper indices denote Lorentz-indices according to the notation used in [4] and the superscript '$-$' indicates the minus-component of the respective light-cone vector. Due to energy-momentum conservation its value is twice the electron beam energy, namely 55 GeV as in the initial state, where the corresponding sum runs over the electron and proton only.

$$\Sigma \equiv \Sigma(\text{final state}) = \Sigma(\text{initial state}) = \underbrace{(k^0 - k^3)}_{55\,\text{GeV}} + \underbrace{(p^0 - p^3)}_{0} = 55\,\text{GeV} , \tag{1.10}$$

where in the last step equation (1.1) was inserted.

1.2 Electron Proton Scattering

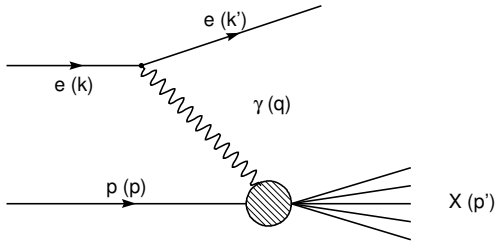

Figure 1.1: *A schematic diagram of the scattering of an electron off a proton.*

The lowest order diagram of electron-proton scattering (ep-scattering for short) is shown in figure 1.1, where the incoming electron emits a virtual photon with four-momentum $q = k - k'$, that subsequently interacts with the proton, indicated by the blob. The scattering may proceed elastically where the proton remains intact or inelastically where it emerges into an N particle final state X with $m_X^2 = (p + q)^2 = (\sum_{n=1}^{N} p_n)^2 \equiv W^2$. Following [4] one can write down the general structure of the total cross section as:

$$\left.\frac{\mathrm{d}^2\sigma(ep \to eX)}{\mathrm{d}E'_e\,\mathrm{d}\Omega}\right|_{\text{Lab}} = \frac{4\pi\alpha^2}{q^4} L_{\mu\nu} W^{\mu\nu} , \tag{1.11}$$

with the fine structure constant $\alpha = e^2/4\pi$, and where $L^{\mu\nu}$ and $W^{\mu\nu}$ denote the leptonic and hadronic tensor, respectively.

$$L^{\mu\nu} = \frac{1}{2}\sum_{s,s'} \langle e|j^\mu|e'\rangle\langle e'|j^\nu|e\rangle \tag{1.12}$$

$$W^{\mu\nu} = \frac{1}{4\pi m_p}\sum_N \left[\frac{1}{2}\sum_s \left\{\prod_{n=1}^{N}\int \mathrm{d}\Gamma_n \sum_{s_n} \langle p|J^\mu|X_n\rangle\langle X_n|J^\nu|p\rangle\right\}\right] \times (2\pi)^2\delta(p + q - p') \tag{1.13}$$

The following conventions were used: $|e\rangle$ ($|e'\rangle$) denotes the incoming (outgoing) electron with momentum k and spin s (k' and s', respectively). The leptonic current j^μ is given by

$$j^\mu = e\bar{u}(k',s')\gamma^\mu u(k,s)\,, \tag{1.14}$$

with spinors u, $\bar{u}$ for incoming and outgoing electron, respectively. The structure of the hadronic tensor is similar, but more general, namely all possible final states X_n are summed up. Therefore the sum over the spins is split and done for each of the N particle final states. In analogy to the leptonic tensor the incoming state is denoted by $|p\rangle$ with momentum p and spin s, and the final state by $|X_n\rangle$ with momentum $p' = \sum_{n=1}^{N} p_n$ and spins s_n. The phase space integration is carried out over the Lorentz invariant phase space element $\prod_{n=1}^{N} \mathrm{d}\Gamma_n$ with $\mathrm{d}\Gamma_n = \frac{\mathrm{d}^3\boldsymbol{p}_n}{(2\pi)^2 p_n^0}$. For the hadronic transition current an analogous construction as in equation. (1.14) is possible only for the elastic case, i.e. $\sum |X_n\rangle = |p',s'\rangle$, then J^μ can be written as

$$J^\mu = e\bar{u}(p',s')\Gamma^\mu u(p,s) \quad \text{with} \quad \Gamma^\mu = F_1(q^2)\gamma^\mu + \frac{\kappa}{2m_p}F_2(q^2)\sigma^{\mu\nu}q_\nu\,, \tag{1.15}$$

and $\sigma^{\mu\nu} = [\gamma^\mu, \gamma^\nu]$, and where F_1 and F_2 are the form factors of the proton, related to the charge and magnetic moment distributions, respectively, via Fourier transformations.

In the case of inelastic scattering, there is no simple analogy, but a more general form of the hadronic tensor $W^{\mu\nu}$ has to be constructed out of the independent momenta p and q and the metric tensor $g^{\mu\nu}$. The most general ansatz that one is led to involves four terms made up of $g^{\mu\nu}$ and products of p and q and scalar functions $W_i(\nu, q^2)$ with $\nu = pq/\ m_p$. Employing current conservation the number of independent terms can be reduced to two:

$$W^{\mu\nu} = W_1\left(\frac{q^\mu q^\nu}{q^2} - g^{\mu\nu}\right) + W_2\frac{1}{m_p^2}\left(p^\mu - \frac{pq}{q^2}q^\mu\right)\left(p^\nu - \frac{pq}{q^2}q^\nu\right)\,. \tag{1.16}$$

Combining all, one can write the cross section for the three cases: (1) elastic scattering off a structureless proton (Dirac proton) (2) elastic scattering of a real proton and (3) inelastic scattering in a generic form:

$$\left.\frac{\mathrm{d}^2\sigma(ep\to X)}{\mathrm{d}E_e'\,\mathrm{d}\Omega}\right|_{\mathrm{Lab}} = \frac{4\alpha^2 E_e'^2}{q^4}\left(A_i\cos^2\vartheta/2 + 2B_i\sin^2\vartheta/2\right)\,, \tag{1.17}$$

where an energy conserving $\delta\left(\nu - \frac{q^2}{2m_p}\right)$ has to be multiplied in the case of elastic scattering. The coefficients A_i and B_i are listed in table 1.1

For the inelastic case it is common to rewrite the cross section (1.17) differential in terms of the invariants x and Q^2 instead of E_e' and Ω and to replace the W_i by the structure functions[3] F_i:

$$m_p W_1(\nu,q^2) \to F_1(x,Q^2) \quad \text{and} \quad \nu W_2(\nu,q^2) \to F_2(x,Q^2)\,. \tag{1.18}$$

The cross section (1.17) then becomes

$$\frac{\mathrm{d}^2\sigma(ep\to X)}{\mathrm{d}x\,\mathrm{d}Q^2} = \frac{4\pi\alpha^2}{xQ^4}\left[y^2 xF_1(x,Q^2) + (1-y)F_2(x,Q^2)\right] \tag{1.19}$$

$$= \frac{2\pi\alpha^2}{xQ^4}\left[(1+(1-y)^2)F_2(x,Q^2) - y^2F_L(x,Q^2)\right]\,, \tag{1.20}$$

[3] not to be confused with the dipole form factors F, which depend on q^2 only, but not on q^2 *and* x.

i	A_i	B_i
1	1	τ
2	$\frac{G_E^2 + \tau G_M^2}{1+\tau}$	τG_M^2
3	$W_1(\nu, q^2)$	$W_2(\nu, q^2)$
	with $\tau = -q^2/4m_p^2$	

Table 1.1: The coefficients A_i and B_i for the three types of *ep*-scattering: *The three cases of ep-scattering described by equation (1.17) are given for $i = 1$ elastic scattering off a Dirac-like proton, $i = 2$ elastic scattering off a real proton and for $i = 3$ deeply inelastic scattering.*

where in equation (1.20) the longitudinal structure function $F_L(x, Q^2)$ was introduced. F_L is defined as the deviation of the Callan-Gross relation

$$F_L(x, Q^2) = F_2(x, Q^2) - 2xF_1(x, Q^2)\,. \tag{1.21}$$

In the naive quark parton model, where the proton is assumed to consist of three spin 1/2-partons only, the Callan-Gross relation reads

$$F_2(x, Q^2) = 2xF_1(x, Q^2) \quad \Rightarrow \quad F_L(x, Q^2) \equiv 0\,. \tag{1.22}$$

1.2.1 The Connection between *ep*- and γp Scattering

Writing down the total cross section for (real) photons scattering off protons, one is led to a structure that has a striking similarity compared to the electron proton cross section:

$$\sigma_{\text{tot}}(\gamma p \to X) = \frac{4\pi^2\alpha}{K}\epsilon_\mu^* \epsilon_\nu W^{\mu\nu}\,, \tag{1.23}$$

where $W^{\mu\nu}$ is the same hadronic tensor as in section 1.2, ϵ^μ is the polarisation vector of the incoming photon and $K = \nu = qp/m_p$ is related to the flux ($4m_pK$) of the photons, and equals the energy of the photon in the proton rest frame. In general, one has to keep in mind that the actual photons are not real, but have a finite virtuality. Therefore the concept of a photon flux has to be adapted to virtual photons. A usual convention is to choose K in a way, such that

$$W^2 = (p+q)^2 = m_p^2 + 2m_pK \tag{1.24}$$

holds also for virtual photons. For real photons W^2 is given by equation (1.24) while for virtual photons equation (1.24) has to be replaced by

$$W^2 = m_p^2 + 2pq + q^2\,. \tag{1.25}$$

Requiring $2m_pK \stackrel{!}{=} 2pq + q^2$ leads to

$$K = \frac{pq}{m_p} + \frac{q^2}{2m_p} = \nu + \frac{q^2}{2m_p} \tag{1.26}$$

In contrast to real photons a virtual photon may also have longitudinal polarisation, resulting in the fact that there is a cross section for transversely polarised photons σ_T and

one for longitudinally polarised photons σ_L, and the total cross section is given by their sum:

$$\sigma_{\mathrm{tot}}(\gamma p \to X) = \sigma_T + \sigma_L \,, \tag{1.27}$$

with

$$\sigma_\lambda = \epsilon_\lambda^{*\mu} \epsilon_\lambda^{*\nu} W_{\mu\nu} \quad \text{and} \tag{1.28}$$

$$\epsilon_\lambda = \begin{cases} \mp\sqrt{\frac{1}{2}}(0, 1, \pm i, 0) & \lambda = \pm 1 \\ \frac{1}{\sqrt{Q^2}}\left(\sqrt{\nu^2 + Q^2}, 0, 0, \nu\right) & \lambda = 0 \end{cases} . \tag{1.29}$$

Evaluating equations (1.28) by means of equations (1.29) and the decomposition (1.13) of the hadronic tensor, one obtains

$$\sigma_T(x, Q^2) = \frac{4\pi\alpha^2}{Q^2} 2x F_1(x, Q^2) \quad \text{and} \tag{1.30}$$

$$\sigma_L(x, Q^2) = \frac{4\pi\alpha^2}{Q^2} \left[\left(1 + \frac{4m_p^2 x^2}{Q^2}\right) F_2(x, Q^2) - 2x F_1(x, Q^2) \right] , \tag{1.31}$$

respectively, where the structure functions W_i were replaced by the corresponding F_i and were expressed in terms of x and Q^2 instead of ν and q^2. Remembering the construction of the longitudinal structure function $F_L = F_2 - 2xF_1$, one recognises that the longitudinal cross section is proportional[4] to F_L justifying a posteriori the naming of F_L as longitudinal structure function.

To express the relation between ep- and γp-scattering, it is common to express the ep cross section (1.19) differential in y and Q^2:

$$\frac{\mathrm{d}^2\sigma(ep \to X)}{\mathrm{d}y\,\mathrm{d}Q^2} = \underbrace{\frac{\alpha}{2\pi}\frac{1}{yQ^2}\left[(1 + (1-y)^2)\right]}_{f^T_{\gamma/e}} \sigma_T + \underbrace{2(1-y)}_{\propto f^L_{\gamma/e}} \sigma_L \Big] \tag{1.32}$$

$$= f^T_{\gamma/e}\sigma_T + f^L_{\gamma/e}\sigma_L \,, \tag{1.33}$$

defining the transverse and longitudinal flux factors $f^T_{\gamma/e}$ and $f^L_{\gamma/e}$, respectively, giving the probability to find a photon "inside" an electron with inelasticity y at a given virtuality Q^2. In practice, it was found that the electron mass is not to be neglected when the electron and hadron tensors are contracted. The transverse flux factor is modified with a term proportional to the electron mass squared and Q^2. The former dependence is expressed through $Q^2_{\mathrm{min}} = y^2 m_e^2/(1-y)$ which is the minimal virtuality kinematically allowed:

$$f^T_{\gamma/e} = \frac{\alpha}{2\pi}\frac{1}{yQ^2}\left(1 + (1-y)^2 - 2(1-y)\frac{Q^2_{\mathrm{min}}}{Q^2}\right) \tag{1.34}$$

$$f^L_{\gamma/e} = \frac{\alpha}{2\pi}\frac{1}{yQ^2} 2(1-y) \tag{1.35}$$

1.3 Kinematical Regimes

At HERA there are essentially two large kinematic regimes, connected by a transition region:

[4] except for $4m_p^2x^2/Q^2$, which is small as $x \ll 1$

1. Photoproduction, where the virtuality is small and

2. the regime of deeply inelastic scattering (DIS), where Q^2 is large and perturbative methods are applicable, since the virtuality sets the scale of the process, and for $Q^2 \gtrsim 1$ GeV^2 the coupling constant of the strong interaction becomes sufficiently small for a perturbative expansion to converge.

3. The transition region in between the above is of great theoretical interest, since there the interplay between soft and hard physics can be studied and therefore great efforts are undertaken experimentally to collect data from the transition region.

In the following a brief description of deep inelastic scattering and related physics is presented, followed by a review on photoproduction.

1.4 Deep Inelastic Scattering

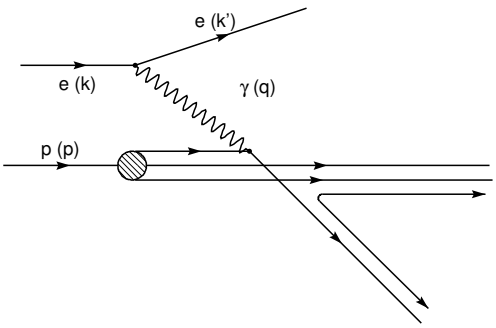

Figure 1.2: The deeply inelastic scattering of an electron off a proton: *The electron emits a photon that subsequently hits a parton that is kicked out of the proton. Hadronisation is indicated as the creation a of quark anti-quark pair.*

When the virtuality of the exchanged photon is large enough, the resolution becomes sufficient to directly probe the proton's charged constituents. In this case the momentum transferred to this parton is too large, such that it can no longer be bound inside the proton, but is "kicked" out. This is shown schematically in figure 1.2. Due to confinement the struck parton cannot exist freely as it carries colour charge and confinement requires strongly interacting particles to form colourless objects – hadrons. A process called hadronisation sets in, providing colour neutrality by the creation of quark anti-quark pairs in between the struck parton and the proton remnant until only colour neutral objects exist.

As both the electron and the charged partons carry electric and weak charges, at virtualities large enough weak exchange starts to contribute. Large virtualities means that the propagator $P^2 = q^4/(q^2 + M^2_{Z/W})^2$ for the weak exchange is no longer suppressed i.e. $\sqrt{Q^2} \sim M_{Z/W} \sim 80$ GeV. Depending on the charge of the exchanged boson one distinguishes between neutral and charged currents:

$$\begin{array}{ll} \text{neutral current:} & \text{charged current:} \\ ep \xrightarrow{\gamma, Z^0} e'X & ep \xrightarrow{W^{\pm}\,(-)} \nu_e\, X \end{array} \quad , \tag{1.36}$$

where depending on the charge of the electron and thus of the exchanged W the final state lepton is the neutrino or anti-neutrino. For these high virtualities the cross section (1.20) has to be modified to incorporate the weak exchange. This is done by introducing the structure function $F_3(x, Q^2)$ and to the cross section (1.20) a term $\pm(1-(1-y)^2)xF_3(x, Q^2)$ is added, where the sign depends on whether positrons (+) or electrons (−) scatter off the proton.

In leading order (LO) QCD the structure functions F_i read

$$F_2(x,Q^2) = x\sum_q \mathcal{A}_q\left[q(x,Q^2)+\bar{q}(x,Q^2)\right] \tag{1.37}$$

$$xF_3(x,Q^2) = x\sum_q \mathcal{B}_q\left[q(x,Q^2)-\bar{q}(x,Q^2)\right] \tag{1.38}$$

$$F_L(x,Q^2) = 0\,, \tag{1.39}$$

where the sum runs over all quark flavours kinematically accessible (u,d,s,c,b). The quark density functions $q(x,Q^2)\,\mathrm{d}x\mathrm{d}Q^2$ yield the probability to find a quark with momentum fraction $x' \in [x, x+\mathrm{d}x]$ given a resolution $Q'^2 \in [Q^2, Q^2+\mathrm{d}Q^2]$. Analogously, $\bar{q}(x,Q^2)\mathrm{d}x\mathrm{d}Q^2)$ denote the density functions for anti-quarks.

The weight factors $\mathcal{A}_q(Q^2)$ and $\mathcal{B}_q(Q^2)$ are the sum of the charges that the respective quarks carry and to which the exchange boson of either electromagnetism or weak exchange couple:

$$\mathcal{A}_q(Q^2) = e_q^2 - 2v_e e_q v_q P(Q^2) + (v_e^2+a_e^2)(v_q^2+a_q^2)P^2 \overset{Q^2\to 0}{\longrightarrow} e_q^2 \tag{1.40}$$

$$\mathcal{B}_q(Q^2) = -2a_e e_q a_q P(Q^2) + 4v_e a_e v_q a_q)P^2 \overset{Q^2\to 0}{\longrightarrow} 0\,, \tag{1.41}$$

with the electric charge e_q, and the charges of the vector and axial vector currents v_q and a_q of the weak interaction, respectively.

1.5 Photoproduction

Photoproduction events lie in that region of phase space where the virtuality is (vanishingly) small, such that the scattering may be interpreted as scattering of quasi real photons off protons. This occurs if the scattering angle vanishes.

In this limit the differential ep cross section is given by the total γp cross section times the flux of transversely polarised photons since $\sigma_T \overset{Q^2\to 0}{\longrightarrow} \sigma_{\mathrm{tot}}(\gamma p \to X)$ as $\sigma_L \overset{Q^2\to 0}{\longrightarrow} 0$

$$\frac{\mathrm{d}^2\sigma(ep\to X)}{\mathrm{d}y\,\mathrm{d}Q^2} = f^T_{\gamma/e}\sigma_{\mathrm{tot}}(\gamma p\to X)\,. \tag{1.42}$$

When dealing with photoproduction at HERA, one is more interested in the actual γp cross section though the measurement yields an ep cross section. By virtue of equation (1.42) one can convert a measured ep cross section into a γp cross section. This is done by integrating over Q^2 and y:

$$\sigma(ep\to X) = \int \mathrm{d}y \int \mathrm{d}Q^2\, f^T_{\gamma/e}\sigma(\gamma p\to X)_{\mathrm{tot}} = \mathcal{F}_{\gamma/e}\sigma_{\mathrm{tot}}(\gamma p\to X)\,. \tag{1.43}$$

To describe photoproduction the following model for the photon is used [5]: Quantum mechanics allows for fermionic fluctuations of the photon: $\gamma \leftrightarrow f\bar{f}$, where the fermions may be leptons ℓ or quarks q. The latter can interact strongly and therefore turn out to be responsible for the major part of the total γp cross section. The hadronic spectrum of fluctuations is split into a part of low virtuality and one of high virtuality[5]. The former part

[5] The term "virtuality" here refers to the amount of "off-shellness" that comes in addition to the virtuality q^2 of the photon.

can be approximated by the sum of the lowest-lying vector mesons, while the latter should be calculable perturbatively, if the scale k_0 separating the domains is chosen properly. The statement that the low-virtuality part can be parametrised by a sum of vector mesons is the essence of the vector meson dominance (VMD) model. This model was generalised to incorporate a smooth behaviour between the resonances by means of an integral over a spectral density: $\sum \to \int \mathrm{d}m\,\mathrm{d}m'\rho(m,m')$ (cf for example [6]). These kinds of models are called generalised VMD models (gVMD).

With the above classification the photon can be written as[6]

$$|\gamma\rangle = c_0|\gamma_0\rangle + \sum_{V=\rho^0,\omega,\phi,J/\psi} c_V|V\rangle + \sum_{q=u,d,s,c,b} c_q|q\bar{q}\rangle + \sum_{\ell=e,\mu,\tau} c_\ell|\ell^+\ell^-\rangle\,, \tag{1.44}$$

where the coefficients c_i in general depend on the scale $\mu = k_\perp$ with which the photon is probed:

$$c_i^2 = \begin{cases} \dfrac{4\pi\alpha}{f_V^2} & i = V \qquad k_\perp \le k_0 \\ \dfrac{\alpha}{2\pi} 2e_q \ln\left(\dfrac{k_\perp^2}{k_0^2}\right) & i = q \quad ; \quad k_\perp > k_0 \\ \dfrac{\alpha}{2\pi}\dfrac{2}{3}\ln\left(\dfrac{k_\perp^2}{m_\ell^2}\right) & i = \ell \\ 1 - \sum c_V^2 - \sum c_q^2 - \sum c_\ell^2 & i = 0 \end{cases} \tag{1.45}$$

The coefficient for the bare photon, labelled with $i = 0$ is given by unitarity.

The $|q\bar{q}\rangle$ part of equation (1.44) can be further subdivided into two parts depending on the relative transverse momentum $k_\perp$ of the $q\bar{q}$ splitting relative to the photon and the transverse momentum $p_\perp$ of the parton coming from the proton. For $p_\perp > k_\perp$ the events are characterised as anomalous, while for $p_\perp < k_\perp$ they are called direct. This division holds down to the above mentioned scale $k_\perp > k_0$ separating the high virtuality domain from the low virtuality domain. Figure 1.3 shows the definition of the scales k_0, $k_\perp$ and $p_\perp$ together with the separation of the phase space into the above domains.

1. The VMD processes, where the photon fluctuates into a vector meson before the interaction, and thus all processes allowed in hadronic physics shown in figure 1.5 may occur. This includes elastic and dissociative scattering as well as low $p_\perp$ and high $p_\perp$ non-diffractive events.

   By construction the VMD model allows to express this part of the cross section $\sigma^{\gamma p}_{\mathrm{VMD}}$ as a sum of total vector meson proton cross sections times their respective couplings:

   $$\sigma^{\gamma p}_{\mathrm{VMD}} = \sum_V \frac{4\pi\alpha}{f_V^2}\sigma^{Vp}_{\mathrm{tot}}\,, \tag{1.46}$$

   where for the total vector meson proton cross section a phenomenological parametrisation inspired by Regge theory can be used.

2. The direct processes, where the photon interacts directly with a parton from the proton.

   In leading order these processes consist of the QCD Compton effect $\gamma q \to qg$ and the boson-gluon fusion $\gamma g \to q\bar{q}$. As both processes diverge as $k_\perp \to 0$ the lower cut-off k_0 is introduced.

[6] The small contribution of the Υ is neglected.

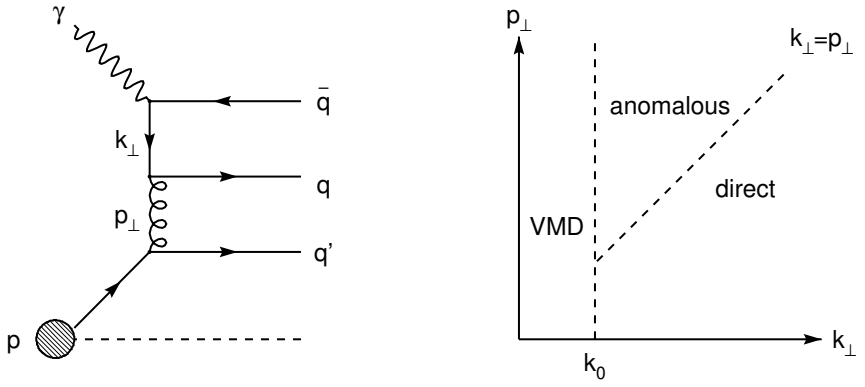

Figure 1.3: The scales $k_\perp$ and $p_\perp$ in photoproduction: *The left part shows an illustration of the scales $k_\perp$ and $p_\perp$ in a schematic graph of a hard γp interaction. The right part shows the classification of γp interactions in the $(k_\perp, p_\perp)$-phase space.*

3. The so called anomalous processes, where the photon splits into a high $k_\perp$ $q\bar{q}$ pair, and one of these subsequently interacts with a parton from the proton.

   This part can be expressed in terms of some sort of gVMD cross section:

$$\sigma^{\gamma p}_{\text{anomalous}} = \frac{\alpha}{2\pi} \sum_q 2e_q \int_{k_0^2}^{\infty} \frac{\mathrm{d}k_\perp^2}{k_\perp^2} \frac{k^2_{V(q\bar{q})}}{k_\perp^2} \sigma^{V(q\bar{q})p} \,, \tag{1.47}$$

   where $k_{V(q\bar{q})}$ is a model parameter that is associated with the typical $k_\perp$ inside the vector meson formed by the $q\bar{q}$ pair.

Based on this classification the total photon-proton cross section can be written as the sum of the respective cross sections:

$$\sigma^{\gamma p}_{\text{tot}} = \sigma^{\gamma p}_{\text{VMD}} + \sigma^{\gamma p}_{\text{direct}} + \sigma^{\gamma p}_{\text{anomalous}} \,. \tag{1.48}$$

1.6 Diffraction

"Diffractive scattering" is often used synonymously for "scattering with vacuum exchange", where vacuum exchange means that only momentum and angular momentum may be exchanged but no internal quantum numbers such as isospin, baryon number, etc. The term diffractive stems from the observation of a striking similarity of the angular spectrum $\mathrm{d}\sigma/\,\mathrm{d}|t|$ in hadron hadron interactions with the pattern of diffraction observed in optics as can be seen in figure 1.4. In wave optics the observed pattern can be related to properties like the shape or opacity of the target. The shape of the target can be described by a profile function, and the angular spectrum observed is related to this profile function by a Fourier transformation. And it is thus possible to deduce the shape of the target by the inverse transformation of the angular spectrum. This technique can also be used to deduce the profile function or shape of a hadron in a high energy collision.

Hadronic interactions are generically classified into diffractive and non-diffractive events, where for the diffractive class is further subdivided as shown in figure 1.5: If both incident particles stay intact one speaks of elastic scattering, while, if one is excited and dissociates one speaks of single dissociative diffraction. If both particles break up, double dissociative diffraction occurred. The rest, when internal quantum numbers are exchanged, is collectively called non-diffractive.

This classification suggests a further definition of diffraction often used to distinguish diffractive from non-diffractive interactions. It is the fact that in diffractive interactions the outgoing particles are strongly collimated along the direction of flight of the incoming particles. This means that there is hardly any activity in the central region, because no quantum numbers are exchanged especially no gluons carrying colour that through hadronisation fill the longitudinal phase space. This fact can be nicely expressed in a variable named rapidity defined as

$$Y = \frac{1}{2} \ln \left(\frac{E + p_z}{E - p_z} \right) \tag{1.49}$$

or the pseudo-rapidity

$$\eta = -\ln \tan \vartheta/2 \,, \tag{1.50}$$

which contains the polar angle of the scattering and is thus more intuitive. Rapidity and pseudo-rapidity are approximately equal and for massless particles they become identical. For massive particles Y and η may be used interchangeably only for rapidities not too large, or angles not too near to either $0°$ or $180°$, since for the latter, the logarithm goes to $\pm\infty$, while the fraction of the former is still finite.

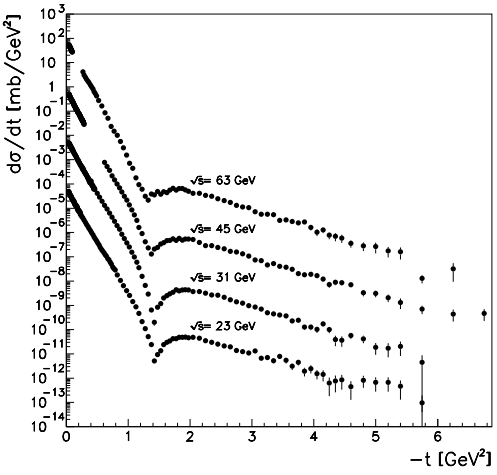

Figure 1.4: Angular spectrum in nucleon nucleon scattering: *$d\sigma/d|t|$ as seen in pp scattering at centre of mass energies of $\sqrt{s} = 23.5$, 30.7, 44.7 and 62.5 GeV measured at the ISR [7]. The respective cross sections were scaled by factors of 10^{-6},10^{-4} and 10^{-2} for better visibility.*

If an elastic interaction like in figure 1.5a) occurred with an angle of $\vartheta = 1$ mrad for example the respective pseudo-rapidities of the scattered particles are $\eta_{C/D} \approx \pm 7.6$, and there is a gap of 15 units in rapidity of no activity in between the scattered particles. This gave rise to the name of rapidity-gap events. This picture holds also if one or even both particles dissociate diffractively. The spike a single particle has in a rapidity distribution is smeared out, but the width of this effect is small compared to the width of the gap in between the two final states. This is shown schematically in figure 1.5 below the diagrams depicting the respective processes.

In general diffractive interactions are soft (small scattering angle) so that there is no hard scale available which can be used to perform any perturbative calculations with the result that (perturbative) QCD is not applicable and one therefore has to rely on phenomenological models such as Regge theory or others.

1.6.1 Regge Theory

Regge theory is founded on the basis of (1) unitarity, (2) crossing symmetry and (3) analyticity.

1. Unitarity is the assertion of conservation of probability, or in other words the probability that something happens is one, or more explicitely, if S is the operator that

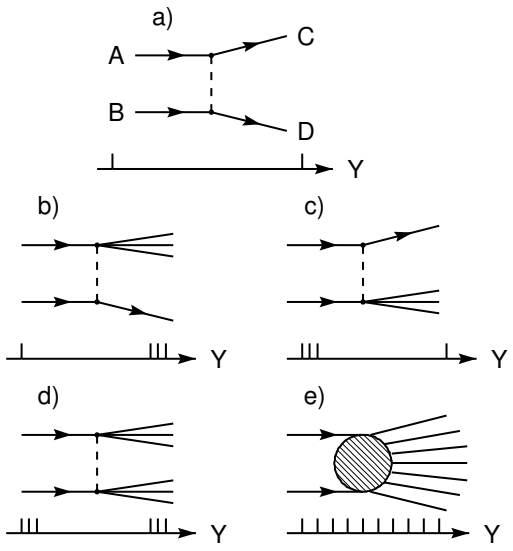

Figure 1.5: Event classes in hadronic interactions: *a) elastic, b)+c) single dissociative, d) double dissociative and e) non-diffractive or minimum bias events. Below the respective diagrams the rapidity population of the final state is indicated.*

transforms an initial state $|i\rangle$ into some final state $|f\rangle$ by $|f\rangle = S|i\rangle$, unitarity requires $S^\dagger S = \mathbb{1}$.

The optical theorem,

$$\sigma_{\rm tot} = \frac{1}{s}{\rm Im}[A(s,t=0)] \tag{1.51}$$

connecting the imaginary part of the forward scattering amplitude with the total cross section, is a consequence of unitarity, as well as the Froissart bound limiting the rise of the total cross section.

2. Crossing symmetry is a property in relativistic field theory but a postulate in S matrix theory. Using the Mandelstam variables s, t and u, defined for elastic scattering as

$$\begin{array}{rcl} s & = & (p_A + p_B)^2 = (p_C + p_D)^2 \\ t & = & (p_A - p_C)^2 = (p_B - p_D)^2 \\ u & = & (p_A - p_D)^2 = (p_B - p_C)^2 \end{array} \qquad \begin{array}{ll} A & \quad C \\ & \bullet \\ B & \quad D \end{array} \tag{1.52}$$

crossing allows for the identification of the process $AB \to CD$ with the process $A\bar{C} \to D\bar{B}$ or $A\bar{D} \to D\bar{C}$, where the barred particles are the respective antiparticles with opposite momentum. Calculating the new variables labelled with a prime for

the former and two primes for the latter processes,

$$\begin{array}{rcl} s' & = & (p_A + p_{\bar{C}})^2 \\ t' & = & (p_A - p_{\bar{B}})^2 \\ u' & = & (p_A - p_D)^2 \end{array} \quad \begin{array}{c} A \\ \\ \bar{C} \end{array} \diagdown\!\!\diagup \begin{array}{c} \bar{B} \\ \\ D \end{array} \quad \Rightarrow \quad \begin{array}{rcl} s & \to & t' \\ t & \to & s' \\ u & \to & u' \end{array} \tag{1.53}$$

$$\begin{array}{rcl} s'' & = & (p_A + p_{\bar{D}})^2 \\ t'' & = & (p_A - p_C)^2 \\ u'' & = & (p_A - p_{\bar{B}})^2 \end{array} \quad \begin{array}{c} A \\ \\ \bar{D} \end{array} \diagdown\!\!\diagup \begin{array}{c} C \\ \\ \bar{B} \end{array} \quad \Rightarrow \quad \begin{array}{rcl} s & \to & u'' \\ t & \to & t'' \\ u & \to & s'' \end{array} \tag{1.54}$$

one can readily make the identifications for the so called t-channel reaction in equation (1.53) and the u-channel in equation (1.54).

3. Analyticity claims that the amplitude describing a specific process is an analytic function. Knowing the analytic properties of the amplitude allows for the calculation of the amplitude of the crossed reaction by continuing the amplitude appropriately.

Regge theory starts with the scattering amplitude $A(s,t)$ as a partial wave expansion:

$$A(s,t) = \sum_{\ell}^{\infty} (2\ell + 1) a_\ell(s,t) P_\ell(z)\,, \tag{1.55}$$

where $z = \cos\vartheta$ is used for brevity, the partial waves amplitudes are denoted by a_ℓ and P_ℓ are the Legendre polynomials. Regge was interested in the behaviour of the scattering amplitude for the process $A\bar{C} \to \bar{B}D$ in the unphysical limit of $z \to -\infty$ that corresponds via crossing – as Mandelstam realized – to the s-channel reaction $AB \to CD$ for $s \to \infty$, so to say justifying a posteriori the dubious considerations $z = \cos\vartheta \to -\infty$. The expansion

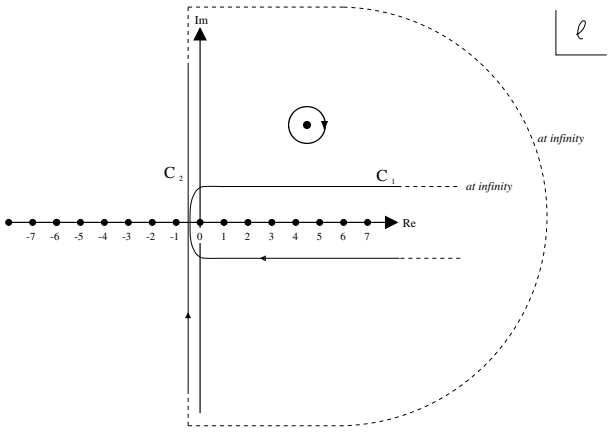

Figure 1.6: *The complex ℓ plane and the integration contours C_1 and C_2.*

(1.55) diverges for $|z| > 1$, so the trick was to drop the requirement for ℓ to be an integer,

but to allow for complex values. The generalisation of equation (1.55) for complex ℓ reads

$$A(s,t) = -\frac{1}{2}\int_{C_1} \mathrm{d}\ell\,(2\ell+1)a(\ell,t)\frac{P_\ell(z)}{\sin\pi\ell}\,, \tag{1.56}$$

where the path of integration encloses the positive real ℓ-axis[7] as shown in figure 1.6.

If the integration contour C_1 is enlarged such that $\mathrm{Im}\ell \to \infty$ the contour C_2 is obtained, so called Regge poles may appear. Assuming for simplicity a single pole only at $\ell = \alpha(t)$ with the approximate behaviour of $a(\ell,t) = \beta(t)/(\ell - \alpha(t))$, equation (1.56) becomes

$$A(s,t) = \pi(2\alpha(t)+1)\beta(t)\frac{P_{\alpha(t)}(z)}{\sin\pi\alpha(t)} - \frac{1}{2}\int_{C_2} \mathrm{d}\ell\,(2\ell+1)a(\ell,t)\frac{P_\ell(z)}{\sin\pi\ell}\,, \tag{1.57}$$

where the first term not yet present in equation (1.56) corresponds to the Regge pole with residue $\beta(t)$ which is unknown a priori. The second term is called background term and behaves like $s^{-1/2}$ in the s-channel reaction and thus vanishes for $s \to \infty$.

By virtue of crossing these poles in the t-channel correspond to physical resonances in the s-channel: The partial wave amplitude $a^{I\!R}(\ell,t)$ of the Regge pole can be written approximately as a Breit-Wigner resonance function

$$\begin{aligned} a^{I\!R}(\ell,t) &\approx \frac{\beta(t_r)/\alpha'_R(t_r)}{t_r - t - i\alpha_I(t_r)/\alpha'_R(t_r)} \\ &= \frac{\kappa\Gamma_r}{m_r^2 - t - i\Gamma_r}\,, \end{aligned} \tag{1.58}$$

if $\alpha(t)$ is decomposed into its real and imaginary parts $\alpha(t) = \alpha_R(t) + i\alpha_I(t)$ and then expanded in a Taylor-series about the point t_r where $\alpha_R(t)|_{t_r} = \ell$: $\alpha_R(t) = \ell + \alpha'_R(t)(t-t_r) + \cdots$ and $\alpha_I(t) = \alpha_I(t) + \alpha'_I(t)(t-t_r) + \cdots$. The resonance mass is to be identified with $m_r = \sqrt{t_r}$ and the width with $\Gamma_r = \alpha_I(t_r)/(m_r\alpha'_R(t_r))$.

And indeed, if one plots the spin of the various mesons versus their masses squared (called Chew-Frautschi-plot), one observes as in figure 1.7 that they string on straight lines

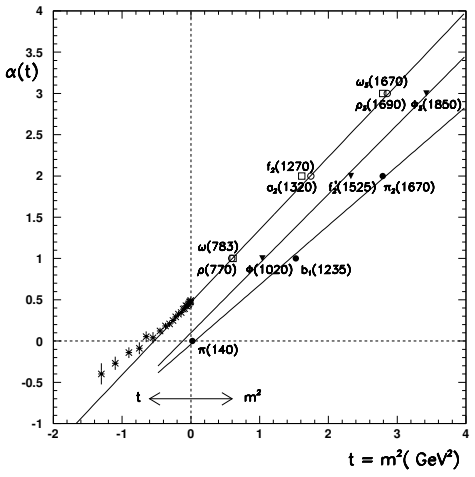

Figure 1.7: A Chew-Frautschi plot of the ρ, ω, ϕ and π trajectories. *The spins of mesons are plotted versus their masses squared. Also shown is the continuation of the ρ trajectory into the t-channel region as measured in $\pi^- p \to \eta n$ [8]*

$$\alpha(t) = \alpha_0 + \alpha' t \tag{1.59}$$

for t in the resonance region ($t > 0$). These lines are called Regge trajectories or Reggeons.

For asymptotic energies the scattering amplitude takes the form

$$A(s,t) \overset{s\to\infty}{\longrightarrow} \beta(t)\left(\frac{s}{s_0}\right)^{\alpha(t)}\,, \tag{1.60}$$

where for the Legendre polynomials the asymptotic form $P_{\alpha(t)} \to e^{-i\pi\alpha(t)}$ was used. So far, only the case of a single pole or resonance was assumed, but in the physical region $t > 0$ there are more resonances which have in principle to be taken into account, thus for the above limit the scattering amplitude is given by the sum of all resonances with $m^2 < s$.

[7] The original expansion can be recovered using Cauchy's theorem.

The total cross section for particles A and B, using the optical theorem (1.51), thus reads

$$\sigma_{\text{tot}}^{AB} = \sum_k \beta_{Ak}(0)\beta_{Bk}(0) \left(\frac{s}{s_0}\right)^{\alpha_k(0)-1} , \tag{1.61}$$

and the differential cross section

$$\frac{\mathrm{d}\sigma_{\text{el}}^{AB}}{\mathrm{d}t} = \frac{|A(s,t)|^2}{16\pi^2 s^2} = \sum_k \frac{\beta_{Ak}^2(t)\beta_{Bk}^2(t)}{16\pi} \left(\frac{s}{s_0}\right)^{2(\alpha_k(t)-1)} \tag{1.62}$$

$$\approx F(t) \left(\frac{s}{s_0}\right)^{2(\alpha(t)-1)} . \tag{1.63}$$

In the last step the dominance of the highest lying trajectory was assumed, so that the sum reduces to a single term. Then the function $F(t)$ absorbs all the t-dependence; in the Regge-limit where $|t| \ll s$ a behaviour of $F(t) \sim e^{b_0 t}$ can be assumed. Inserting this, yields

$$\frac{\mathrm{d}\sigma_{\text{el}}^{AB}}{\mathrm{d}t} = \mathcal{C} \exp\left[2\alpha_0 - 2 + 2\alpha' t \ln(s/s_0) + b_0 t\right] = \left.\frac{\mathrm{d}\sigma}{\mathrm{d}t}\right|_{t=0} e^{bt} , \tag{1.64}$$

with

$$b = b_0 + 2\alpha' \ln(s/s_0) . \tag{1.65}$$

From this equation follows that the slope b rises gently with energy and the interactions become more and more concentrated in the forward direction. This is the so called shrinkage of the diffractive peak, that is known for long.

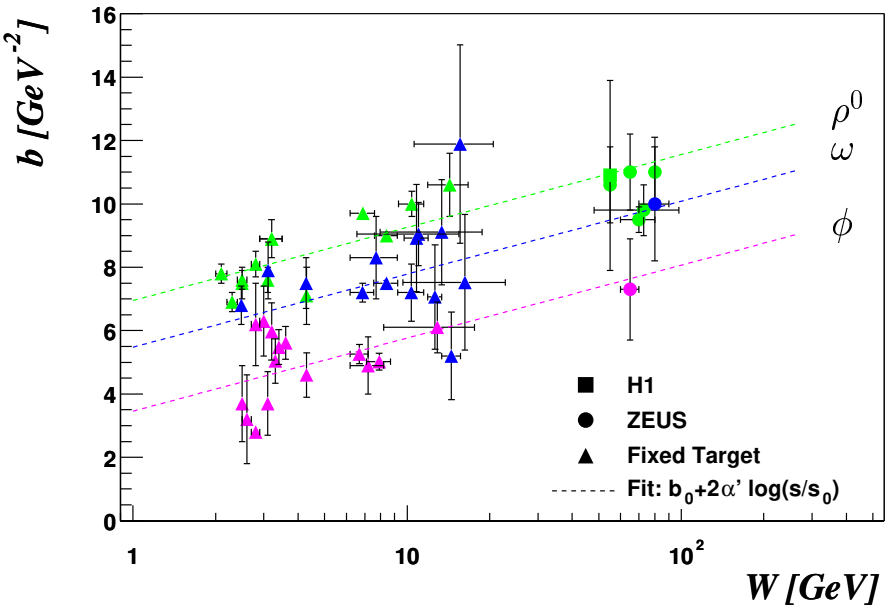

Figure 1.8: Slopes for the three light vector mesons: *The slopes of the light vector meson ρ^0, ω and ϕ measured in fixed target experiments and HERA are fitted with equation (1.65) for $s_0 = 10$ GeV^2.*

Figure 1.8 shows measurements [9, 10, 11, 12, 13, 14, 15, 16, 17, 18, 19, 20, 21, 22, 23, 24, 25, 26] of values for the slopes for the three light vector meson ρ^0, ω and ϕ together with a fit of equation (1.65) to these data to determine b_0 for fixed $s_0 = 10$ GeV^2. The results are listed in the last row of table 1.3

1.6.2 The Pomeron

The cross section predicted by equation (1.61) falls with energy roughly as $s^{-0.5}$ inserting the intercept of the highest lying trajectory with $\alpha_0 \approx 0.5$. But empirical fact (see figure 1.9) is that all hadronic cross sections rise slowly for energies $\sqrt{s} \gtrsim 10$ GeV. In order to accommodate for the rise of the high energy data a further trajectory was introduced with an intercept greater than unity. This trajectory

$$\alpha_{I\!P}(t) = 1 + \epsilon + 0.25t \quad \text{with} \quad \epsilon \ll 1 \tag{1.66}$$

was named after Pomeranchuk by Gribov who introduced it and is now known as Pomeron. But the Pomeron has the drawback that it ultimately violates unitarity at energies around 10^{23} GeV.

As there are no particles on the Pomeron trajectory, a simple identification with bound states as for the other trajectories is not possible. Though glue balls — hypothetical particles made up of bound gluons — are widely expected to lie on the Pomeron trajectory, since in a QCD picture Pomeron exchange can be modelled as the exchange of two gluons (or a gluon ladder, two gluons in between which further gluons are inter-exchanged) [27, 28, 29]. Another approach is to treat the Pomeron as a real particle. This approach is discussed briefly in the following:

The Pomeron in DIS

The Pomeron does not only appear in soft interactions, but also at high virtualities. What was observed were events at high Q^2 with a large rapidity gap, which could not be explained by means of ordinary DIS, since there, the longitudinal phase space is filled with hadronic activity due to hadronisation between the struck quark and the proton remnant. So these events were explained by a hard scattering of the photon and the Pomeron. One went one step further and made measurements of the structure function of the Pomeron in complete analogy to the measurements in ordinary DIS. To describe these kind of interactions two further variables have to be introduced: The momentum fraction $x_{I\!P}$ of the proton carried by the Pomeron and the momentum fraction β of the quark inside the Pomeron that is actually probed by the photon.

$$x_{I\!P} = \frac{(p - p')q}{pq} \approx \frac{M_X + Q^2}{W^2 + Q^2} \quad ; \quad \beta = \frac{x}{x_{I\!P}} \approx \frac{Q^2}{M_X^2 + Q^2} \tag{1.67}$$

In contrast to the ordinary F_2, the diffractive structure function depends on four variables: $F_2^D = F_2^D(\beta, Q^2, x_{I\!P}, t)$. As the scattered proton is in general not measured, t cannot be measured and this dependence is integrated over, and the measured quantity is the threefold differential cross section

$$\frac{\mathrm{d}^3\sigma}{\mathrm{d}\beta\,\mathrm{d}Q^2\,\mathrm{d}x_{I\!P}} = \frac{2\pi\alpha}{\beta Q^2}\left[1 + (1-y)^2\right] F_2^{D(3)}(\beta, Q^2, x_{I\!P}) \tag{1.68}$$

A measurement of $x_{I\!P} F_2^{D(3)}$ is published in [30], where for the intercept of the Pomeron a value of $\epsilon = 0.24 \pm 0.023$ was found, which is not small compared to unity. This gives rise to much stronger energy dependence than the originally introduced Pomeron and is therefore called hard Pomeron.

1.6.3 The Odderon

The Odderon is a trajectory that was introduced in analogy to the Pomeron, and the name is the abbreviation of Odd-under-crossing-Pomeron. The idea was [31], that, if the amplitude for pp scattering can be decomposed in a part even and a part odd under crossing as

$$A_{pp} = A_+ + A_- \,, \tag{1.69}$$

the amplitude for the crossed reaction $\bar{p}p$ is

$$A_{\bar{p}p} = A_+ - A_- \,, \tag{1.70}$$

leading to a finite difference in the cross sections $\Delta\sigma = \sigma^{pp} - \sigma^{\bar{p}p} \not\to 0$ for $s \to \infty$. For asymptotic energies the even amplitude A_+ is dominated by the Pomeron, and if there were a finite difference the odd amplitude would be dominated by what is called the Odderon, such that

$$A_+ \overset{s\to\infty}{\longrightarrow} A_{I\!P} \quad \text{the Pomeron} \tag{1.71}$$

$$A_- \overset{s\to\infty}{\longrightarrow} A_{I\!O} \quad \text{the Odderon} \tag{1.72}$$

If there is an Odderon, it manifests itself as mentioned above in a finite difference $\Delta\sigma$ of the total cross sections for pp and $\bar{p}p$ scattering, or in a related variable $\Delta\rho = \rho_{\bar{p}p} - \rho_{pp}$, where $\rho_{AB} = \mathrm{Re}A^{AB}/\mathrm{Im}A^{AB}$ for elastic scattering at $t = 0$, which vanishes only if there is no odd-under-crossing part in the amplitude. But as can be seen from the data [32] in figure 1.9 neither $\Delta\sigma$ nor $\Delta\rho$ seem to be finite.

From the construction of the Odderon – as odd under crossing amplitude – follows that its C- and P-parity are $C = P = -1$, in contrast to the Pomeron that exchanges only vacuum quantum numbers $C = P = +1$. Nothing is known about the trajectory of the Odderon except for the intercept, that again by construction is near unity (otherwise it could not contribute at high energies). The slope is commonly assumed to be similar to the Pomeron slope.

$$\alpha_{I\!O}(t) \approx 1 + 0.25t \tag{1.73}$$

The simple analogue to the two gluon model of the Pomeron is a three gluon model for the Odderon [33].

1.6.4 Cross Sections

In [34] fits to total cross sections and ρ-parameters for AB and $\bar{A}B$ reactions were done, assuming that in the sum in equation (1.61) only the Pomeron and two effective Regge trajectories contribute:

$$\sigma_{\mathrm{tot}}^{\overset{(-)}{A}B} = X^{AB}s^{\epsilon} + Y_+^{AB}s^{-\eta_+} \mp Y_-^{AB}s^{-\eta_-} \,, \tag{1.74}$$

where the barred quantities refer to the respective anti-particle[8]. The first term $X^{AB}s^{\epsilon}$ corresponds to the Pomeron, while the $Y_\pm^{AB}s^{-\eta_\pm}$ terms correspond to C-even trajectories $(+)$ and C-odd trajectories $(-)$, respectively. The even trajectory is assumed to be a superposition of the a- and the f- trajectories, and for the odd one a superposition of the ρ- and ω-trajectories. The result of the fit is summarised in table 1.2 and shown in figure 1.9. In appendix A two further parametrisations of the cross sections are given and applied to vector meson photoproduction.

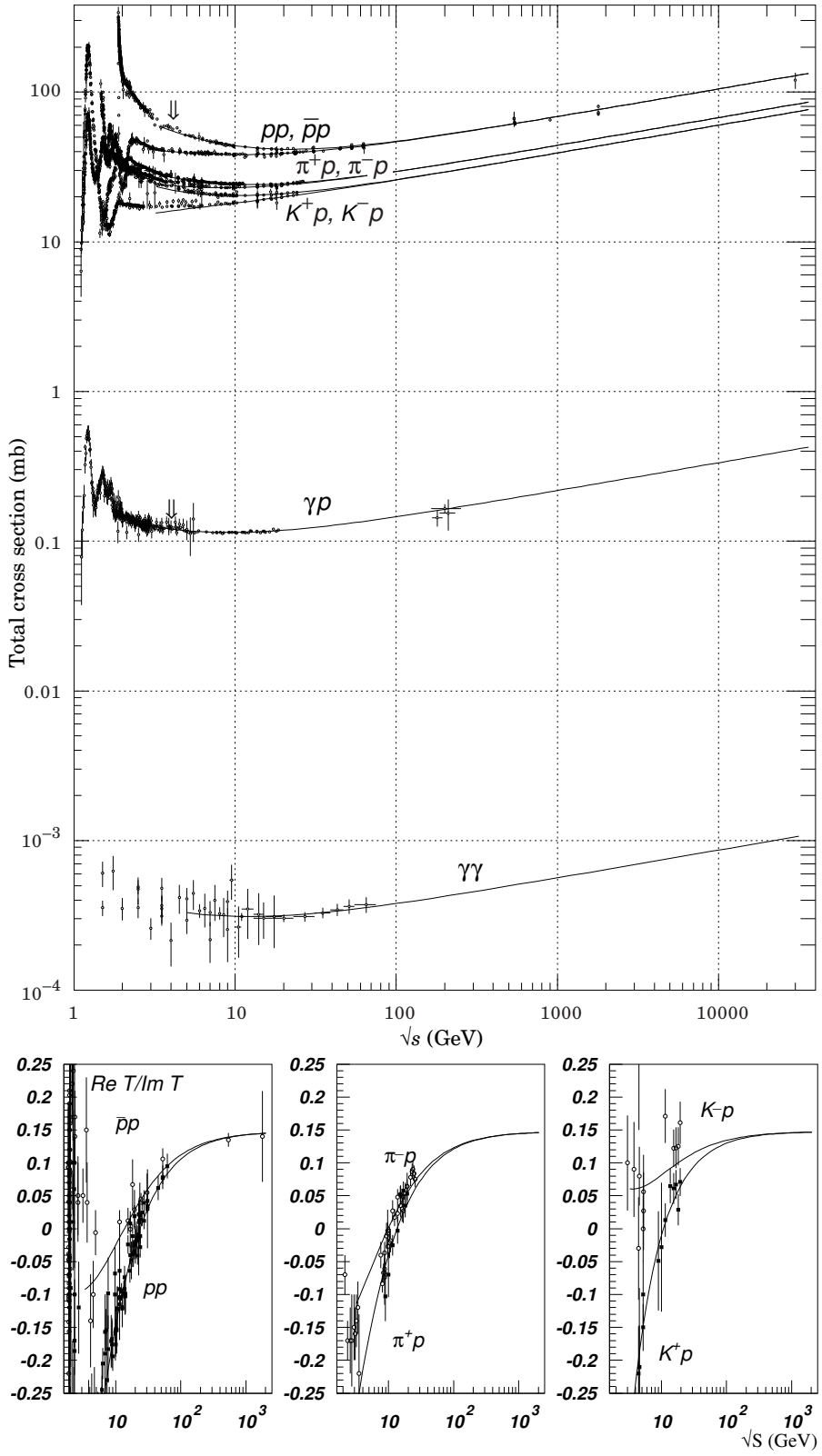

Figure 1.9: Fit to total cross sections and ρ-parameters: *The upper part shows a fit performed in [34] to total cross sections for $p^{\pm}p$, $\pi^{\pm}p$, γp and $\gamma\gamma$ reactions. The lower part shows the fit to the ρ-parameter for $p^{\pm}p$, $\pi^{\pm}p$ and $K^{\pm}p$ reactions.*

	ϵ	η_+	η_-
	0.0933±0.024	0.357±0.015	0.560±0.015

process	X [mb]	Y_+ [mb]	Y_- [mb]
pp	18.79±0.51	63.0±2.3	36.2±3.2
πp	12.08±0.29	26.2±0.74	7.63±0.72
Kp	10.76±0.23	14.08±0.57	14.7±1.3
$\gamma p \times 10^2$	5.98±0.17	11.64±0.88	—
$\gamma\gamma \times 10^4$	1.55±0.14	3.9±2.0	—

Table 1.2: Fit to total cross sections and ρ-parameters: *Results for the reactions $p^{\pm}p$, $\pi^{\pm}p$, $\pi^{\pm}p$, γp and $\gamma\gamma$ reactions and for the ρ-parameter in $p^{\pm}p$, $\pi^{\pm}p$ and $K^{\pm}p$ reactions[34]. The χ^2 per degree of freedom was found to be 1.02 with $N = 382$.*

Using the above described methods, one can derive cross sections for elastic vector meson photoproduction [36]: Insertion of $|A|^2 = (1+\rho^2)\mathrm{Im}A^2$, where $\rho = \mathrm{Re}A/\mathrm{Im}A$ into the differential cross section $\mathrm{d}\sigma/\mathrm{d}t = |A|^2/(16\pi s^2)$, together with the optical theorem i.e. for $t = 0$, yields

$$\left.\frac{\mathrm{d}\sigma_{\mathrm{el}}(\gamma p \to Vp)}{\mathrm{d}t}\right|_{t=0} = \frac{1+\rho^2(s,0)}{16\pi}\left[\sigma_{\mathrm{tot}}(\gamma p \to Vp)\right]^2 . \tag{1.75}$$

Under the assumption that at energies high enough the real-part of the scattering amplitude can be neglected due to Pomeron dominance i.e. $\rho \to 0$, the elastic cross section is obtained by integration over t:

$$\sigma_{\mathrm{el}}(\gamma p \to Vp) = \frac{1}{16\pi b}\left[\sigma_{\mathrm{tot}}(\gamma p \to Vp)\right]^2 , \tag{1.76}$$

where a t dependence according to equation (1.64) for the whole range with the slope b given by equation (1.65) is assumed. The total $\gamma p \to Vp$-cross section can be obtained from vector meson dominance using equation (1.46), where $\sigma_{\mathrm{VMD}}(\gamma p)$ is just the sum over the respective $\gamma p \to Vp$-cross sections, which themselves are given by the total Vp-cross sections. Therefore one can write

$$\sigma_{\mathrm{tot}}(\gamma p \to Vp) = \frac{4\pi\alpha}{f_V^2}\sigma_{\mathrm{tot}}^{Vp} . \tag{1.77}$$

The Vp-cross section can be approximated, using the additive quark model [36], by

$$\sigma_{\mathrm{tot}}^{\rho^0 p} \approx \sigma_{\mathrm{tot}}^{\omega p} \approx \frac{1}{2}\left(\sigma_{\mathrm{tot}}^{\pi^+ p} + \sigma_{\mathrm{tot}}^{\pi^- p}\right) \text{ and} \tag{1.78}$$

$$\sigma_{\mathrm{tot}}^{\phi p} \approx \sigma_{\mathrm{tot}}^{K^+ p} + \sigma_{\mathrm{tot}}^{K^- p} - \sigma_{\mathrm{tot}}^{\pi^- p} . \tag{1.79}$$

Thus, finally inserting equations (1.78) and (1.77) into (1.76) yields the approximate cross

[8] This fit is an extension of a fit performed by Donnachie and Landshoff [35] where only one effective Regge trajectory was taken into account.

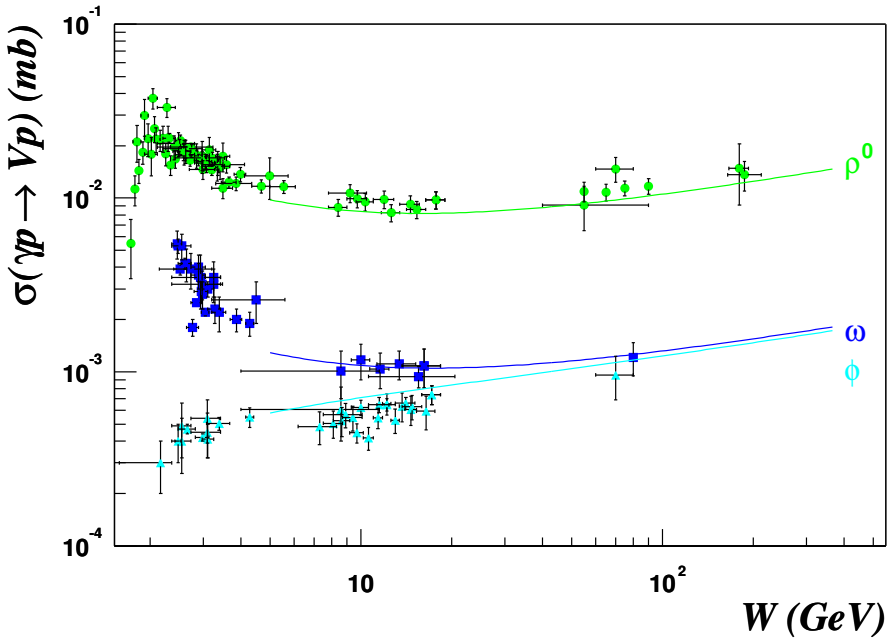

Figure 1.10: Comparison of the Regge model with data: *Prediction of equation (1.80) as compared with with data for the light vector mesons ρ^0, ω and ϕ.*

section for elastic vector meson photoproduction[9]:

$$\sigma_{\mathrm{el}}(\gamma p \to Vp) \;=\; \frac{4\pi\alpha}{f_V^2}\frac{1}{16\pi b}\left[X^{Vp}s^{\epsilon} + Y_+^{Vp}s^{\eta_+} - Y_-^{Vp}s^{Vp}s^{\eta_-}\right]^2, \tag{1.80}$$

where the values for the respective parameters X^{Vp}, Y_+^{Vp} and Y_-^{Vp} are summarised in table 1.3 together with the coupling constants – or transition probabilities $f_V^2/4\pi\alpha$, taken from [37] and are shown in the last column of table 1.3.

The result of equation (1.80) using equation (1.65) together with the values of table 1.3 is shown in figure 1.10 for the light vector mesons ρ^0, ω and ϕ.

[9] only a single power of $4\pi\alpha/f_V^2$ is used – not squared – because this would yield the truly elastic case $(\gamma \to V) + p \to (V \to \gamma) + p$.

	ρ^0	ω	ϕ
X^{Vp} [mb]	12.08±0.29	12.08±0.29	9.44 ±0.54
Y_+^{Vp} [mb]	26.2 ±0.74	26.2 ±0.74	1.96 ±1.36
Y_-^{Vp} [mb]	0	0	−7.63±0.72
$f_V^2/4\pi\alpha$	2.69 ±0.27	24.6 ± 3.8	18.8 ± 1.5
b_0 [GeV^{-2}]	8.1 ± 0.1	6.6 ± 0.2	4.6 ± 0.2

Table 1.3: Parameters for the Regge-VMD cross sections: *Predictions of equation (1.78) using the values of table 1.2 to be used with equation (1.80). The coupling constants $f_V^2/4\pi\alpha$ for the transition $\gamma \leftrightarrow V$ for the light vector mesons $V = \rho^0$, ω and ϕ as measured in photoproduction (taken from [37]). The slopes b_0 fitted for $s_0 = 10$ GeV^2 by equation (1.65) are given in the last row.*

1.7 Other Models

In the following two other models that are to describe (inclusive) photoproduction and exclusive meson-production are discussed. These are the class of the dipole models and an eikonal model.

1.7.1 Dipole Models

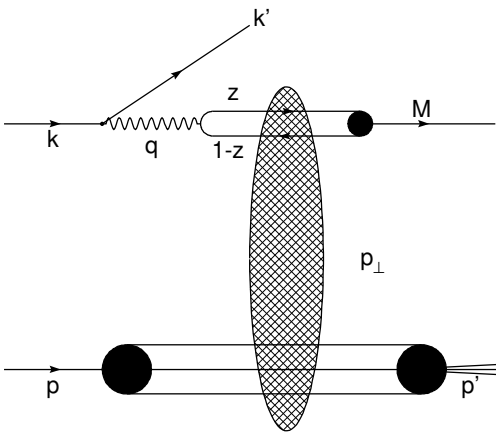

Figure 1.11: *A schematic diagram of the γp interactions in the color dipole model.*

Photon-proton interactions can be described by dipole models due to the fact, that in the proton rest frame the $q\bar{q}$ splitting can be considered as occurring sufficiently long before the actual interaction, so that the cross section can be factorized into a part dealing with the photon-$q\bar{q}$ fluctuation and another part modelling the interaction. These $q\bar{q}$ states are called color dipoles. Figure 1.11 shows the diagram representing photon-proton interactions in the color dipole model. The dashed region in between the proton and the color dipole indicates the interaction to be described by a model cross section $\hat{\sigma}$. The photon wave function ψ_γ is expressed in terms of the light cone variables z and $\boldsymbol{r}$, denoting, respectively, the momentum fraction of the photon carried by the quark and the transverse separation of the $q\bar{q}$ pair [38]:

$$\begin{aligned} |\gamma\rangle_{\text{had}} &= |q\bar{q}\rangle + |q\bar{q}+g\rangle + \cdots \\ &= \int \mathrm{d}z\mathrm{d}^2\boldsymbol{r}\ \psi_\gamma(z,r)|z,\boldsymbol{r}\rangle + \text{higher Fock states} \end{aligned} \tag{1.81}$$

The wave function is constructed in a way that the values of z and $\boldsymbol{r}$ do not change during the diffractive scattering, i.e. they are eigenstates of the scattering. The total γp cross

section can be written as

$$\sigma_{\mathrm{tot}}(\gamma p \to X) = \int \mathrm{d}z\mathrm{d}^2\boldsymbol{r}\ \left[|\psi_{\gamma,L}(z,r)|^2 + |\psi_{\gamma,T}(z,r)|^2\right] \hat{\sigma}(s,r,z)\,, \tag{1.82}$$

where $\hat{\sigma}(s,r,z)$ is the above mentioned model cross section for the scattering of a dipole with configuration $(z,\boldsymbol{r})$ off a proton. The photon wave functions can be calculated in QED, but the dipole cross section is subject to QCD with α_s large, and thus cannot be treated perturbatively.

These models can also be employed to describe exclusive vector meson production. Knowing the wave function of the meson, the cross section can be written as

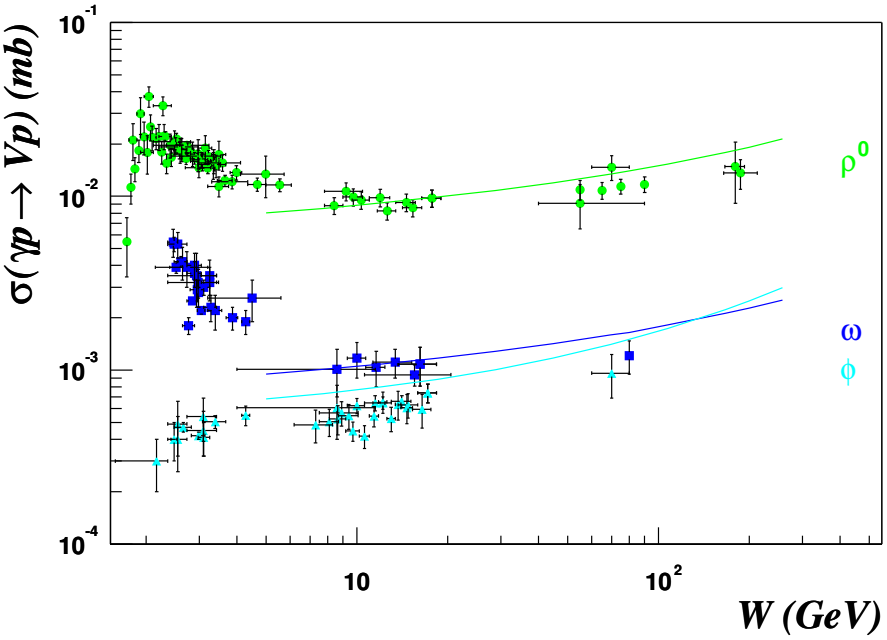

Figure 1.12: Comparison of the colour dipole model with data: *The result of equation (1.84) is compared with data for the light vector mesons ρ^0, ω and ϕ.*

$$\left.\frac{\mathrm{d}\sigma(\gamma p \to Vp)}{\mathrm{d}t}\right|_{t=0} = \frac{1}{16\pi}\sum_{\lambda=T,L}\left[\int \mathrm{d}z\mathrm{d}^2\boldsymbol{r}\ \psi_V^\dagger(z,r)\psi_{\gamma,\lambda}(z,r)\hat{\sigma}(s,r,z)\right]^2 \tag{1.83}$$

$$\sigma(\gamma p \to Vp) = \frac{1}{16\pi b}\sum_{\lambda=T,L}\left[\int \mathrm{d}z\mathrm{d}^2\boldsymbol{r}\ \psi_V^\dagger(z,r)\psi_{\gamma,\lambda}(z,r)\hat{\sigma}(s,r,z)\right]^2, \tag{1.84}$$

where in the last step the differential cross section was integrated using again a simple exponential as for equation (1.76), yielding an additional factor of $1/b$ for the total elastic cross section.

The details of the calculation of vector meson cross sections utilising the dipole model presented in [38] are given in appendix B. In Figure 1.12 the comparison of the model with data is shown. The rise of the vector meson cross sections at small energies is not reproduced, since any "Reggeon" contribution was neglected.

1.7.2 The Stochastic Vacuum Model (SVM)

The SVM [39] also provides a means to calculate cross sections for exclusive meson production in γp interactions. But in contrast to the above mentioned models, the SVM provides a QCD inspired formulation for the dipole cross section $\hat{\sigma}$: The amplitude A leading to the dipole cross section is written as a convolution of the proton wave functions in the initial and final states with the kernel of the interaction:

$$\hat{\sigma}_\lambda(z,r,t) = \left| \int \mathrm{d}^2\boldsymbol{r}'\, \chi^\dagger_\lambda(r')\chi(r')J_{MB}(t,\boldsymbol{r},\boldsymbol{r}') \right|^2 , \tag{1.85}$$

where χ is the wave function of the initial state proton and χ_λ is the wave function of the nucleonic final state with helicity λ, which are described by a single position space vector $\boldsymbol{r}$ only. J_{MB} is the meson-baryon profile function and is the quantity that is actually modelled within the SVM.

The calculations are performed in impact parameter space, such that the amplitude $A(\boldsymbol{r},\boldsymbol{b})$ has to be Fourier-transformed from $\boldsymbol{b}$ space to $\boldsymbol{p}_\perp$ space, with $t = -\boldsymbol{p}_\perp^2$, where $\boldsymbol{p}_\perp$ is the transverse momentum transferred in the scattering:

$$A(s,t) = 2is \int \mathrm{d}^2\boldsymbol{b}\, e^{i\boldsymbol{p}_\perp \boldsymbol{b}} \tilde{J}_{MB}(\boldsymbol{b}) , \tag{1.86}$$

where $\tilde{J}_{MB}(\boldsymbol{b})$ is the profile function one obtains after the convolutions over both $\boldsymbol{r}$ and $\boldsymbol{r}'$. But from equation (1.86) follows, that the cross sections bear no energy dependence and any dependence on the energy has to be added to the model ad hoc, since the optical theorem yields a factor $1/s$ that cancels the factor s in (1.86).

The hadrons are constructed from quarks and/or antiquarks moving on light-like paths, that are connected at arbritrary endpoints $t = \pm T$ with so called Schwinger strings to form gauge invariant Wegner Wilson loops. Figure 1.13 shows the space-time picture of the scattering and the construction of the hadrons. The configuration of the three quarks

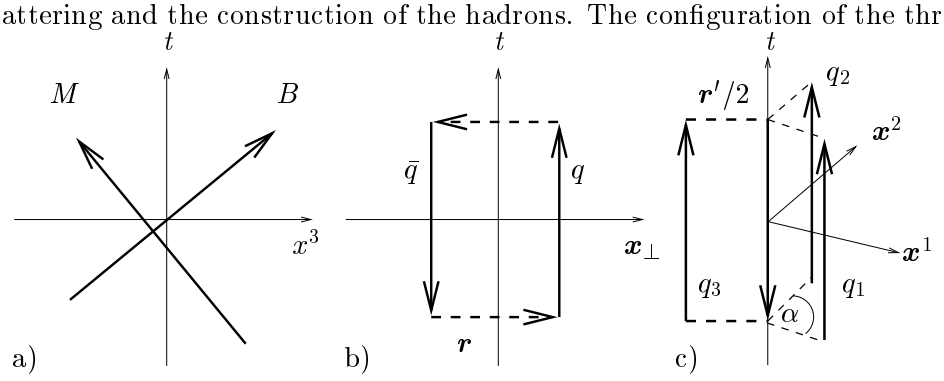

Figure 1.13: Schematic view of interactions in the SVM: *a) Space-time picture of the actual scattering in the SVM. b) Construction of a meson from a $q\bar{q}$ pair moving on the light cone with transverse separation $\boldsymbol{r}$. c) Analogous construction of a baryon of extension $\boldsymbol{r}'$ from three light-like quarks q_i.*

forming the baryon can be characterised by a single angle α, drawn in between the planes of q_1 and q_2. A baryon can be turned into a dipole analogue of a meson if α is set to zero. Then the baryon is said to consist of a quark and a point-like diquark.

The profile function J_{MB} can be written generically as:

$$J_{MB}(\boldsymbol{b}, \boldsymbol{r}, \boldsymbol{r}') = -\langle M \times B \rangle \,, \tag{1.87}$$

where the brackets denote functional integration over the gluon-background field and M and B represent the Wegner-Wilson loops of the meson and baryon, respectively. Both the integration and the explicite construction of M and B are performed in the SVM.

In [39] the leading contribution of the meson-meson scattering (J_{MM}) was calculated which was found to be purely imaginary and even under C-parity. I.e. the leading term of the scattering amplitude in the SVM can be attributed to Pomeron exchange. Calculations for exclusive vector meson production can be found in [39, 40]. In [41] the next to leading order contribution for the profile function was calculated for the part that is odd under C-parity, which was found to be the leading contribution of the real part of the scattering amplitude, and can thus – analogously to the leading order – attributed to the Odderon.

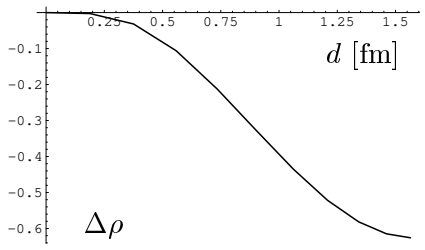

Figure 1.14: $\Delta\rho$ *as function of the diquark distance at UA4/2 energies.*

If the proton is considered as a quark-diquark system with $\alpha = 0$, it effectively becomes a meson which is symmetric under parity operations and the amplitude vanishes. Figure 1.14 shows $\Delta\rho$ as function of the diquark distance $d \sim \alpha$. This behaviour can easily explain the apparent lack of a odd-under-crossing contribution: if one assumes a diquark distance of $d < 0.3$ fm, one obtains $|\Delta\rho| < 0.02$ compatible with $\Delta\rho = 0.04 \pm 0.02$ as measured at the ISR at $\sqrt{s} = 32$ GeV. Turning the argument around, if the Odderon exists and the SVM gives a reliable description of its contribution to the cross section, then one can deduce information of the spatial structure of the proton, viz. that the proton is a quark-diquark system with a diquark distance of $d \lesssim 0.3$ fm.

This suppression due to the geometric configuration of the proton is lifted if the final state is allowed to consist of parts with $C = -1$. In a series of publications this case was presented for the mesons π^0 [42, 43] and $f_2(1270)$ [44]. Once the amplitude has been calculated, the differential cross section can be written as

$$\frac{\mathrm{d}\sigma}{\mathrm{d}t} = \frac{1}{16\pi s^2} \sum_{\lambda_M \lambda_\gamma} |A_{+1,\lambda_M,\lambda_\gamma}|^2 \tag{1.88}$$

$$\approx a \exp(bt - ct^2) \tag{1.89}$$

$$\text{with} \quad a = 97\,\mathrm{nb/GeV^2}, b = 4.8\,\mathrm{GeV^{-2}}, c = 0.52\,\mathrm{GeV^{-4}} \tag{1.90}$$

where the amplitude depends on the three helicities of the excited nucleon ($\lambda = +1$ by construction), the meson λ_M and the photon λ_γ. For photoproduction the centre of mass energy $\sqrt{s}$ is to be identified with the photon-proton centre of mass energy W, which is 20 GeV, where the parameters of the model were fixed. The predicted differential cross sections for f_2 production is presented in figure 1.15. The integration of the differential cross sections (1.88) yields

$$\sigma(\gamma p \xrightarrow{\mathcal{O}} f_2\{2P\}) = 21\,\mathrm{nb}\,, \tag{1.91}$$

where the symbol $\{2P\}$ above is a shorthand notation for the two degenerate nucleon states $N^*(1520)$ and $N^*(1535)$ which are treated as a single state. If the iso-scalar tensor

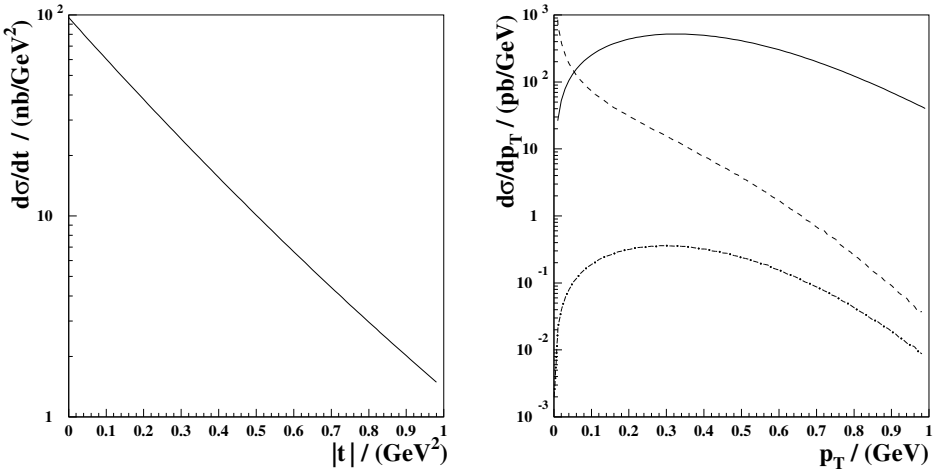

a) b)

Figure 1.15: Differential cross sections for the f_2 in the SVM: *Part a) shows $d\sigma/dt$ and b) $d\sigma/dp_T$ for f_2-mesons. Also shown is the cross sections for the $\gamma\gamma$ fusion process as dashed lines for comparison. In b) the inelastic $\gamma\gamma$ process is shown as dash-dotted line, where the proton is excited into degenerate states $N^*(1520)$ and $N^*(1535)$.*

meson f_2 is produced, it is to expect that the iso-vector a_2^0 is produced as well, but with a cross section nine times larger. The reason for this is thoght to be due to the wave functions at the origin in analogy to the arguments given in [45] for the ρ^0 and the ω. The uncertainty of the cross section given in [44] amounts to a factor of two.

It was found that the dominant contribution from the sum over λ_f comes from the helicity states $\lambda_f = \pm 2$. The background due to the $\gamma\gamma$-processes was found to be small: $\sigma(\gamma p \xrightarrow{\gamma} f_2\{2P\}) \sim 2$ nb for the elastic case and if the proton is allowed to break up, the cross sections is even by a factor of 1000 smaller than the Odderon induced process.

1.7.3 The Eikonal Model of Block et al.

In [46] a model is presented that can simultaneously describe total and elastic cross sections, the angular spectrum and thus the slopes b and the ρ-parameters of pp-, $\bar{p}p$-, γp- and $\gamma\gamma$ interactions, once the parameters were fixed, fitting pp and $\bar{p}p$ data. The model is based on a QCD-inspired eikonal, that consists of even and odd contributions to the scattering, $\chi = \chi_+ + \chi_-$ The even eikonal contains the interaction of quarks with quarks (qq), quarks with gluons (qg) and gluons with gluons (gg) together with a part that is odd under crossing[10].

$$\sigma_{\mathrm{tot}}(pp \to X) = 2 \int \mathrm{d}^2\boldsymbol{b}\,[1 - \exp(-\chi_I(b,s))\cos(\chi_R(b,s))]\,, \tag{1.92}$$

[10] This part odd under crossing, is not to be confused with the Odderon, but accounts for the difference between pp and $\bar{p}p$ scattering at small energies

where the eikonal was split in its real and imaginary part, respectively: $\chi(b,s) = \chi_R(b,s) + i\chi_I(b,s)$. The full form of the eikonal reads

$$\chi(b,s) = \underbrace{\chi_{qq}(b,s) + \chi_{qg}(b,s) + \chi_{gg}(b,s)}_{\chi_+(b,s)} + \chi_-(b,s) \tag{1.93}$$

$$= \sum_i \hat{\sigma}_i(s) W(b,\mu_i) \quad \text{with } i \in \{qq, qg, gg, -\} \tag{1.94}$$

and $\hat{\sigma}_i(s)$ are model cross sections of the colliding partons, where $W(b,\mu)$ is their overlap function in impact parameter space, parameterised as the Fourier transform of a dipole form factor. The μ_i's characterise the partons' sizes in b space.

The model is constructed in a way that unitarity and thus the Froissart bound is satisfied, such that the cross section does not rise faster than $\ln^2 s$ and the hadrons ultimately evolve into black discs of partons. The step from pp to γp (or $\gamma\gamma$) scattering is achieved using vector meson dominance and the additive quark model, i.e. the photon is assumed to consist of two quarks in contrast to the proton, which is modelled as a three-parton object. The parton cross sections $\hat{\sigma}_i$ are dressed with quark counting factors of 2/3 (4/9) and the parton sizes with $\sqrt{2/3}$ (2/3) for γp and $\gamma\gamma$ scattering, respectively. Vector meson dominance is implemented by multiplying the (total) cross section with the transition probability P_{had} for a photon to enter the interaction as a hadron. For the total γp cross section this probability is, according to the VMD model, given by the sum of the vector mesons contributing $P_{\text{had}} = \sum_V 4\pi\alpha/f_V^2$ and for elastic vector meson photoproduction only the corresponding $4\pi\alpha/f_V^2$.

The total γp cross section is thus given by the very same expression as the pp cross section, but multiplied with a factor $P_{\text{had}} = 240$ and the parton cross sections and the μ_i's rescaled with factors of 2/3 and $\sqrt{2/3}$, respectively. And the cross section for elastic vector meson photoproduction is given by

$$\sigma_{\text{el}}(\gamma p \to Vp) = \frac{4\pi\alpha}{f_V^2} \int \mathrm{d}^2\boldsymbol{b} \; |1 - \exp\left(i\chi^{\gamma p}(b,s)\right)|^2 \;, \tag{1.95}$$

with its differential cross section in t given by

$$\frac{\mathrm{d}\sigma^{\gamma p \to Vp}}{\mathrm{d}t} = \frac{4\pi\alpha/f_V^2}{4\pi} \int \mathrm{d}^2\boldsymbol{b} \; \left| J_0(qb) \left[1 - \exp\left(i\chi_I^{\gamma p}(b,s)\right)\right]\right|^2 . \tag{1.96}$$

The eikonal χ has no odd contribution if a photon is involved.

In figure 1.16 the prediction of the model for γp interactions can be seen: part a) shows the total photon-proton cross section, b) and c) the elastic and differential cross section for ω photoproduction, respectively and d) the slopes b as derived from $b = \mathrm{d}/\mathrm{d}t\,[\ln(\mathrm{d}\sigma/\mathrm{d}t)]_{t=0}$ for the light vector mesons

1.7.4 Summary

In the previous sections various models to describe exclusive meson production were presented. In section 1.6.4 a Regge theory based model using vector meson dominance gives a prediction of 1.5 μb for the ω meson in photoproduction at $W = 200$ GeV. The adaptation of the dipole model of Forshaw et al. presented in section 1.7.1 gives for the same γp centre of mass energy a cross section of 2.2 μb and the eikonal model of Block et al. [46] in section 1.7.3 yields 1.7 μb.

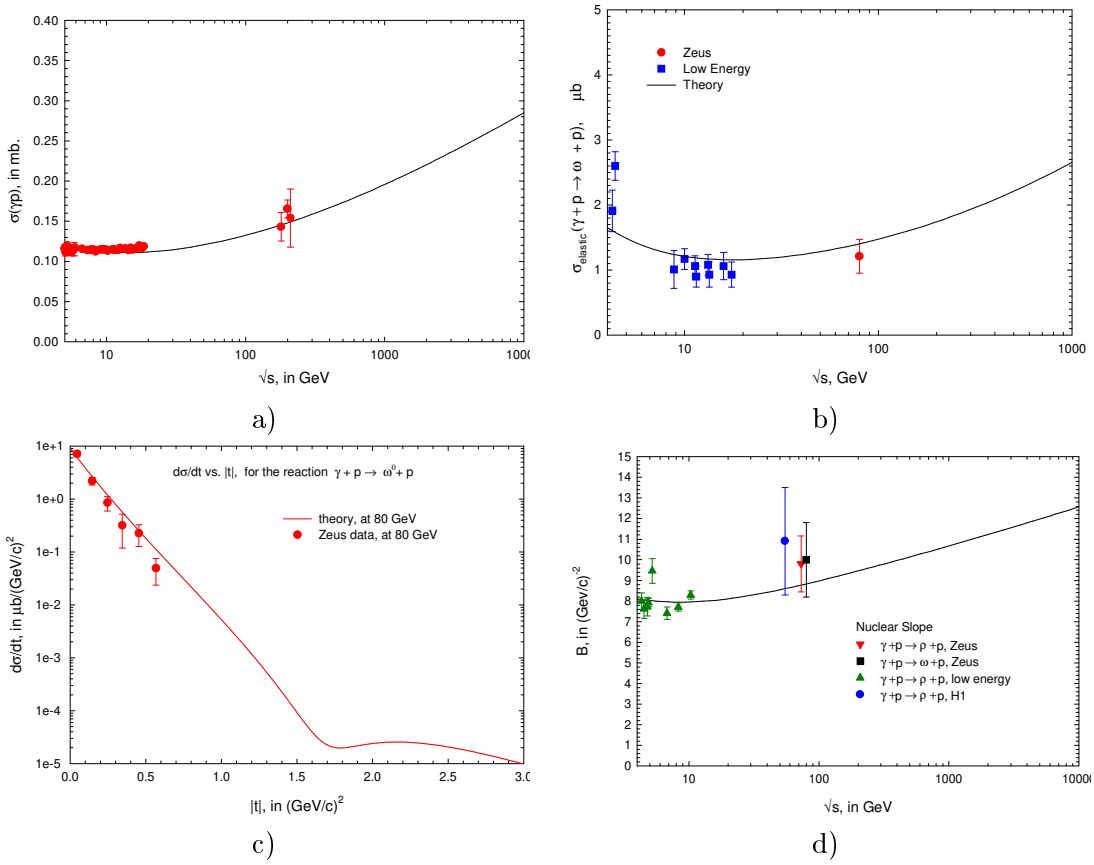

Figure 1.16: Comparison of the eikonal model with γp-data: *a) total photon proton cross section, b) cross section for elastic ω photoproduction, c) differential cross section $d\sigma/dt$ for elastic ω photoproduction and d) slopes b for the light vector mesons ρ^0, ω and ϕ. (Taken from [46])*

The model of the stochastic vacuum, described in 1.7.2 is the only model presented that makes any prediction about contributions of the Odderon. There are published predictions for the inelastic production of the meson π^0 [43] and f_2 [44] of 294 nb and 21 nb, respectively evaluated at $W = 20$ GeV. But as the SVM does not incorporate any energy dependence the intercept of the Odderon is unity and the cross sections at $W = 200$ GeV are the same. Further, the authors of [43] [44] claim that in the same way as the ρ^0 cross section is nine times larger than the one for the ω the cross section for a_2^0 should be nine times larger than the f_2 one, namely 190 nb.

M	$\sigma^{\gamma p \to MX}$	Model	equation	elastic/inelastic
ω	1.5 μb	Regge+VMD	(1.80)	elastic
ω	2.2 μb	dipole+wave functions	(1.84)	elastic
ω	1.7 μb	eikonal	(1.95)	elastic
π^0	294 nb	SVM	(1.88)	inelastic
f_2	21 nb	SVM	(1.88)	inelastic
a_2	9×21 nb	SVM	(1.88)	inelastic

Table 1.4: Summary of cross sections for exclusive meson photoproduction *as presented in sections 1.6.4, 1.7.1, 1.7.3 and 1.7.2. The ω cross sections were evaluated at $W = 200$ GeV and the SVM cross sections at $W = 20$ GeV and an Odderon intercept of unity, i.e. no energy dependence, is assumed.*

1.8 Decay Angular Distributions

When studying decay angular distributions it is customary to measure the angles in a particular reference frame, the so called helicity system, which is defined as the system where the meson is at rest and the z-axis points in the opposite direction of the outgoing nucleonic final state ($\boldsymbol{p}'$) and the y-axis is chosen perpendicular on the plane given by the photon momentum $\boldsymbol{q}$ and the direction of the meson $\boldsymbol{M}$. The x-axis is constructed using the fact that the coordinate system is to be right handed.

$$\hat{\boldsymbol{z}} = -\frac{\boldsymbol{p}'}{|\boldsymbol{p}'|} \quad ; \quad \hat{\boldsymbol{y}} = \frac{\boldsymbol{q} \times \boldsymbol{M}}{|\boldsymbol{q} \times \boldsymbol{M}|} \quad ; \quad \hat{\boldsymbol{x}} = \hat{\boldsymbol{y}} \times \hat{\boldsymbol{z}} \,. \tag{1.97}$$

The decay angular distribution is measured in terms of the azimuthal and polar angles φ^* and ϑ^*, respectively, of one of the decay products. The angles are measured with respect to the coordinate frame (1.97).

In principle the decay angular distribution depends on a further angle ψ^*, the angle between the electron scattering plane and the plane given by the meson and photon momentum. The angles and the respective planes are shown in figure 1.17. For photoproduction where the scattering angle is (vanishingly) small, it is not possible to determine the scattering plane and thus ψ^* cannot be measured and its dependence has to be averaged out.

In appendix C a formalism is presented that can be utilised to derive the decay angular distributions. For the decay of vector meson into a vectorial and a scalar particle the

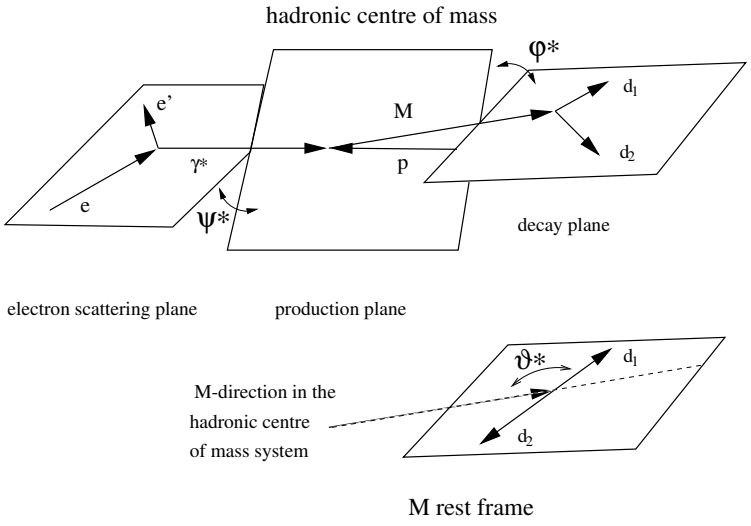

Figure 1.17: Schematic view of the production and decay of a meson M: *The hadronic centre of mass frame and the angles ϑ^*, φ^* and ψ^* are visualised.*

decay angular distribution is given by

$$\frac{\mathrm{d}^2\sigma}{\mathrm{d}\vartheta^*\mathrm{d}\varphi^*} \propto W(\vartheta^*, \varphi^*) = \frac{3}{8\pi}[\rho_{+1+1}(1+\cos^2\vartheta^*) + \rho_{00}\sin^2\vartheta^*]\,, \tag{1.98}$$

where it was assumed that the meson retains the helicity of the photon – also called s-channel helicity conservation. The contribution proportional to ρ_{00} is expected to vanish for real photons and to be small for photoproduction, as it is the part that stems from longitudinal photons.

For tensor mesons produced as predicted in [44] with helicities ± 2 only, the decay angular distribution, is given by

$$\frac{\mathrm{d}^2\sigma}{\mathrm{d}\vartheta^*\mathrm{d}\varphi^*} \propto W(\vartheta^*, \varphi^*) = \frac{75}{64\pi^2}\rho_{+2+2}\sin^4\vartheta^*\,. \tag{1.99}$$

In both cases – for the decay of a vector and for the decay of a tensor – no dependence on the azimuthal angle φ^* is expected.

Chapter 2

The Accelerator HERA and the Experiment H1

The electron proton collider HERA[1], situated at DESY[2] in Hamburg, Germany, is the first and only accelerator to bring leptons and hadrons to collisions. By going from a fixed target experiment to a collider experiment an increase of the centre of mass energy of orders of magnitude has been be achieved.

2.1 The Collider HERA

Figure 2.1 shows a sketch of the HERA ring which is about 6.3 km in circumference and the complex of pre-accelerators. At HERA electrons and protons are accelerated and stored

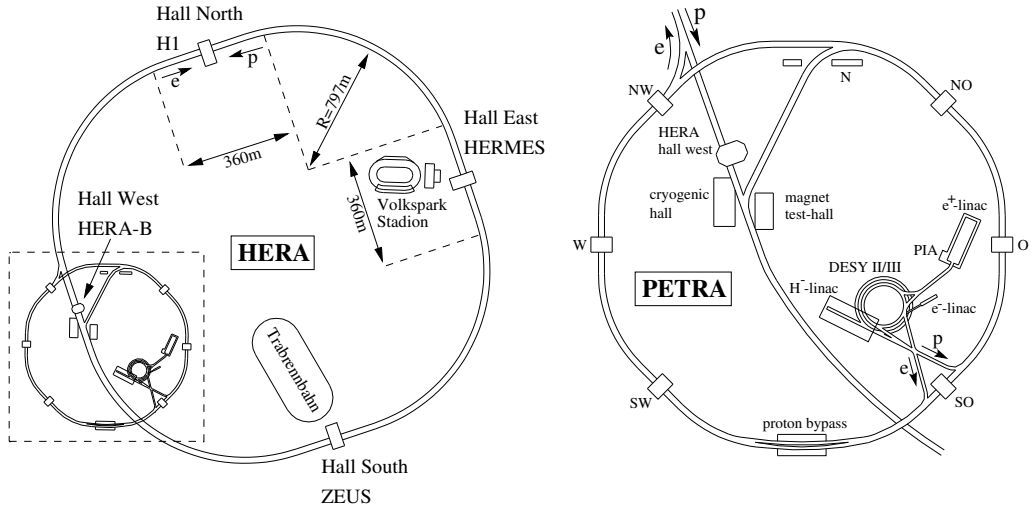

Figure 2.1: *The layout of HERA and its pre-accelerators.*

in two independent rings and can be brought to collision at four interaction regions, where

[1] Hadron Elektron Ringanlage
[2] Deutsches Elektron Synchrotron

only two experiments actually utilise the two beams for interaction, namely the two multi-purpose experiments H1 and the ZEUS. The two other experiments at HERA, HERMES and HERA-B, run as fixed target experiments only. HERMES uses the electron beam to measure the spin structure of the proton by polarising the electrons and using polarised Hydrogen (and Deuterium) as target. HERA-B uses a wire as target for the proton beam to create B^0-mesons which are studied to look for CP violation.

In a series of steps the beam particles are created and accelerated before they are actually injected into the HERA ring where they are accelerated to their final energies. The beams are packed in bunches of 10^{10}–10^{11} particles. Therefore interactions do not occur continuously, but with a frequency given by the length of the gaps in between the bunches; at HERA this frequency is ca. 10 MHz.

2.2 The Experiment H1

The detector H1 is located in the north hall of the HERA ring. Figure 2.2 shows a schematic view of the H1 detector with its components listed in the legend. H1 is a detector designed to cover nearly the full solid angle. The major losses are due to the beam pipe intercepting the detector. A complete description of the H1 detector can be found in [47]. The design reflects the properties of the interactions occurring usually in ep-scattering with asymmetric beams, namely azimuthal symmetry and a strong asymmetry perpendicular to the plane $z = 0$. The reason for this asymmetry are the different beam momenta, so that the centre of mass system moves with a velocity of $\beta = 0.93$ with respect to the laboratory frame in the proton direction, resulting in a strong boost of the particle flux. The inner part of the detector and the main calorimeter of H1, are surrounded by a superconducting coil, creating a uniform magnetic field of 1.15 T along the z-axis forcing charged particles on bent trajectories. The radius of curvature is a measure for the momentum of a particle.

The various components are designed for a clear measurement of the scattered electron and its identification together with a measurement as complete as possible of the hadronic final state emerging from the proton. In the following, the major components are discussed briefly.

2.2.1 The Tracking System

The tracking system serves for the detection and identification of charged particles. The momentum of a particle can be determined from the radius of curvature of its trajectory that it has to move on in the presence of a magnetic field. From the specific energy loss $\mathrm{d}E/\mathrm{d}x$ the velocity of a particle can be determined, and together with its momentum the identity of the particle can be deduced. The interaction point – or event vertex – is also determined by means of reconstructed tracks: The region where most of the tracks intersect each other is likely the region where the interaction occurred.

The strong asymmetry of the beam energies and the resulting strong boost between the laboratory and the centre of mass frame is also reflected in the arrangement of the tracking devices, as can be seen in figure 2.3. Table 2.1 summaries parameters such as angular coverage and resolutions.

The central region is covered by the following components (from the inner to the outer):

- the **C**entral **I**nner **P**roportional Chamber (CIP),

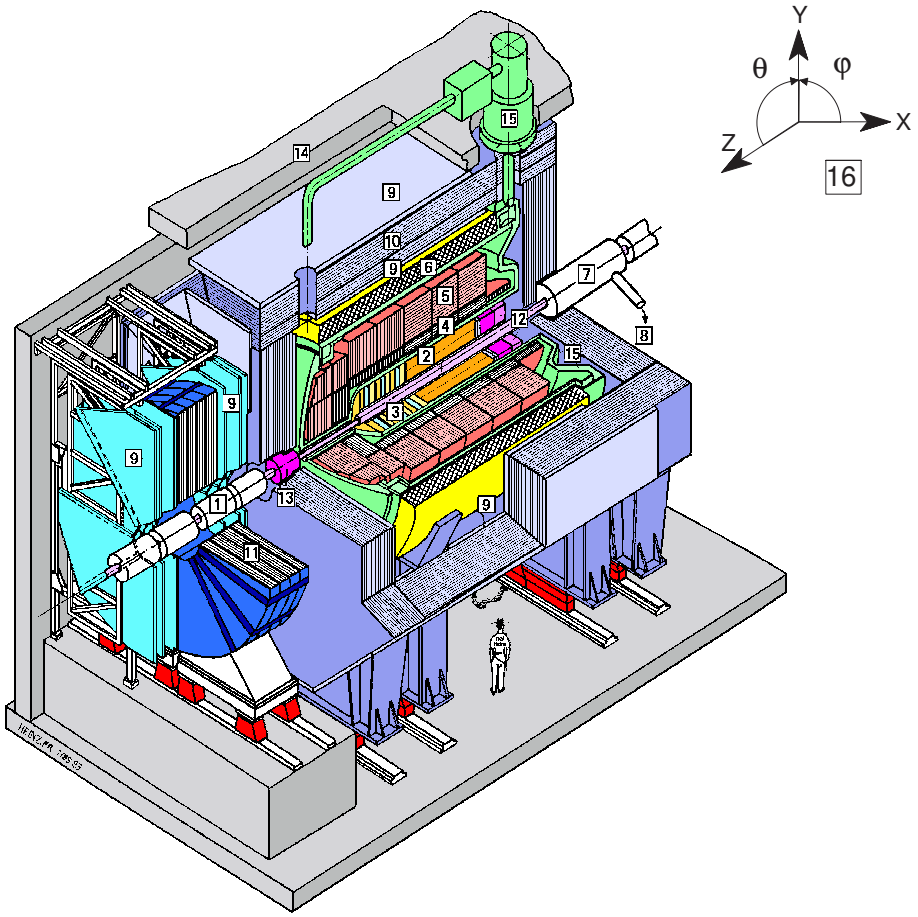

1 Beam pipe and beam magnets
2 Central track detectors
3 Forward track detectors
4 Electromagnetic LAr calorimeter
5 Hadronic LAr calorimeter
6 Superconducting coil (1.15 T)
7 Compensating magnet
8 Helium supply for 7
9 Muon chambers
10 Instrumented iron yoke
11 Forward muon toroid
12 SPACAL and Backward DC
13 Plug calorimeter
14 Concrete shielding
15 Liquid argon cryostat
16 H1 coordinate system

Figure 2.2: *A schematic view of the H1 detector.*

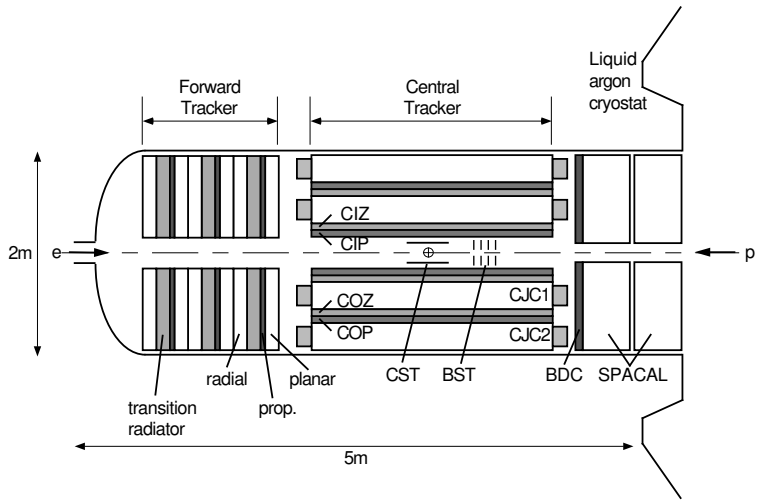

Figure 2.3: *A side view of the tracking system of the H1 detector*

- the **C**entral **I**nner **z**-Chamber (CIZ),
- the **C**entral **J**et **C**hamber **1** (CJC1),
- the **C**entral **O**uter **z**-Chamber (COZ),
- the **C**entral **O**uter **P**roportional Chamber (COP)
- and the outermost **C**entral **J**et **C**hamber **2** (CJC2)

In the forward region there is the **F**orwad **T**racking **D**etector (FTD), built up out of three super modules each consisting of a planar drift chamber, followed by a **M**ulti-**W**ire **P**roportional **C**hamber (MWPC) and completed by a radial drift chamber.

And in the backward region there is the **B**ackward **D**rift **C**hamber (BDC), providing an additional capability to measure the electron at scattering angles low enough to escape detection in the central region. The BDC is used to improve the position measurement of the scattered electron by linking the cluster position to the track found. It is a means to separate electrons from photons.

In the years 1995 and 1996 two silicon trackers were installed very close to the beam pipe to further improve the measurement of the interaction point and the polar angle of the scattered electron in the very backward direction. The former task is fulfilled by the **C**entral **S**ilicon **T**racker (CST) and the latter by the **B**ackward **S**ilicon **T**racker (BST).

2.2.2 The Calorimeters

The calorimeters are used to measure the energies and to some extent also the directions of both charged and neutral particles. A high energetic electromagnetically or strongly interacting particle interacting with matter is the origin of a cascade of secondary particles emerging from this interaction. The summed length of all the particles' trajectories is proportional to the energy of the primary particle and the depth of penetration is proportional to the logarithm of its energy.

	d [mm]	ϑ [°]	$\sigma_{r\varphi}$ [mm]	σ_z [mm]
CIP	157–166	8–172	—	—
CIZ	174–200	16–169	28	0.26
CJC1	203–451	10–170	0.17	22
COZ	460–485	23–157	58	0.20
COP	501–514	25–155	—	—
CJC2	530–844	26–154	0.17	22
FTD	—	5–25	0.21	—
BDC	—	155–175	5	0.4
CST	5.7–9.8	17–163	0.12	0.22
BST	5.9–12	162–176	—	—

Table 2.1: Summary of parameters of the H1 tracking devices: *Given are the radial distances d, the coverage of the polar angle ϑ and the transverse and longitudinal resolutions $\sigma_{r\varphi}$ and σ_z, respectively.*

Due to the fact that electromagnetically and strongly interacting particles develop different showers, calorimeters are often split into two parts, an electromagnetic and a hadronic part. The showers of strongly interacting particles have larger transverse and longitudinal extensions, as in the evolution of a hadronic shower nuclear reactions occur where a hadron hits a nucleon, resulting in its excitation or break-up, whereby pions with larger transverse momenta may be produced compared to particles in electromagnetic interactions .

Table 2.2 summaries the parameters of the major calorimeters of H1.

The Liquid Argon (LAr) Calorimeter is the largest calorimeter of the H1 detector and covers the central and forward regions around the interaction point. The calorimeter consists of roughly 45000 cells and is divided into an electromagnetic and a hadronic part. In z-direction it consists of eight so called wheels, each built up out of eight segments, therefore called octants.

The LAr calorimeter is a sandwich calorimeter where absorber material and active material follow each other in several layers. The active material is liquid argon, and for the electromagnetic part lead is used in contrast to stainless steel in the hadronic part as the passive material.

The electromagnetic calorimeter consists of three layers in the central and seven in the forward region, while the hadronic section consists of four layers in the central region and of six in the forward region.

The PLUG Calorimeter closes the gap in between the beam pipe and the LAr calorimeter in the forward region to minimise losses of particles created with small transverse momenta.

As absorber material copper plates are used with silicon detectors as active material.

The Central Muon System (IRON) encloses the superconducting coil creating the magnetic field. Three layers of so called muon boxes are mounted (from the inner to the outer) right behind the coil, in chambers carved into the iron yoke and right behind the yoke.

Muons with energies larger than 1.5 GeV can reach the central muon system.

	ϑ [°]	X_0	λ	σ_E/E (E in GeV)
LAr (em)	4–153	20–30		$12\%/\sqrt{E} \oplus 1\%$
LAr (had)	4–153		4.5 – 7	$50\%/\sqrt{E} \oplus 2\%$
SpaCal (em)	152–177	28	1	$7.5\%/\sqrt{E} \oplus 1\%$
SpaCal (had)	159–178	29	1	$56\%/E$
PLUG	0.7–3.3	45	4.25	$\approx 150\%/\sqrt{E}$
IRON	4–176		4.5	$100\%/\sqrt{E}$

Table 2.2: Summary of H1-calorimeters: *Given is the coverage of the polar angle ϑ, the thickness in units of interaction lengths X_0 for electromagnetic interactions and in units of hadronic radiation lengths λ together with the relative energy resolution σ_E/E, where E is measured in GeV. [49, 50, 51, 52]*

The Backward Calorimeter SpaCal covers the backward region of H1, and is used to measure the scattered electron at moderate photon-virtualities with high precision. The SpaCal also consists of an electromagnetic and a hadronic section, the former being built up out of 1192 cells with cell-sizes of 4.05×4.05 cm^2 and the latter out of 128 cells sized 12×12 cm^2.

The SpaCal is a sandwich calorimeter with lead as absorber and scintillating fibres 0.5 mm in diameter as active material. The fibres of each cell are collected and connected with a photomultiplier. The lead-to-fibre ratio is 2.3 : 1 for the electromagnetic section and 3.4 : 1 for the hadronic section.

Due to the low noise level of the photomultipliers of 15 MeV per cell, a spatial resolution in the mm region and an energy resolution better than $10\%/\sqrt{E}$, the SpaCal can be used as a tool to perform/make spectroscopy of mesons decaying radiatively, which has been demonstrated successfully in [48] for π^0- and η-mesons. The energy and spatial resolutions were found to be

$$\frac{\sigma_E}{E} = \frac{(7.5 \pm 0.2)\,\%}{\sqrt{E}} \oplus (1.0 \pm 0.1)\,\% \tag{2.1}$$

$$\sigma_{x|y} = \frac{(4.4 \pm 0.5)\,\text{mm}}{\sqrt{E}} \oplus (1.0 \pm 9.2)\,\text{mm}\,, \tag{2.2}$$

with the energy measured in GeV. The symbol $\oplus$ is a shorthand notation for summing quadratically, i.e. $a \oplus b = \sqrt{a^2 + b^2}$. The absolute energy is known with an uncertainty of 4 % in the range of $E < 10$ GeV and around 1 % for higher energies.

2.2.3 Detectors in the Forward Region

The Forward Muon System supplements the central muon system for polar angles of 4° to 17° and is sensitive to muons with $|\boldsymbol{p}| > 5$ GeV.

The Proton Remnant Tagger (PRT) is located at $z = 25$ m to detect particles coming from the fragmentation of the proton rest. Its angular acceptance is in the region of 0.06° to 0.25°.

The Forward Proton Spectrometer (FPS) consists of two special detectors, so called roman pots, located at $z = 80$ m and $z = 90$ m and is used to tag protons or charged

fragments produced with very low transverse momenta and thus under very small angles $\lesssim 3$ mrad.

The Forward Neutron Calorimeter (FNC) is utilised to measure neutrons from the reactions $ep \to e'n + X$. The distance to the nominal interaction point is 110 m. The angular acceptance is substantial only for $\vartheta \lesssim 1$ mrad.

2.2.4 The Luminosity Measuring System

The luminosity L is a property specific for each accelerator, yielding the connection between a cross section σ and the rate of interactions $\dot{N}$:

$$\dot{N} = L\sigma\,. \tag{2.3}$$

Measuring the rate of a particular process with a precisely known cross section thus allows for the determination of the luminosity. At HERA the bremsstrahlung – also called Bethe-Heitler – process $ep \to e'p' + \gamma$ is chosen. For the measurement of this process two detectors in the backward region are utilised, namely a calorimeter at $z = -33$ m for the scattered electron[3] and a calorimeter for the emitted photon at $z = -103$ m under an angle of $\vartheta = 180°$. These detectors are called electron tagger (ET) and photon tagger (PD), respectively. Through the emission of the bremsstrahlung-photon the electron loses energy and is therefore more strongly deflected by the magnets that steer the beams. The beam pipe has special exit windows where the electron and photon may pass the beam pipe wall without too many losses.

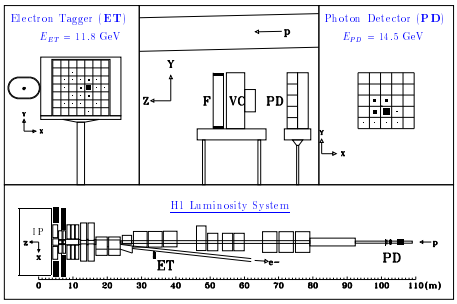

Figure 2.4: The components of the H1 luminosity system: *The components are shown in both transverse and longitudinal projections with a Bethe-Heitler event where the sum of the photon and the scattered electron yield an energy of* 26.3 *GeV, i.e. roughly the beam energy as required.*

Measuring the electron and the photon in coincidence allows for the determination of the total rate R_{tot}. But for the measurement of the luminosity the rate R_0 of background (non ep) events has to be taken into account. This rate can be measured by means of the so called pilot bunches; these are electron bunches that have no corresponding proton bunch. The luminosity is calculated by

$$L = \frac{R_{\text{tot}} - (I_{\text{tot}}/I_0)R_0}{\sigma_{\text{vis}}}\,, \tag{2.4}$$

where I_{tot} and I_0 are the currents of the nominal and pilot bunches, respectively. The quantity σ_{vis} is the known cross section for Bethe-Heitler processes taking into account geometric acceptances and trigger efficiencies. The luminosity system of H1 is shown in figure 2.4 with a Bethe-Heitler event.

2.3 The Trigger System of H1

The H1 trigger is a system designed to separate physically interesting events from so called background events, which can be for example the interaction of beam particles with

[3] There are three further detectors to tag the scattered electron at $z = -7$ m, -8 m and -44 m, respectively. But in the following only the detector at -33 m will be used.

residual gas atoms. This kind of reaction has a rate of more than 100000 events per second throughout the HERA ring.

A further source of background are muons: There are the so called halo muons, stemming from pion decays induced by proton interaction with rest gas or the beam pipe wall, and muons from showers of cosmic rays hitting the earth's atmosphere with a rate of several hundred events per second in the central part of the detector.

The short time of 96 ns between the crossing of the bunches together with the high currents, resulting in a luminosity of $L = 1.5 \cdot 10^{31}\,\mathrm{cm}^{-2}\mathrm{s}^{-1}$ (design value) and the cross sections for the respective reactions gives rise to rates of 20–30 Hz for photoproduction down to a few events per week for events with W-exchange. To record and store all events is not possible, since the readout of the detector takes several milliseconds.

To filter the interesting events the concept of a multi-level trigger was pursued. As shown in figure 2.5 the trigger consists of 5 levels, where the fifth one is not in parallel to the actual data-taking, but off-line.

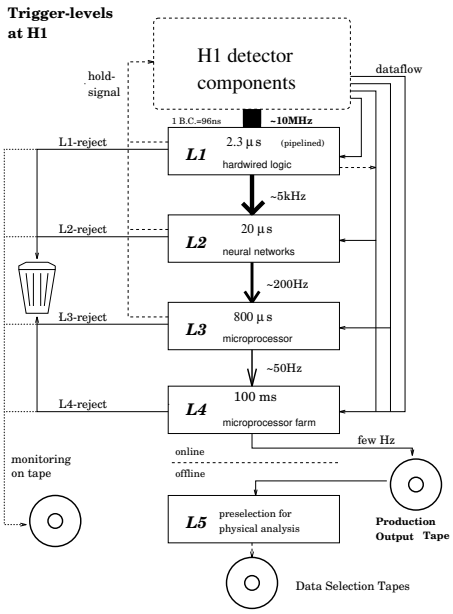

Figure 2.5: The trigger concept of H1: *The figure shows the H1 trigger concept with its 5 levels and the respective input rates entering the various levels.*

In order to keep the dead-time — the time in which the detector cannot take data — as short as possible the detector information is written into pipeline caches and the first trigger level starts to work out its decision.

Level 1 (L1): The output of the "fast trigger branches" can be compared to thresholds and combined logically to up to 128 so called subtriggers. This may not need more than 2.5 μs. To reduce the amount of beam gas interactions, events are accepted only if they occurred inside a time window around a nominal bunch crossing. Is one of the subtriggers set to true — it is said to fire — the pipelines are stopped and the detector is started to be read out[4] and simultaneously the second level is started. For L1 to run without dead-time it has to work with a rate of 10 MHz.

Level 2 (L2): This trigger level consists of two parts, the so called topological trigger (L2TT) and a neural network (L2NN). In contrast to L1 which concentrates on detector components, L2 analyses data provided by L1 with more complex algorithms to further reduce the amount of background and to check the physics relevance of an event. It takes ca. 20 μs for L2 to reject or accept an event.

Level 3 (L3): This level has not been implemented yet.

Level 4 (L4): This part of the trigger consists of 32 processors running in parallel and asynchronously all having access to the full detector information. Besides a further reduction of the background, L4 serves also as an instance of monitoring and calibration. The output rate of L4 is roughly 10 Hz, the rate with which the events are written on tape. From 1997 on L4 was further used to run so called physics finders,

[4] Unless this particular subtrigger is prescaled, i.e. only every p-th event is actually accepted for a prescale of p.

which are routines that require special conditions be fulfilled. Only if an event is accepted by at least of the finders it is actually written to tape.

Level 5 (L5) is no online trigger anymore, but runs the full event reconstruction together with the latest set of calibration constants and classifies the events into classes according to their physics content (DIS, photoproduction, etc.). Events are accepted only if they are classified as belonging of one of the above classes.

Chapter 3

Selection of the Events, Trigger, Trigger-Efficiencies, Reconstruction of the Variables

Due to the large amount of data and the great variety of processes, it is common to analyse a subset of all data only. This set is chosen ideally as small as possible, still being a superset of the set of events comprising the process to be studied.

The processes $\omega \to \pi^0\gamma$ and $f_2 \to \pi^0\pi^0$ to be analysed, lead to three and four photons, respectively in the final state (not counting the scattered beam particles). As only the kinematic regime of photoproduction is studied, the electron is deflected only very weakly and mainly looses energy and obtains hardly any transverse momentum, implying that the photon also has only small transverse momentum. The interaction with the proton adds only rather little to this, so the mesons are produced mainly parallel to the electron direction. This kinematic configuration results in a strong boost of the decay products in the backward direction with only a small transverse component.

To select this kind of topology one requires energy in the SpaCal (to detect the photons of the meson decay) and the scattered electron detected in the electron tagger supplemented by additional conditions to reduce the size of the set. So the basic criterion to select events was the subtrigger S50 to have fired, where S50 requires some activity in the SpaCal as well as activity in the electron tagger. The precise definition of S50 is given by

$$\text{S50} \quad = \quad \begin{cases} \texttt{(SPCLe\_IET>1 || SPCLe\_IET\_Cen\_2) \&\& eTAG} & \text{on Level 1} \\ \texttt{SPCL\_R20} & \text{on Level 2} \end{cases} , \tag{3.1}$$

where[1] the symbols '||' and '&&' stand for a logical 'or' and 'and' ($\vee$ and $\wedge$ mathematically), respectively.

The L1 condition `SPCLe_IET>1||SPCLe_IET_Cen_2` is true, if the L1-estimator of the cluster fulfils $\hat{E} > 2$ GeV and `eTAG` is true, if the energies measured in the electron and photon detector fulfil $E_{ET} > 4$ GeV and $E_{PD} < 2$ GeV, respectively. This L1 setting had to be supplemented by the L2 (L2TT) condition `SPCL_R20`, demanding the cluster to have a transverse distance d larger than 20 cm, because of strong beam activity near the beam pipe – called "hot spot". This requirement largely reduces the efficiency of this subtrigger for both analyses due to the small transverse momenta of the mesons.

[1] including correct timing validated by the time-of-flight information, to ensure that the event stem from a nominal bunch crossing and no particles come from behind or from ahead the H1 detector

The kinematics of the events allows for a further condition be fulfilled, namely the whole final state (except for the proton) be contained in the SpaCal and the electron tagger. This can be rephrased as $\Sigma_{\mathrm{SpaCal+eTag}} \in (40, 70)$ GeV, what is just another way to demand energy momentum conservation.

The decay channels are chosen such that there are only photons in final state, and thus there are no tracks expected that would give rise to a reconstructed interaction point. Thus the events selected must not have a vertex either.

To ensure an acceptable quality of the data, only events that were labelled as 'good' or 'medium' were accepted, i.e. the main components of the H1 detector like the lAr, the SpaCal and the jet chambers, had to be operational. To reduce the amount of beam-induced background it was further required that the events occurred in phase 2 or later. The inelasticity y was required to be in a range where the electron tagger had reasonable acceptance, namely $y \in [0.3, 0.7]$ and the impact point of the scattered electron had to lie in a volume where shower leakage is negligible ($|x_{\mathrm{eTag}}| \leq 6.5$ cm). Since the analyses presented in the following are concerned only with three- and four-photon final states, the number of clusters in the SpaCal was not allowed to exceed ten. The selection criteria are summarised in table 3.1.

$\Sigma_{\mathrm{SpaCal+eTag}} \in (40, 70)$ GeV
no reconstructed vertex
$y \in [0.3, 0.7]$
$\lvert x_{\mathrm{eTag}} \rvert \leq 6.5$ cm
$N_C \leq 10$
phase > 1
quality $\in \{\mathrm{good}, \mathrm{medium}\}$

Table 3.1: Event Selection Summary: *A summary of the requirements to select events is shown.*

3.1 Efficiency of the IET-part of the Subtrigger S50

The efficiency of S50 was determined using a different subtrigger, namely S43=`eTAG && zVtx_sig_1 && DCRPh_Ta` relying the electron tagger and on tracks only. To determine the efficiency $\epsilon(x)$ $(x = E, d)$, a sample was chosen with S43 set and a single cluster in the SpaCal. The efficiency ϵ in a given bin in x was then calculated as the number of events fulfilling the conditions required by S50 divided by number of events having set S43 $\epsilon = N_{S50}/N_{S43}$. The error was calculated as

$$\Delta\epsilon = \frac{\sqrt{N_{S43}\epsilon(1-\epsilon)}}{N_{S43}} \tag{3.2}$$

if $N_{S43} \neq N_{S50}$ and as a lower limit for a 67 % confidence level is used instead if $N_{S43} = N_{S50}$:

$$\epsilon > \Delta\epsilon = (1 - 0.67)^{1/N_{S43}} \tag{3.3}$$

Figure 3.1 shows the distributions of the energy (a) and and the distance (b) for events triggered by S43 as dashed line and if accepted also by S50 as full line. For the energy

distribution the distance was demanded to be larger than 25 cm in order to have the L2 condition always verified. For the distance distribution the energy had to exceed 3 GeV to be independent of the IET condition. Parts c) and d) of figure 3.1 show the ratios of the above distributions, i.e. the efficiencies. The efficiencies were fitted with

$$\epsilon(E) = \frac{p_0}{\exp\left(\frac{p_1 - E}{p_2}\right) + 1} \quad \text{and} \quad \epsilon(d) = \frac{q_0}{\exp\left(\frac{q_1 - d}{q_2}\right) + 1}, \tag{3.4}$$

respectively. The results of the fits are given in table 3.2

$\epsilon(E)$		$\epsilon(d)$	
p_0	0.98±0.02	q_0	0.98±0.01
p_1	2.16±0.03	q_1	15.24±0.29
p_2	0.14±0.02	q_2	1.65±0.23
$\chi^2/N_{df} = 6.95/26$		$\chi^2/N_{df} = 7.44/26$	

Table 3.2: Summary of fitted paramters for the trigger efficienies: *The table shows the paramters and their errors when equation (3.4) is fitted to the data. The parameters p_i refer to the efficiency of the energy and the q_i refer to the efficiency of the distance.*

Figure 3.2 shows the distributions of events triggered by S43 (a) and accapted additionally by S50 (b) as a function of both the energy and the distance, without any further restrictions. Part c) of figure 3.2 displays the ratio of the two former distributions, while part d) visualizes the product of the efficiencies $\epsilon(E)$ and $\epsilon(d)$ as parametrised by:

$$\epsilon(E,d) = \frac{\sqrt{p_0 q_0}}{\left[\exp\left(\frac{p_1 - E}{p_2}\right) + 1\right]\left[\exp\left(\frac{q_1 - d}{q_3}\right) + 1\right]}. \tag{3.5}$$

The geometric mean of the p_0 and q_0 is chosen as parameter to describe the efficiency in saturation.

This efficiency is applied to the Monte Carlo events as weight, where the weight is given by the total probability for an event to have set the trigger:

$$w_{\text{SpaCal}} = 1 - \prod_{i=1}^{N_C} \left(1 - \epsilon(E,d)\right) . \tag{3.6}$$

The product runs over all clusters reconstructed in the SpaCal.

3.2 Acceptance of the Electron Tagger

The acceptance of the electron detector (α_{eTag}) as function of y is measured during data-taking and is shown in figure 3.3. This limited acceptance is also taken into account by applying its value, $w_{\text{eTag}} = \alpha_{\text{eTag}}(y)$, as weight to the Monte Carlo events in addition to the efficiency of the SpaCal-part of the trigger:

$$w_{\text{S50}} = w_{\text{eTag}} \cdot w_{\text{SpaCal}} \tag{3.7}$$

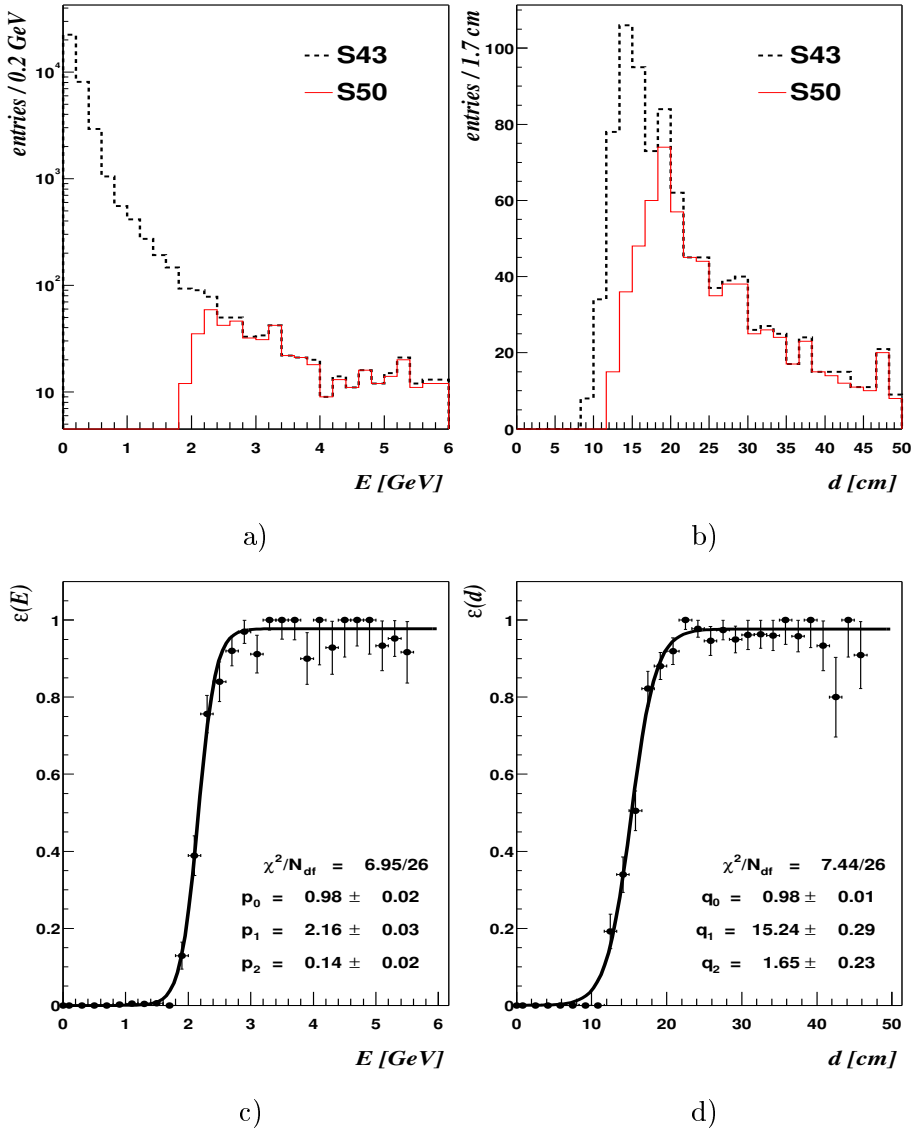

Figure 3.1: IET-efficiencies (I): *Parts a) and b) show the energy and distance distributions, respectively. Events triggered by S43 are shown as dashed lines and as full lines when they were accepted by S50 additionally. For a) it was required that d be larger than 25 cm where the L2 condition is expected to be fully efficient. In b) it was required that E be larger than 3 GeV, where the* IET *condition is expected to be fully efficient.*
Parts c) and d) show the ratios of the above distributions together with fits of equation (3.4)

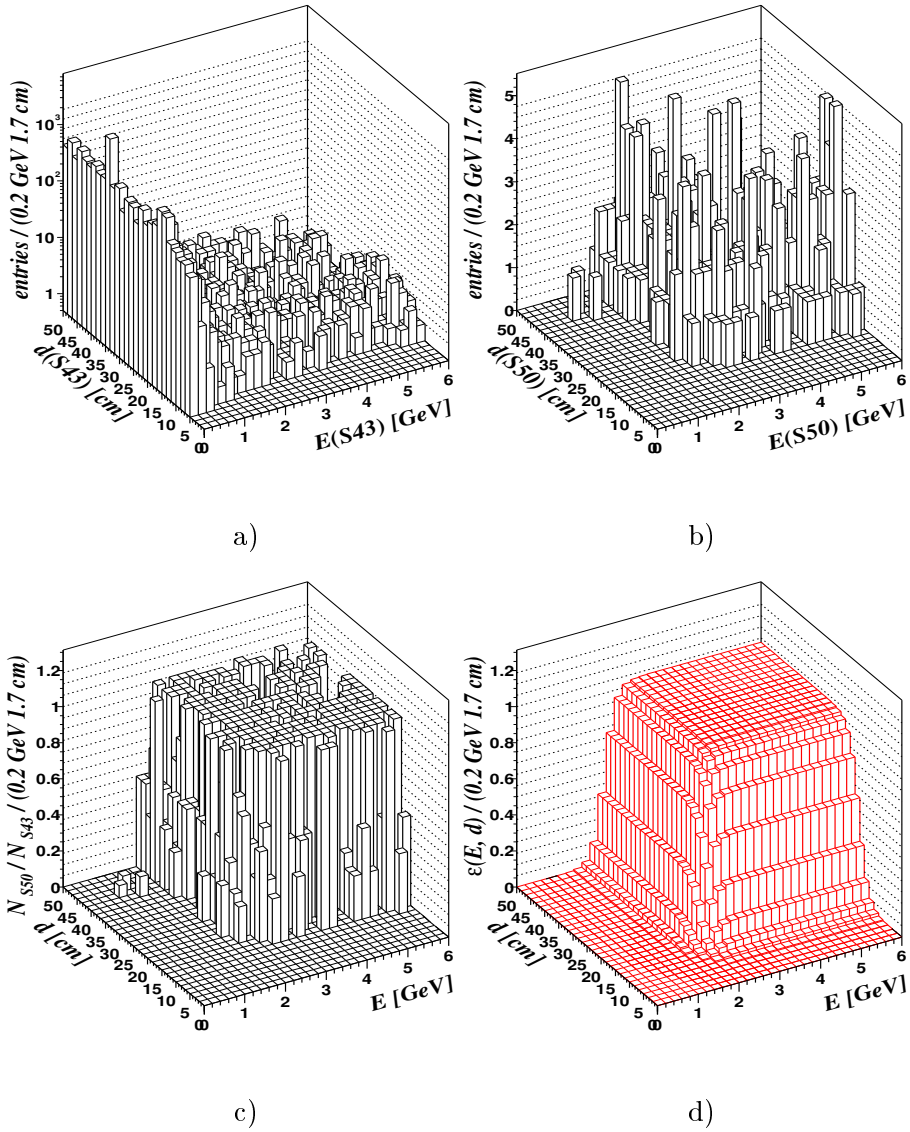

Figure 3.2: IET-efficiencies (II): *Parts a) and b) show the two-dimensional distributions of events triggered by S43 and additionally accepted by S50, respectively.*
Part c) shows the ratio of the distributions shown in a) and b). In part d) equation (3.5) is visualised using the parameters determined with equation (3.4) fitted to the distributions of figure 3.1 c) and d).

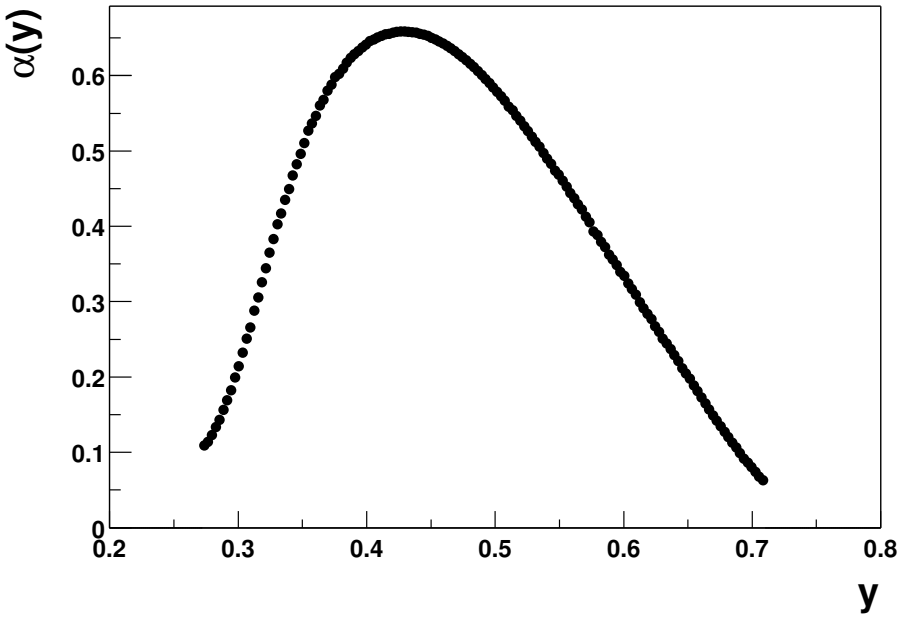

Figure 3.3: eTAG-efficiency: *The acceptance of the electron detector of the luminosity system located at $z = -33$ m as a function of y.*

3.3 Stability of the Trigger S50

The stability of S50 is shown in figure 3.4, where a) shows the accumulated number of events (N) as a function of the integrated luminosity ($\mathcal{L}$), b) shows the ratio $N/\mathcal{L}$ as a function of the run number and c) shows the frequency distribution of $N/\mathcal{L}$.

3.4 Reconstruction of the Kinematic Variables

With the physics and the detector components relevant for the analyses presented in chapters 5 and 6 it is here where the reconstruction of the variables needed is discussed.

There exist various methods [53] to reconstruct the variables described in section 1.1:

- The electron method, where the kinematics of an event is determined by measuring the scattered electron only,
- the Jacquet-Blondel (or hadronic) method, using the hadronic final state emerging from the interaction, except for the proton or its remnant,
- the Σ method being a mixture of the electron and the Jacquet-Blondel method,
- and the double angle method utilising the polar angle of the electron and the so called inclusive hadron angle.

Each method has its advantages and weaknesses in the various regions of phase space such that depending on the analysis performed, the one best suitable has to be chosen. As in

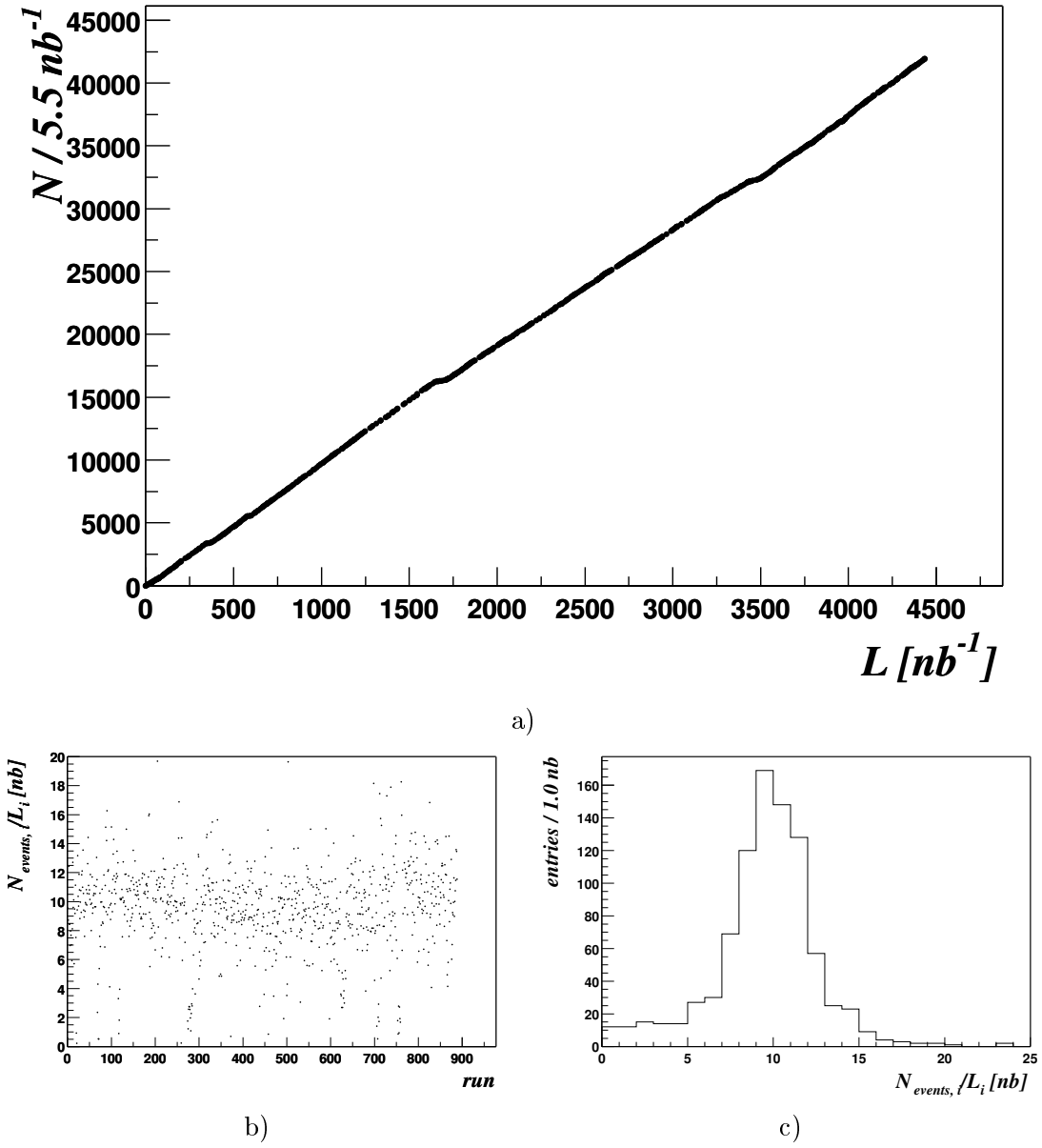

Figure 3.4: Stability of S50: *Part a) shows the number selected events (N) as function of the accumulated luminosity ($\mathcal{L}$), b) shows the ratio $N/\mathcal{L}$ of events per run as function of the run number and c) shows the frequency distribution of the ratio $N/\mathcal{L}$.*

this work only small (or vanishing) scattering angles occur, where the electron method is best, it is the only one described explicitely:

Having measured the scattered electron with energy E'_e and polar angle ϑ_e the inelasticity and Q^2 are given by (neglecting the masses of both the electron and the proton)

$$y = 1 - \frac{E'_e}{E_e} \sin^2 \vartheta_e/2 \,, \tag{3.8}$$

$$Q^2 = 4 E_e E'_e \cos^2 \vartheta_e/2 \quad \text{and} \tag{3.9}$$

$$x = \frac{E_e E'_e \cos^2 \vartheta_e/2}{E_p \left(E_e - E'_e \sin^2 \vartheta_e/2\right)} \,, \tag{3.10}$$

respectively. Since only photoproduction events, where the electron is hardly deflected and $\vartheta_e \approx 180°$, are selected, equations (3.8) – (3.10) simplify significantly, in the approximation $\vartheta_e = 180°$:

$$y \approx 1 - \frac{E'_e}{E_e} \,, \tag{3.11}$$

$$Q^2 \approx 0 \quad \text{and} \tag{3.12}$$

$$x \approx 0 \,, \tag{3.13}$$

The photon-proton centre of mass energy for $Q^2 \to 0$ can be approximated by

$$W = \sqrt{ys} \,. \tag{3.14}$$

The four momentum transfer squared at the proton vertex, described by the variable t can not be reconstructed directly as the scattered proton is in general not detected and t is reconstructed using the momentum of the reconstructed final state. In the case of exclusive photoproduction of mesons t can be well approximated by the transverse momentum of the meson:

$$t = - \left(\boldsymbol{p}_{\perp,M}\right)^2 \,, \tag{3.15}$$

since in photoproduction the electron carries no transverse momentum and all the transverse momentum of the scattered proton has to be balanced by the meson. The four momentum of a meson M is calculated by the sum of its decay products, where it is assumed that M decays into n photons:

$$p_M = \sum_{i=1}^{n} p_i \,. \tag{3.16}$$

The four momenta of the photons are calculated by

$$p_i = E_i \left(1, \sin\vartheta_i \cos\varphi_i, \sin\vartheta_i \sin\varphi_i, \cos\vartheta_i\right) \,, \tag{3.17}$$

where the angles are reconstructed as

$$\vartheta_i = \arctan\left(\frac{\sqrt{\Delta x_i^2 + \Delta y_i^2}}{\Delta z_i}\right) \quad ; \quad \varphi_i = \arctan\left(\frac{\Delta y_i}{\Delta x_i}\right) \,, \tag{3.18}$$

with

$$\Delta x_i = x_i - x_0 \quad ; \quad \Delta y_i = y_i - y_0 \quad ; \quad \Delta z_i = z_i - z_0 \,.$$

The coordinates with index i correspond to the impact points of the photons in the detector. The coordinates bearing the subscript '0' refer to the interaction point, that is

actually not measured in the analyses presented, but a nominal position is determined during data taking.

The mass squared of an n-photon final state is calculated by

$$m_M^2 = m_{n\gamma}^2 = \left(\sum_{i=1}^{n} p_i\right)^2 = \left(\sum_{i=1}^{n} E_i\right)^2 - \left(\sum_{i=1}^{n} \boldsymbol{p}_i\right)^2 \tag{3.19}$$

Chapter 4

Monte Carlo Models

For a measurement of a cross section the acceptances of the process to be measured have to be determined, and the amount of expected background has to be known or estimated. Both tasks are accomplished by computer programmes – so called Monte Carlo programmes – generating interactions of a certain class, that subsequently are passed to another programme that simulates the detector and its imperfections. A third programme is then used to convert the result of the detector simulation into the very same format in which the experimental data are stored.

For the analyses presented in this thesis mainly three event generators are used, where two (DIFFVM[1] and ODDPIUM[2]) are used for describing the signal processes and one (PYTHIA) is used as an estimator for the background.

4.1 Event Generators

4.1.1 The Generator DiffVM

DIFFVM [54] is used to describe diffractive ω photoproduction as presented in chapter 5. The generator was designed to describe diffractive photo- and electroproduction of vector mesons employing Regge phenomenology and vector meson dominance as described in sections 1.5 and 1.6.4. The photons entering the interaction are treated as described in section 1.2.1. And in addition the γp cross sections are dressed with a propagator factor of $(1 + Q^2/\Lambda^2)^{-n}$ with $n = 2.5$ for both transverse and longitudinal photons, to account for the Q^2 dependence of the flux of virtual photons. The ratio of longitudinal to transverse γp cross sections $R(Q^2)$ is modelled as (with $\Lambda = m_V$)

$$R(Q^2) = \frac{\sigma_L^{\gamma p}}{\sigma_T^{\gamma p}} = \frac{\xi \frac{Q^2}{m_V^2}}{1 + \chi \xi \frac{Q^2}{m_V^2}}\,, \tag{4.1}$$

where ξ is a constant factor and χ is purely phenomenological factor to keep $R(Q^2)$ finite for $Q \to \infty$, so that the limiting behaviour of $R(Q^2)$ is

$$R(Q^2) \overset{Q^2 \to 0}{\longrightarrow} \xi \frac{Q^2}{m_V^2} \quad \text{and} \quad R(Q^2) \overset{Q^2 \to \infty}{\longrightarrow} \frac{1}{\chi}\,. \tag{4.2}$$

[1] for **DIFF**ractive **V**ector **M**eson production
[2] for **O**dderon **P**omeron **I**nduced **U**nified **M**eson maker

For the photon virtualities considered here, $Q^2 < 0.01$ GeV^2, the actual setting of these parameters are irrelevant.

The masses m of the ω-mesons are generated according to a non-relativistic Breit-Wigner function

$$\frac{\mathrm{d}\sigma}{\mathrm{d}m} \propto \frac{\Gamma_{\mathrm{tot}}^2}{(m - m_\omega)^2 + \Gamma_{\mathrm{tot}}^2/4}\,, \tag{4.3}$$

$m_\omega = 783$ MeV [32] being the nominal mass and $\Gamma_{\mathrm{tot}} = 8.44$ MeV [32] the total width of the ω.

The differential cross section $\mathrm{d}\sigma/\mathrm{d}|t|$ is modelled as an exponential $\exp(-b|t|)$ according to equation (1.64) with input parameters $b_0 = 10.7$ GeV^{-2} and $W_0 = 80$ GeV as measured in [11], resulting in an expected slope of $b = 10.9$ GeV^{-2} at $W = 200$ GeV.

As described in section 1.8, the decay angular distributions $\mathrm{d}\sigma/\mathrm{d}\cos\vartheta^*$ and $\mathrm{d}\sigma/\mathrm{d}\varphi^*$ for $\omega \to \pi^0\gamma$ are generated, assuming s-channel helicity conservation, according to

$$\frac{\mathrm{d}\sigma}{\mathrm{d}\cos\vartheta^*} \propto (1 + \cos^2\vartheta^*) \quad \text{and} \quad \frac{\mathrm{d}\sigma}{\mathrm{d}\varphi^*} = \text{const}\,. \tag{4.4}$$

4.1.2 The Generator OLPium

OLPium is an extension of DiffVM to incorporate Odderon processes as well. The generator is used to describe the signal expected for an f_2 produced according to the SVM as described in [44], whereas the excitation of the proton into an N^* is not included. The SVM enters only via the different t-distribution that contains an additional quadratic term in the exponential, $\exp(-b|t| + c|t|^2)$ (see section 1.7.2), as compared to the Pomeron case. In addition to that, the f_2 and its properties have to be included: The masses are generated following a relativistic Breit-Wigner function for spin-2 particles:

$$\frac{\mathrm{d}\sigma}{\mathrm{d}m} \propto \left(\frac{m_{f_2}}{m}\right)^2 \frac{\Gamma_{\mathrm{tot}}(m)}{(m^2 - m_{f_2}^2)^2 + m_{f_2}^2\Gamma_{\mathrm{tot}}^2(m)}\,, \tag{4.5}$$

where m denotes the mass generated and $m_{f_2} = 1275$ MeV [32] the nominal mass of the f_2 meson and the total width is denoted by $\Gamma_{\mathrm{tot}} = 185$ MeV[32] . The dependence on the mass is parameterised as in [55] for the $\gamma\gamma$ process according to

$$\Gamma_{\mathrm{tot}}(m) = \Gamma_{\mathrm{tot},0}\frac{m_{f_2}}{m}\left(\frac{q^*}{q_0^*}\right)^{2L+1}\frac{D_L(q_0^* r)}{D_L(q^* r)} \qquad ; \quad L = 2\,, \tag{4.6}$$

where q^* and q_0^* are the pion momenta in the $\gamma\gamma$ centre of mass system, and for $m = m_{f_2}$, respectively. The function $D_L(q^* r)$ is a decay form factor and for $L = J = 2$ it is given by

$$D_2(q^* r) = 9 + 3(q^* r)^2 + (q^* r)^4\,, \tag{4.7}$$

with the effective interaction radius r assumed to be 1 fm.

For the decay angular distributions a behaviour of

$$\frac{\mathrm{d}\sigma}{\mathrm{d}\cos\vartheta^*} \propto (1 - \cos^2\vartheta^*)^2 \quad \text{and} \quad \frac{\mathrm{d}\sigma}{\mathrm{d}\varphi^*} = \text{const} \tag{4.8}$$

is assumed as described in section 1.8. Events for the a_2^0 were generated as well, as it is assumed that the a_2^0 is produced in the very same way as the f_2 but with a cross section nine times larger due to arguments analogous to the reasoning that yield a ratio of cross

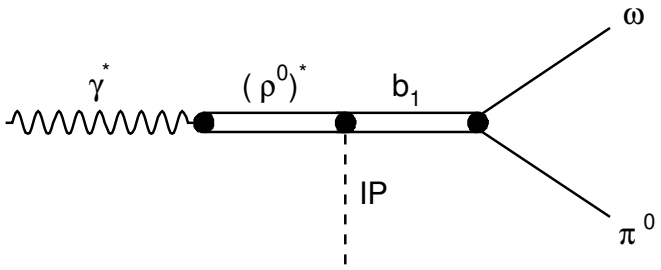

Figure 4.1: Photoproduction of the b_1: *A (quasi-) real photon turns into a virtual ρ^0 which in the following interacts with the proton via Pomeron exchange that mediates one unit of angular momentum. The product of this interaction is a b_1 decaying into a $\omega\pi^0$ system.*

sections for the ρ^0 and ω of nine [45]. The mass and width of the a_2^0 were chosen as $m_{a_2} = 1318$ MeV and $\Gamma_{\mathrm{tot},0} = 107$ MeV [32], respectively.

A further extension included in DIPSY is the exclusive production of b_1 mesons as shown in figure 4.1. As shown in [2] the b_1 is a strong candidate to produce exclusive five photon final states via the decay

$$b_1 \to \omega\pi^0 \to (\pi^0\gamma)\pi^0 \to 5\gamma\,.$$

The shape of the mass-distributions is described by a relativistic Breit-Wigner function for spin-1 particles:

$$\frac{\mathrm{d}\sigma}{\mathrm{d}m} \propto \frac{m m_{b_1}\Gamma_{\mathrm{tot}}(m)}{(m^2 - m_{b_1}^2)^2 + m_{b_1}^2\Gamma_{\mathrm{tot}}^2(m)}\,, \tag{4.9}$$

with the nominal b_1 mass $m_{b_1} = 1230$ MeV [32] , the mass generated m and the total width $\Gamma_{\mathrm{tot}}(m)$. The dependence on the mass is parameterised as in [56] according to

$$\Gamma_{\mathrm{tot}}(m) = \Gamma_{\mathrm{tot},0}\left(\frac{q^*}{q_0^*}\right)^{2L+1}\frac{2}{1+q^*/q_0^*} \quad ; \quad L = 1\,, \tag{4.10}$$

with $\Gamma_{\mathrm{tot},0} = 142$ MeV [32] denoting the nominal width and where q^* and q_0^* are the momenta of the primary decay products in their centre of mass system, and for $m = m_{b_1}$, respectively. For the differential cross section $\mathrm{d}\sigma/\mathrm{d}|t|$ also a simple exponential $\exp(-b|t|)$ with $b = 5.7$ GeV^{-2} was used.

The considerations on the decay angular distribution of section 1.8 are not valid in the case of b_1 production, since, as one unit of angular momentum is transferred, the helicity of the b_1 is not the same as the incoming photon. Due to lack of information of this process the most simple assumption was used and the decay angular distributions were assumed to be flat.

For the decay of the b_1 it is assumed that it decays dominantly into $\omega\pi^0$ [32]. For this two subsequent decay channel were considered:

$$b_1 \to \omega\pi^0 \to \begin{cases} (\pi^0\gamma)\pi^0 & \to & 5\gamma & 8.3\,\% \\ (\pi^+\pi^-\pi^0)\pi^0 & \to & \pi^+\pi^-4\gamma & 86.7\,\% \end{cases},$$

with the branching ratios taken from [32]. The decay into charged pions had to be included as well, since it contributes largely to the background in the lower photon multiplicities, because of the large branching ratio for the decay $\omega \to \pi^+\pi^-\pi^0$ of roughly 88 %.

4.1.3 The Generator to Describe the Background: Pythia

PYTHIA [57] is a multipurpose event generator with emphasis on multi-particle production. It is used here to describe the background stemming from high-multiplicity[3] photoproduction events. The physics model employed by the programme to describe photoproduction is briefly described in section 1.5 and in more detail in [36, 5]. Not all of the events generated were actually written to disk to save space and time, since the number of events that give rise to a vertex amounts to roughly 84 % and the processes to be analysed are expected to have no vertex as these final states consist of photons only and should not produce any tracks leading to a vertex. A further condition to reduce the amount of events written out, is to consider only the regions where the calorimeters are located that are used in the analyses and require energy-momentum conservation for these regions of the solid angle exclusively, i.e. reject events that deposit a large amount of their energy neither in the SpaCal nor in the electron tagger. This results in a further reduction down to about 13 %. In order to apply these requirements to the events generated the following two variables are introduced:

$$v_{\text{gen}} = \begin{cases} 1 & \text{if } N_{\pm} \geq 1 \text{ with } \vartheta_{i,\pm} \in [0.087, 2.915] \\ 0 & \text{otherwisse} \end{cases} \tag{4.11}$$

$$\Sigma_{\text{gen}} = \sum_{\vartheta_i \in [2.65, 3.12]} (E_i - p_{i,z}) + (E'_e - p'_{z,e}) \,, \tag{4.12}$$

where the superscript '$\pm$' in equation (4.11) denotes charged (and stable) particles and the sum in equation (4.12) extends over stable particles only. An event was written out, only if

$$v_{\text{gen}} = 0 \quad \text{and} \quad \Sigma_{\text{gen}} > 40\,\text{GeV} \,. \tag{4.13}$$

In contrast to the above generators PYTHIA allows for dissociative events. A fraction of these dissociative events, namely the photon-dissociative ones, sometimes do not consider isospin and C-parity explicitely, since their decay is modelled in a simplified manner. In the course of these events the photon turns into a vector meson and is subsequently excited diffractively into a state called V_{diff} ($V = \rho^0, \omega, \phi$) as sketched in figure 4.2. It is for $m^2_{V_{\text{diff}}} < (|\boldsymbol{p}_{V_{\text{diff}}}| + \hat{m})^2$ with $\hat{m} = 1$ GeV that this routine is utilised by PYTHIA. The effect of these decays is exemplified in figure 4.3, where PYTHIA is compared to data for $\pi^0\gamma$- and $\pi^0\pi^0$-final states, in the left and right column, respectively.

Parts a) and b) shows PYTHIA including all of the V_{diff}-mesons for the $\pi^0\gamma$ and $\pi^0\pi^0$ final states, and clearly overestimates the respective cross sections. The second row shows PYTHIA when events containing decays like $\rho^0_{\text{diff}} \to \pi^0\pi^0$ are removed from the set of events analysed. The full list of such events is shown in table 4.1. A different approach as pursued in [1, 3] is to remove all events were one of these diffractive states is produced. This scenario is shown in parts e) and f) of figure 4.3. The difference in the two approaches to modify PYTHIA is for the $\pi^0\gamma$-sample only marginal, while it is somewhat more pronounced for the $\pi^0\pi^0$-sample. Due to the fact that the latter approach incorporates the best knowledge it is pursued as the default choice for PYTHIA.

From the left part of figure 4.3 it is apparent that PYTHIA has severe problems describing the absolute normalisation, especially in the region of the ω-peak. Hence in what follows the process $\omega \to \pi^0\gamma$ will be removed from PYTHIA as well, and DIFFVM is used with much larger statistics and better knowledge to describe this particular process. Therefore PYTHIA will be referred to as PYTHIA(mod).

[3] In the following these interactions are also called *inclusive*, as in these processes not the complete final state is reconstructed in contrast to the above signal processes which are also called *exclusive* henceforth.

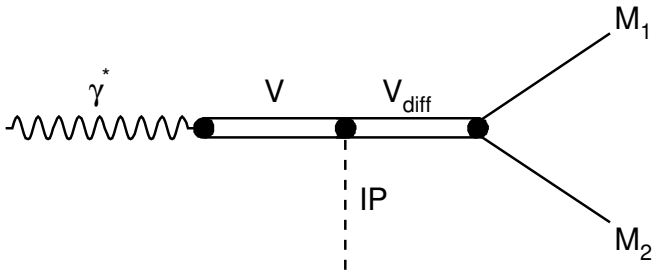

Figure 4.2: Diffractive dissociation as modelled by Pythia: *A photon is turned into a vector meson V according to the VMD and subsequently interacts with the Pomeron. This interaction excites the vector meson into a state called V_{diff}, that decays into two mesons M_1 and M_2 if $m^2_{V_{diff}} < (|\boldsymbol{p}_{V_{diff}}| - \hat{m})^2$.*

$\rho^0_{\rm diff}$				$\omega_{\rm diff}$			
$\pi^0\pi^0$	(6376)	$\rho^0\pi^0$	(2073)	$\pi^0\pi^0$	(576)	$\omega\pi^0$	(409)
$\eta\eta$	(752)	$\omega\eta$	(1004)	$\eta\eta$	(97)	$\rho^0\eta'$	(2)
$\omega\omega$	(174)	$\eta'\pi^0$	(842)	$\omega\omega$	(20)	$\eta\pi^0$	(424)
$\rho^0\rho^0$	(44)	$\omega\rho^0$	(168)	$\rho^0\rho^0$	(4)	$\omega\rho^0$	(22)
$\eta'\eta'$	(1)	$\eta'\eta$	(139)	$\pi^+\pi^-$	(203)	$\eta\rho^0$	(65)
$\eta\pi^0$	(4785)	$\eta'\omega$	(36)	$\eta\eta'$	(12)	$\eta'\pi^0$	(99)

Table 4.1: Events removed from the Pythia sample: *The table shows the summary of all the events removed from the* Pythia *sample due to isospin- and C-parity non-conservation.*

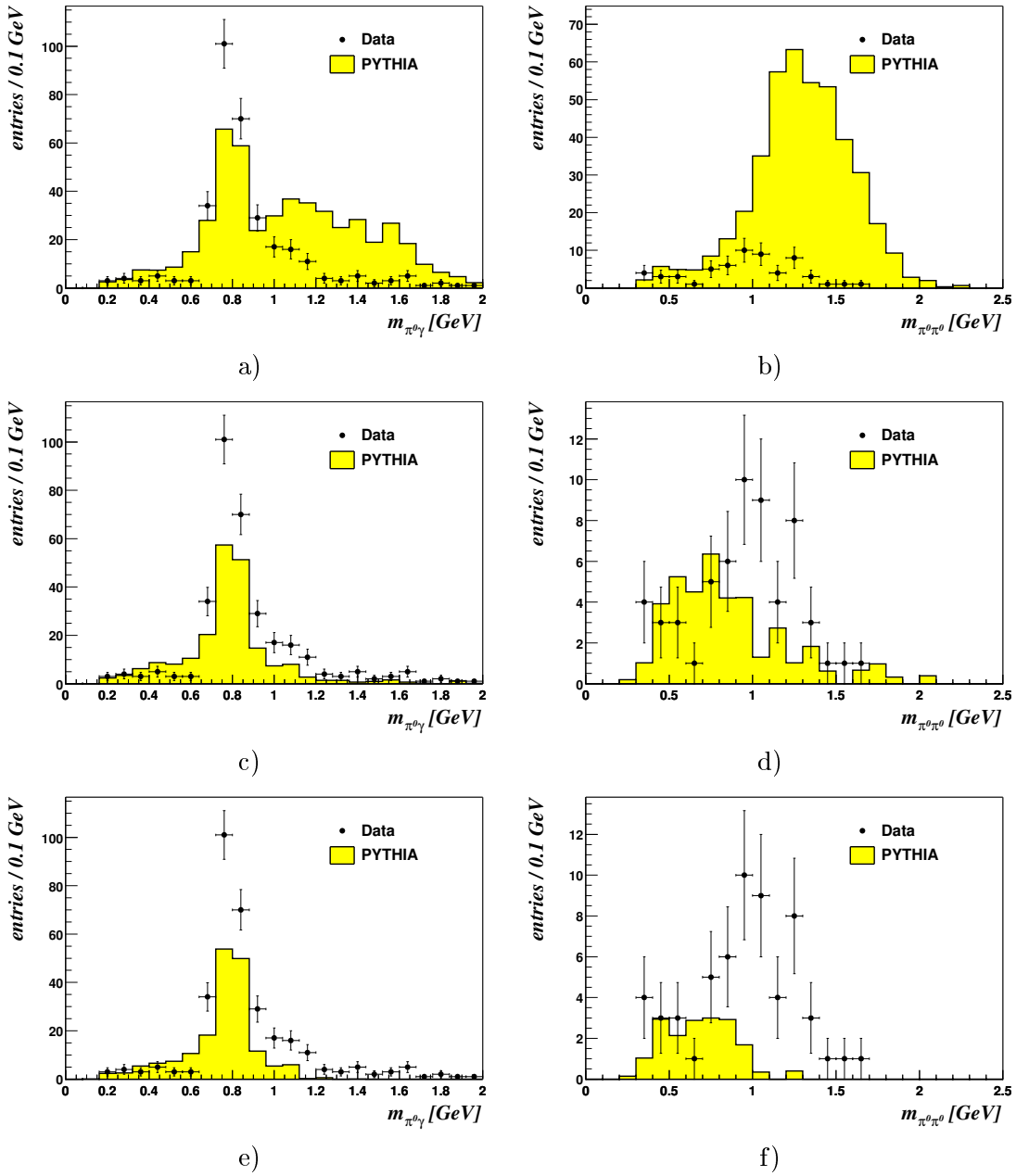

Figure 4.3: Comparison of Pythia with data: *The left column shows the $\pi^0\gamma$ sample and the right column the $\pi^0\pi^0$ sample. The first row, parts a) and b), compare* Pythia *without any modifications to data and for both the $\pi^0\gamma$ and the $\pi^0\pi^0$-sample* Pythia *overestimates the cross section for masses larger than one GeV, especially in part b). The second row – parts c) and d) compares* Pythia *when the isospin or C-parity violating decays of the V_{diff}-state given in table 4.1 are removed. Parts e) and f) show — after the removal of all V_{diff}-states —* Pythia *in comparison with data.*

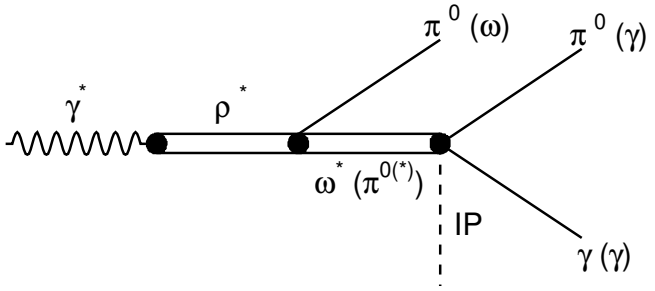

Figure 4.4: Non-resonant photoproduction of $\omega\pi^0$-states: *A (quasi-) real photon turns into a virtual ρ^0 which in the following emits a real π^0 (or ω) and turns into a virtual ω (π^0). Then it interacts with the proton via Pomeron exchange followed by its decay into $\pi^0\gamma$ for example.*

MC		N_{gen}	σ [μb]
DIFFVM	$\omega \to \pi^0\gamma$	79992	1.5
ℙPIUM	$f_2 \to \pi^0\pi^0$	90000	$21 \cdot 10^{-3}$
ℙPIUM	$a_2^0 \to \eta\pi^0$	99995	$9 \times 21 \cdot 10^{-3}$
PYTHIA	$\gamma p \to$ anything	14560000	165
ℙPIUM	$b_1 \to \omega\pi^0 \to 5\gamma$	39996	0.98
ℙPIUM	$b_1 \to \omega\pi^0 \to \pi^+\pi^- 4\gamma$	199980	0.98
PYTHIA	$\gamma p \to \omega\pi^0$(NR)	17000	0.19

Table 4.2: Summary of the Monte Carlo sets: *Given are the number of events generated for the various processes and the cross sections are listed in the last column.*

The photoproduction of the b_1 meson as described in section 4.1.2 is not the only way to produce exclusive $\omega\pi^0$ states, but there is also the non-resonant production as measured in [58, 59]. The non-resonant production can be described by the diagram shown in figure 4.4. This process may be estimated to some extent by the process

$$\rho^0_{\text{diff}} \to \omega\pi^0 \,,$$

modelled by PYTHIA.

4.2 Monte Carlo Sets

Table 4.2 summarises the event numbers generated for the different Monte Carlo sets. All samples were generated with $y \in [0.25, 0.75]$ and $Q^2 < 0.01$ GeV^2, except for PYTHIA which was generated with $y \in [0.3, 0.7]$ and $Q^2 < 0.01$ GeV^2. The corresponding photon flux factors introduced in equation (1.43) for the conversion from a γp into an ep cross section are $\mathcal{F}_{\gamma/e} = 1.83 \cdot 10^{-2}$ for the former and $1.36 \cdot 10^{-2}$ for the latter range in y, respectively. For the Monte Carlo sets be directly comparable to data the corresponding distributions are scaled by factors $\mathcal{C}_i = \mathcal{L}_{\text{data}}/\mathcal{L}_i$, where $\mathcal{L}_i$ is the luminosity for Monte Carlo i calculated using the numbers in table 4.2.

4.3 Detector Simulation and Event-Reconstruction

The response expected from the detector is simulated by a separate programme called H1SIM [60] based on the programme GEANT [61]. The events generated are fed into the simulation and the particles are tracked through the detector simulating their interaction with the material followed by the simulation of the read-out electronics.

The simulation also contains the density profile of the colliding bunches, so it also generates a distribution of interaction points. Since the profiles follow simple Gaussian distributions, but the real distributions exhibit a more complex behaviour, the Monte Carlo events are reweighted accordingly, to follow the observed behaviour. Figure 4.5 shows the distribution of interaction points as measured by H1 and it is compared to the Monte Carlo distribution.

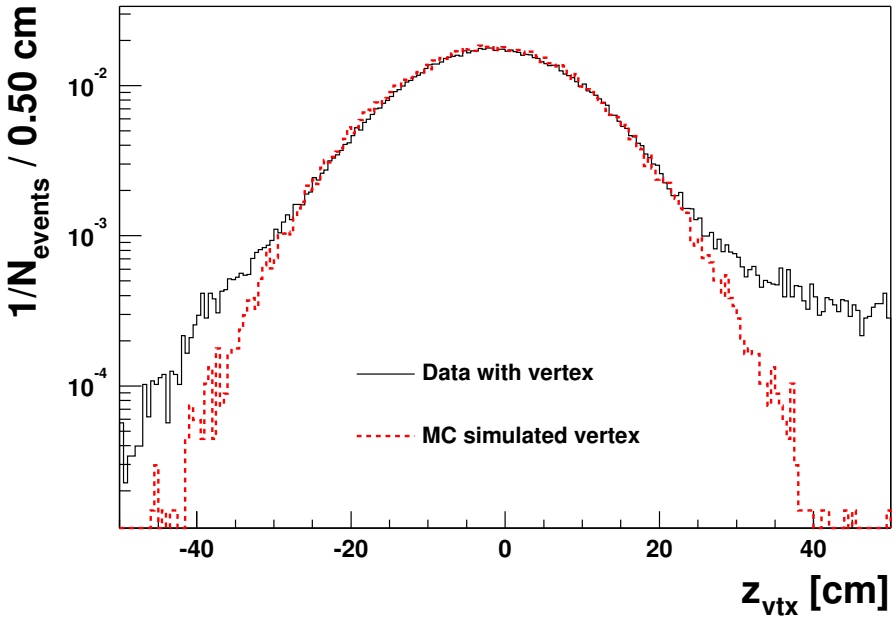

Figure 4.5: Distribution of interaction points in data and simulation: *The full histogram represents the vertex distribution as measured in H1, which is to be compared to the dashed one, which is the corresponding distribution as implemented in the simulation*

The simulated events are reconstructed using H1REC [62], the same programme that is used to reconstruct the events in real data-taking. Thus, they are stored in the same format as real data. It is therefore possible to compare physics models implemented in event generators to measured data with detector effects properly taken into account.

Chapter 5

Exclusive ω-Photoproduction at HERA

5.1 Preparation of the ω Sample

In order to select events with only ω-mesons in the final state (aside from the scattered beam particles) further cuts – in addition to those listed in table 3.1 have to be applied.

As the decay $\omega \to \pi^0\gamma$ is to be analysed, it is obvious to restrict the sample to events with only three photons in the final state, where two stem from a neutral pion. First, criteria have be defined to select photon-candidates[1], since there is background from charged particles (mostly pions) in the SpaCal which is not removed by the no-vertex requirement as the angular coverage of the track- and jet-chambers does not extend to angles that near to the beam pipe. In [63] a study on the separation of electrons and charged pions is presented. There, two criteria are given that can be used to separate strongly interacting particles from electromagnetically interacting ones:

- The lateral size of the latter is significantly smaller than for the former. It turned out that the Monte Carlo has problems describing low-energetic pions and produced much more clusters which are contained in a single cell than are found in data. So, events only with finite cluster-radii are accepted.
- The amounts of energy deposited in the electromagnetic and hadronic parts of the SpaCal differ for electrons an pions.

In [48] a correction in dependence of the energy and the distance was developed. By means of this recalibration it is possible to shift the peak of inclusive π^0's to the nominal pion mass of 135 MeV. This correction is applied here as well for the exclusive final states.

In the following any cluster with an energy $E_i > 100$ MeV in the electromagnetic part of the SpaCal fulfilling

$$R_i \in (0,3)\,\mathrm{cm} \quad \text{and} \quad f_i^{(h/e)} = \frac{E_i^{(had)}}{E_i} < 0.01 \tag{5.1}$$

is considered as a photon. Further, in order to avoid shower leakage at the borders of the SpaCal, it is required that the photons be safely contained:

$$d_i \in [8,75]\,\mathrm{cm}\,, \tag{5.2}$$

[1] Since one can never be sure that a given cluster really stems from a photon the term 'photon' is used synonymously for 'photon-candidate'.

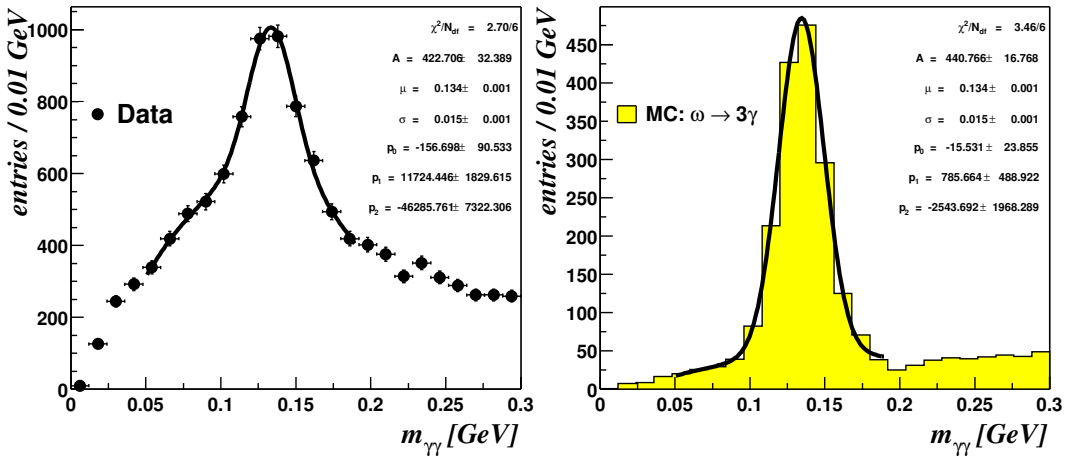

Figure 5.1: Pion-candidates as seen in data and Monte Carlo: *The spectra of photon-photon masses are shown for data in the left and for Monte Carlo (*DIFFVM $\omega \to \pi^0\gamma$*) in right part of the figure. The curves show fits of Gaussians together with third order polynomials.*

where d_i denotes the transverse distance of the photon from the beam pipe. The index i labels the clusters and E_i refers to the energy in the electromagnetic SpaCal while $E_i^{(had)}$ refers to the hadronic part. The cut $E_i > 100$ MeV is applied to reject noise (100 MeV correspond to $\sim 3\sigma_{\text{noise}}$ [64]). I.e. clusters with $E_i < 100$ MeV are ignored in the following, and events with one cluster violating (5.1) or (5.2) are rejected, since they are assumed to be contaminated by charged pions, or have energy leakage.

The basic criterion to select $\omega \to \pi^0\gamma$ events is to require the number of photon-candidates N_γ to equal three:

$$\boxed{N_\gamma = 3}. \tag{5.3}$$

The obvious next requirement to be fulfilled is the event to contain a neutral pion decaying into two photons. This is checked by looking at the invariant masses of the pairs of photons. A pair of photon-candidates is considered as a pion-candidate, if

$$|m_{\gamma\gamma} - m_{\pi^0}| < 40\,\text{MeV}\,, \tag{5.4}$$

where $m_{\pi^0} = 135$ MeV [32] is the nominal mass of the neutral pion. As can be seen in figure 5.1 the threshold of 40 MeV in equation (5.4) corresponds roughly to two times the width one finds for neutral pions. The distributions are fitted with a Gaussian $G(m_{\gamma\gamma})$ and a polynomial of degree three $\mathcal{P}_3(m_{\gamma\gamma})$. The parameters determined by the fit are displayed in the figure and the mean values and widths are shown separately in table 5.1. The mean values fitted to the distributions are (within two standard standard deviations) in accordance with the nominal value.

Demanding exaclyt one pair fulfilling (5.4) would reject events where a second pair accidently falls into this mass window. Therfore it is required that the number of pion-candidates N_{π^0} be equal or greater than 1

$$\boxed{N_{\pi^0} \geq 1}. \tag{5.5}$$

	Data	Monte Carlo
μ [MeV]	133.8±1.0	134.4±0.5
σ [MeV]	15.4±1.4	15.1±0.6
$\chi^2/N_{\rm df}$	2.70/6	3.46/6

Table 5.1: Parameters fitted for pion-candidates: *The table shows the mean value, the width and the χ^2 per degree of freedom found by the fit for data and Monte Carlo (*DIFFVM*)*

As can be seen in the right part of figure 5.2 the cut on Σ can be tightened, since the simulation of $\omega \to \pi^0\gamma$ events shows that this quantity covers the range from 50 GeV to 60 GeV only.

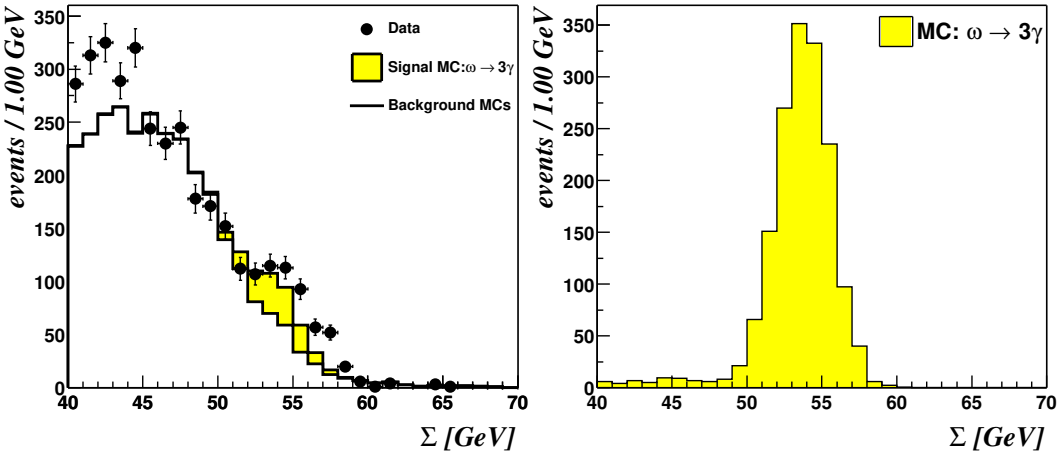

Figure 5.2: The variable Σ for three photons selected: *The left part of the figure shows Σ as it is seen after selecting three photon-candidates. The rise towards small values is due to events where only a fraction of the final state is detected in the SpaCal. The shoulder around 55 GeV (twice the beam energy) stems from exclusive three photon events, being the decay products of the ω as shown by the grey histogram, which is the expectation of $\omega \to \pi^0\gamma$ on top of the assumed background. The right part shows the expected distribution of Σ as given by* DIFFVM.

Therefore it is further required that

$$\boxed{\Sigma_{\pi^0\gamma+\mathrm{eTag}} \in [50, 60]\ \mathrm{GeV}}. \tag{5.6}$$

The last condition imposed, is to select elastic[2] events. To reject events with proton break-up vetoes on components of the H1-detector in the forward direction are applied, namely

$$\boxed{E_{\rm PLUG} < 5\ \mathrm{GeV} \quad , \quad N_\mu < 2 \quad , \quad N_{\rm PRT} = 0}, \tag{5.7}$$

[2]in the sense, that the proton stays intact and the fluctuation $\gamma \to \omega$ is considered as elastic

where E_{PLUG} refers to the energy measured in the PLUG calorimeter, N_μ is the number of hits in layers 1,2 and 3 of the forward muon-system, and N_{PRT} is the number of hits in Proton Remnant Tagger. These latter conditions cannot guarantee that the events are really elastic, but it restricts the mass of the outgoing baryonic system to masses below 1.6 GeV [30]. The remaining background can be estimated to (11 ± 5) % [65].

5.1.1 Beam-Induced Backgrounds

A source of background not covered by the Monte Carlo models are events that do not belong to nominal ep-interactions. A fraction stems from interactions of the beams with the beam-pipe wall or with other "dead" material. These events are rejected already by the trigger due to their bad timing. But there are two further kinds of beam-induced backgrounds: Interactions of the beams with residual gas atoms (beam-gas) and events from so-called satellite bunches.

To obtain the number of events stemming from beam-gas interactions, events from so-called pilot-bunches[3] entering the sample are counted, $N(e-\mathrm{pilot})$. The sample considered here consists of events passing the requirements of table 3.1. From this number the corresponding number of events for all bunches, $N(\mathrm{all})$, is obtained by multiplying the former number with the ratio of the respective currents of the bunches $R = I_e(\mathrm{tot})/I_e(\mathrm{pilot}) = 13.29$[66]. The fraction of beam-gas interactions is thus given by

$$f(e\text{-gas}) = f(e\text{-pilot}) \cdot R = 4.13\,\%,$$

where $f(e\text{-pilot}) = N(e\text{-pilot})/N(\mathrm{all}) = 18/5795 = 0.31$ % is the fraction of events for the selected samples. But this fraction of 4.13 % is not necessarily the fraction that contaminates the sample used to determine the ω-cross section, but only a part of it. To estimate its amount a toy Monte Carlo generator for $\omega \to \pi^0\gamma$ was employed. For the production it was assumed that the events are distributed equally along the z-axis within ± 5 m around the nominal interaction point. The efficiency for these events was estimated requiring that all three photons be detected in the SpaCal and one of the $\gamma\gamma$-pairs be in the pion-window. The geometrical acceptance of these events is found to be 1.8 %. This number does not include the trigger efficiency, and since not all beam-gas interactions lead to exclusive $\pi^0\gamma$ final states this 1.8 % is only an upper limit. Thus the amount of background due to beam gas interactions is estimated to be less than $4.13\,\% \cdot 1.8\,\% = 0.2$ % and can be safely neglected.

The same toy Monte Carlo was used to estimate the contribution of the satellite-bunches, which belong to nominal proton bunches but are separated by 70 cm from the major bunch due to a mismatch of the position of the proton bunch in the accelerating cavities and the frequency. This leads to two accompanying smaller bunches containing ~ 4 % of the protons each at ± 70 cm, respectively. The bunches at -70 cm have an acceptance of 0.2 % only, but those at $+70$ cm are accepted in 5.9 % of the cases, i.e. have more than twice the acceptance of events occurring at the nominal interaction point. But this background can also be neglected, since only ~ 1 % of the interactions from satellite bunches are indeed $\gamma p \to \omega p$ reactions.

[3] Electron pilot bunches are bunches that have an empty appendant proton bunch, and vice versa.

5.2 Comparison of Monte Carlo with data

In figure 5.3 the properties of the photon-candidates are shown for both data (dots) and the Monte Carlos; again the expectation for $\omega \to \pi^0\gamma$ is shown in grey on top of the background assumption of PYTHIA(mod) + $(b_1 \to 5\gamma)$ + $(b_1 \to \pi^+\pi^-4\gamma)$. These distributions and all the others shown in the following are obtained after the application of the cuts (5.3), (5.5), (5.6) and (5.7). The photons are sorted in energy from top to bottom as can be seen in the leftmost column: $E_1 > E_2 > E_3$. The middle column shows the distribution of their transverse distances and the right column shows the radii for these photon-candidates. In general, a good agreement of data and Monte Carlo can be observed.

In figure 5.4 the distances $d_{\gamma\gamma}$ between two photons are shown. The peak at $d_{\gamma\gamma} \sim 8$ cm stems from decaying pions. These photons are nearby each other because of the low pion mass: Labelling these photons as I and II, respectively, the invariant mass can be calculated by $m^2_{I,II} = 2E_IE_{II}(1-\cos\alpha_{I,II})$, where the angle between the three-momenta is denoted by $\alpha_{I,II}$. The kinematics of the event and the geometry of the SpaCal restricts this angle to a visible range of $\alpha_{I,II} \in (0.04, 0.48)$ rad $\hat{=} (2.29, 27.5)^\circ$ and hence together with the distance of the SpaCal from the interaction point results in the distances observed in the right part of figure 5.5 for the Monte Carlo $\omega \to \pi^0\gamma$, where the distribution of photon-photon distances is shown for $m_{\gamma\gamma} < 185$ MeV and $m_{\gamma\gamma} > 185$ MeV, respectively.

Figure 5.6 shows a collection of distributions together with the respective expectations from Monte Carlo, where the signal process $\omega \to \pi^0\gamma$ is plotted in grey on top of the background. The distributions shown are: the mass of the pion-photon system a), the photon-photon mass-spectrum b), the energy c), Σ d), the transverse momentum e), the momentum transfer at the proton vertex $|t|$ f) and the decay-angular distributions $\cos\vartheta^*$ g) and $|\varphi^*|$ h). Also here, a general good agreement can be observed, with the exceptions of the energy distribution c) where the data exhibit a slight shift of ca. one GeV towards higher energies than predicted by Monte Carlo. And the spectrum of the cosine of the decay angle in the hadronic centre of mass frame is more sharply peaked at zero as the Monte Carlo, which may be due to a wrong assignment of the analyser used to calculate $\cos\vartheta^*$.

In figure 5.7 $\pi^0\gamma$-mass distributions are shown with the four Monte Carlos (DIFFVM: $\omega \to \pi^0\gamma$, PYTHIA(mod), and DIPIUM $b_1 \to \omega\pi^0 \to (\pi^0\gamma)\pi^0 \to 5\gamma$ as well as $b_1 \to (\pi^+\pi^-\pi^0)\pi^0 \to \pi^+\pi^-4\gamma$. As can be seen the largest background stems from PYTHIA(mod) (68 events) and the b_1 contributes significantly only via its purely photonic decay mode (18 events), while the decay mode containing charged pions hardly contributes at all (8 events). The above numbers in brackets are to be contrasted with a 134 events expected for the signal process $\omega \to \pi^0\gamma$. The main contributions of PYTHIA(mod) are ρ^0's (46 %), ω's via the three pion decay (22 %), ρ^0_{diff}'s (19 %), ϕ's (6 %), ω_{diff}'s (4 %) and ϕ_{diff}'s (1 %).

5.3 Acceptances

The geometrical acceptance (not yet including the trigger efficiency) is determined by means of the signal Monte Carlo and it is defined as the number of accepted events per generated events N, and is found to be

$$\alpha_{\text{geom}} = 10.9\,\% \pm 0.1\,\%\,, \tag{5.8}$$

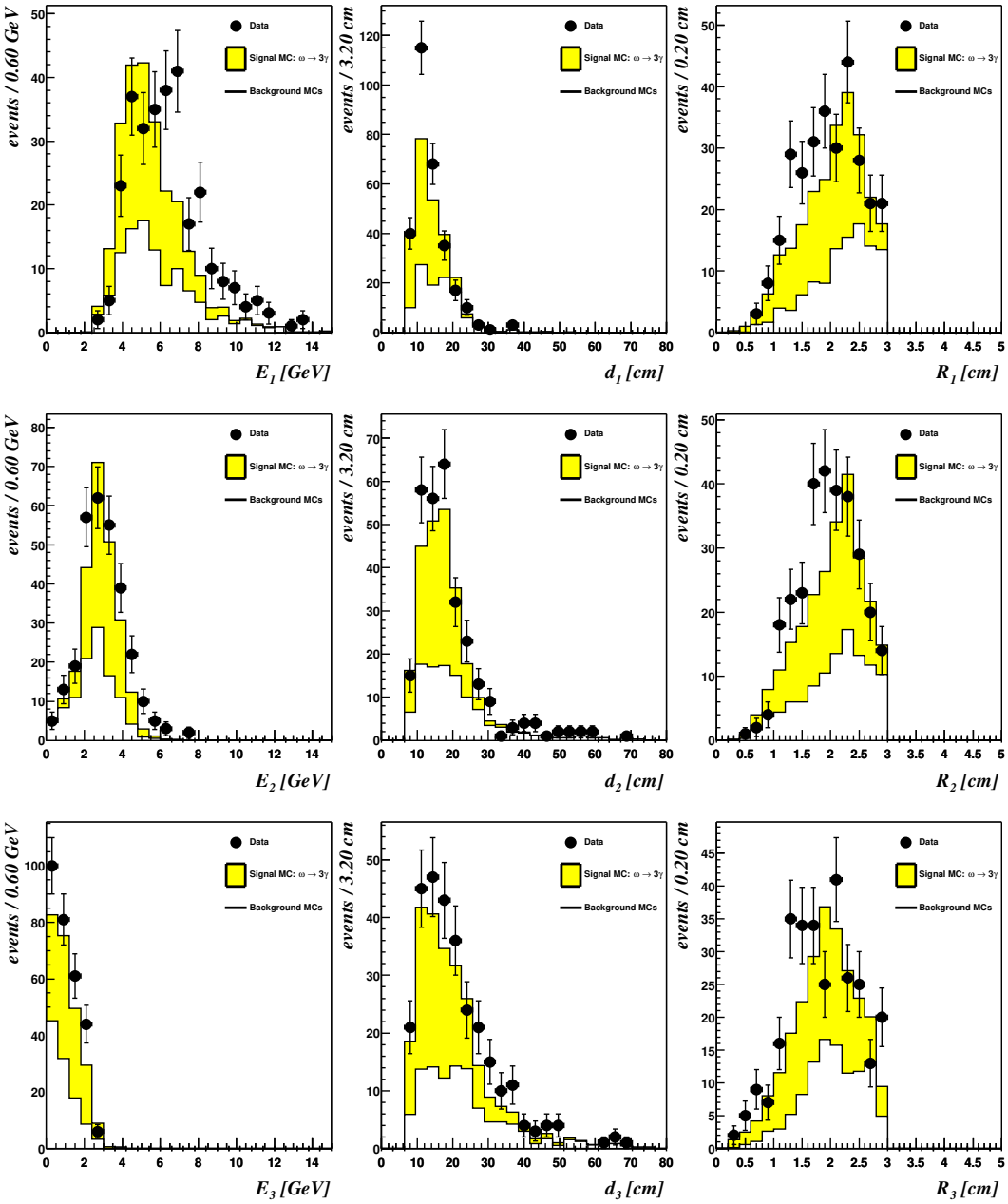

Figure 5.3: Properties of the photons of the decay $\omega \to \pi^0\gamma$: *The energies (left column), transverse distances (middle column) and cluster radii (right column) are shown for the three photons of $\omega \to \pi^0\gamma$. The photons are sorted according to their energies from top to bottom.*

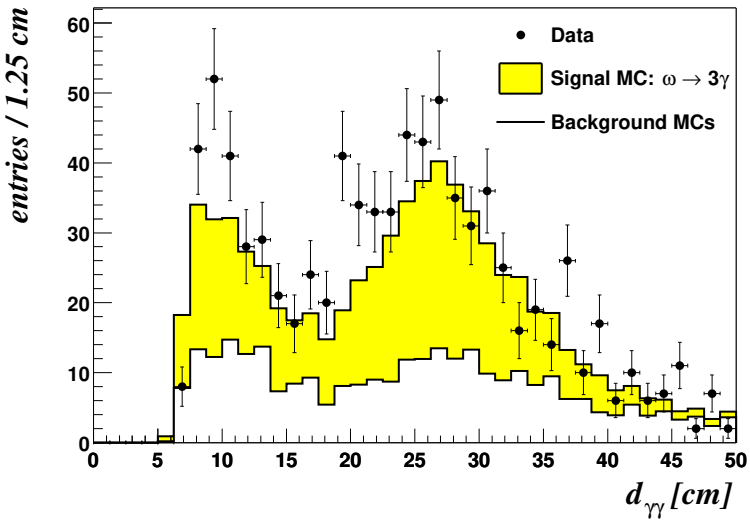

Figure 5.4: Photon-photon distances $d_{\gamma\gamma}$: *The distances between two photons for all three combinations in the SpaCal are shown.*

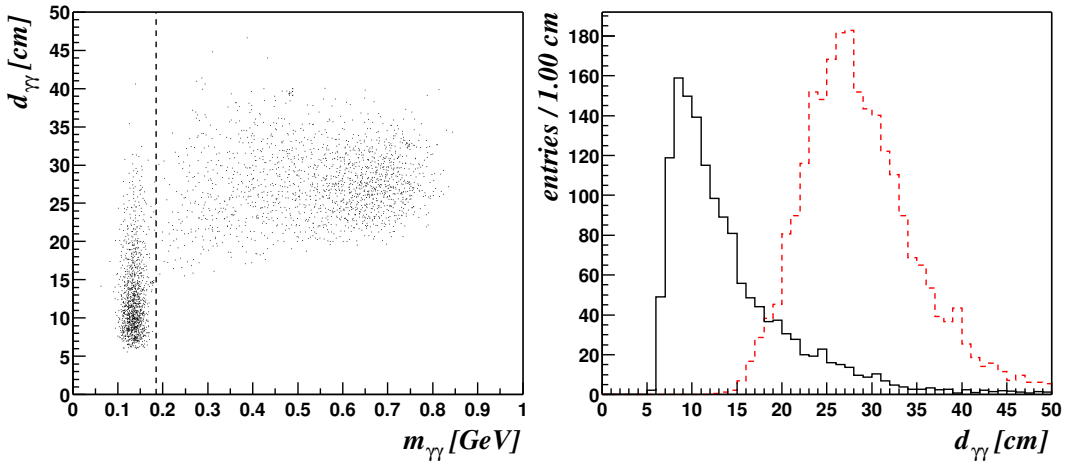

Figure 5.5: Photon-photon masses versus photon-photon distances: *The left part shows the scatter plot of $m_{\gamma\gamma}$ versus $d_{\gamma\gamma}$. One can easily separate the pions from the other combinations. The projection on the $d_{\gamma\gamma}$-axis for $m_{\gamma\gamma} < 185$ MeV as indicated by the dashed line, yields the distribution on the right, which peaks at $d_{\gamma\gamma} = 8.5$ cm. The corresponding distribution for $m_{\gamma\gamma} > 185$ MeV is shown as dashed line and peaks at $d_{\gamma\gamma} = 27$ cm.*

where the error is calculated as $\Delta\alpha = \sqrt{\alpha N(1-\alpha)}/N$. Including the trigger efficiencies reduces the acceptance to[4]

$$\alpha = 2.2\,\% \pm 0.1\,\%. \tag{5.9}$$

[4]The error does not change, since the actual numbers do not change, as the reduction of α is obtained by including the weights.

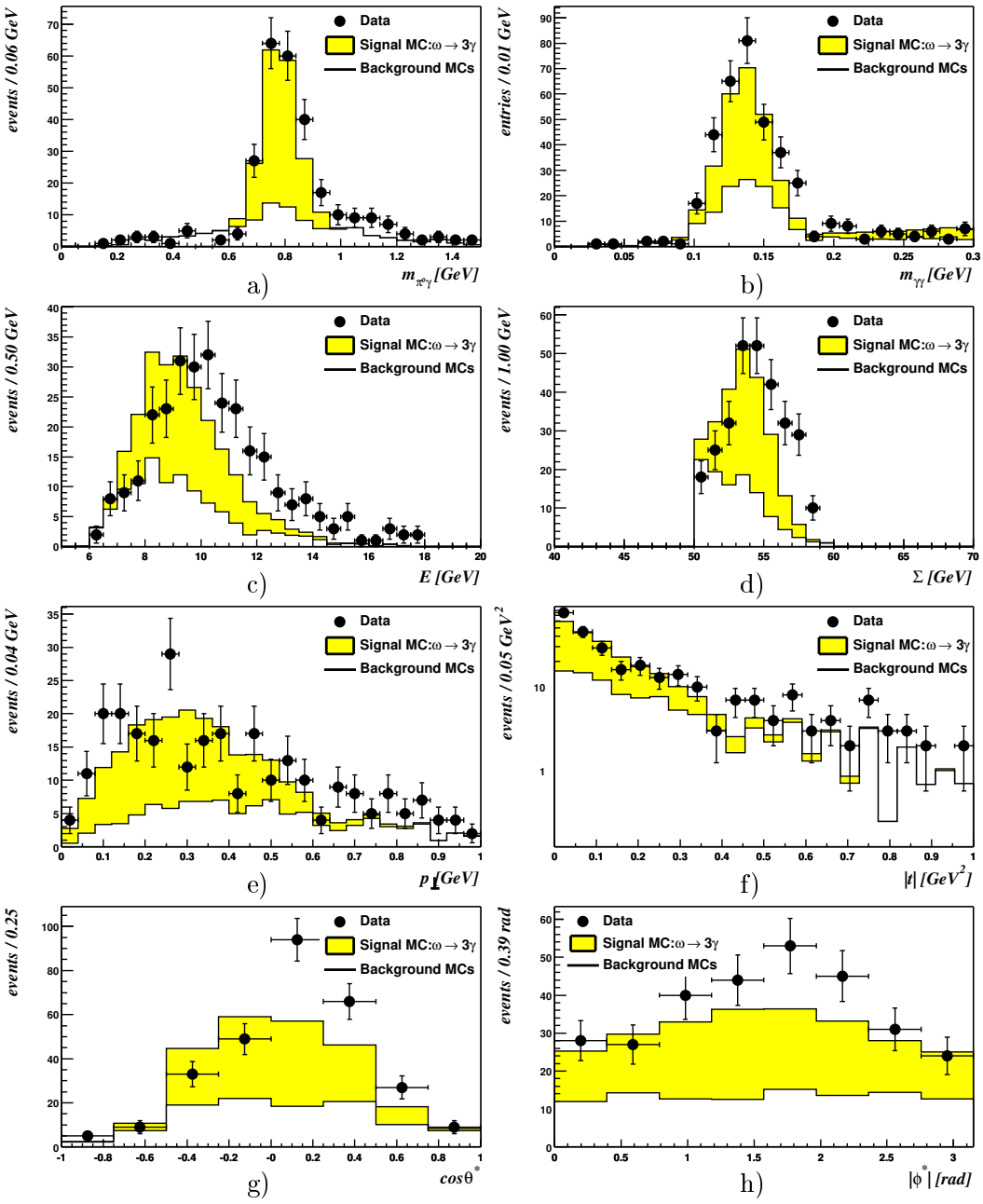

Figure 5.6: Properties of the $\pi^0\gamma$-system: *Distributions characterising the $\pi^0\gamma$-system are shown for data and compared to Monte Carlo-simulations. The distributions show the resulting events after application of the cuts (5.3), (5.5), (5.6) and (5.7)*

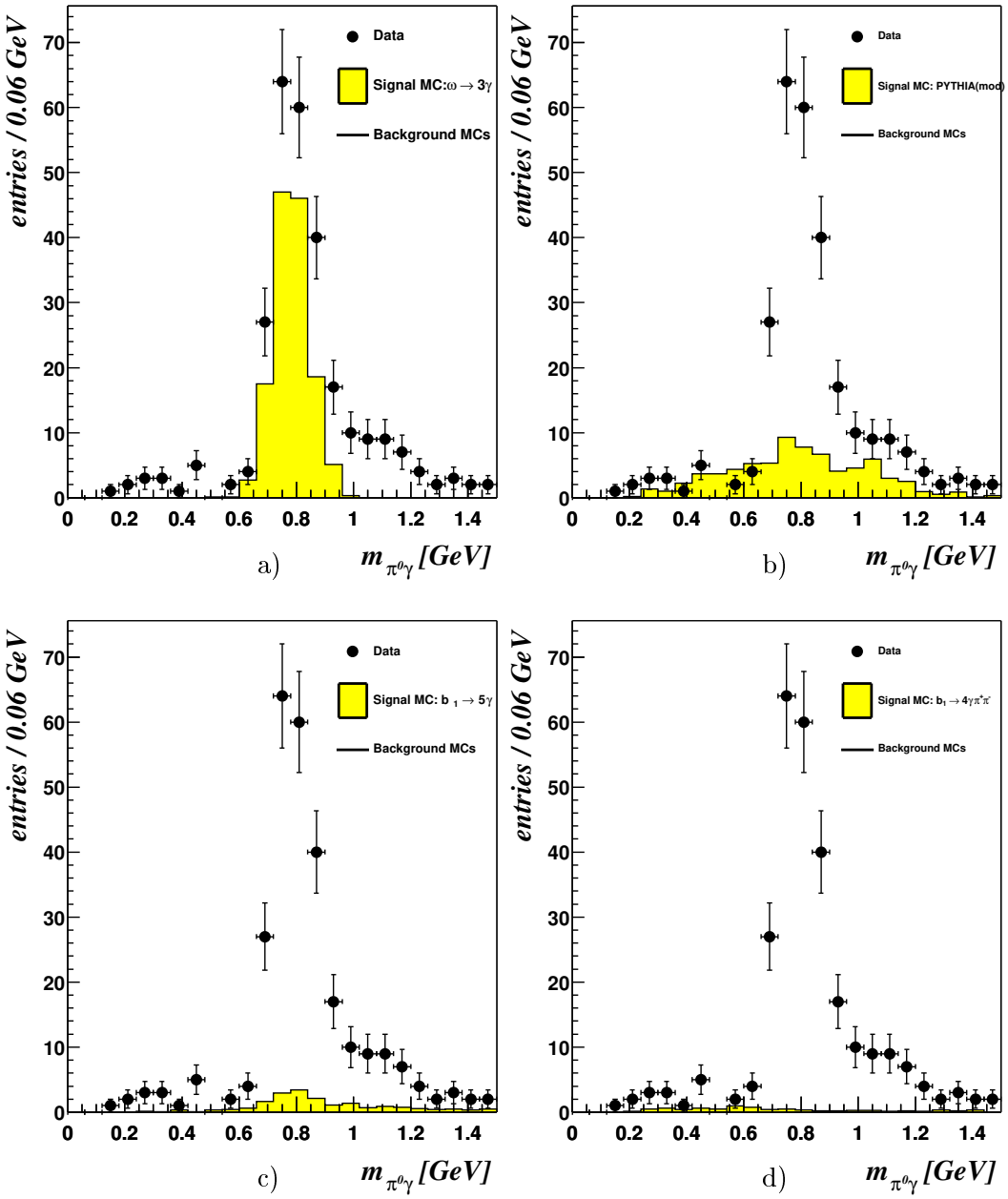

Figure 5.7: Contributions of the Monte Carlos: *The Monte Carlos contributing to the $\pi^0\gamma$ sample are shown separately together with data. Part a) shows the signal process $\omega \to \pi^0\gamma$, part b) shows the dominant background as predicted by* PYTHIA*(mod). The bottom two panels c) and d) show the b_1 decaying purely into photons $b_1 \to \omega\pi^0 \to (\pi^0\gamma)\pi^0 \to 5\gamma$ and $b_1 \to \omega\pi^0 \to (\pi^+\pi^-\pi^0)\pi^0 \to \pi^+\pi^- 4\gamma$.*

Figures 5.16 and 5.17 show the acceptance of the ω for the decay into $\pi^0\gamma$ as a function of various variables: The left-hand panels show the distributions as the respective quantities were generated (upper most solid line), including the effect of the trigger-simulation (dashed) and the result after application of the cuts (bottom most line). The right panels

show the acceptances, i.e. the ratio of the number of events accepted after cuts over the number of events generated: $\alpha(x) = f_{\mathrm{acc}}(x)/f_{\mathrm{gen}}(x)$ where $f_{\mathrm{gen}}(x)$ is the distribution as it was generated and $f_{\mathrm{acc}}(x)$ the corresponding one, but for the events that are accepted by the cuts. Figure 5.16 shows the acceptance as a function of the mass in a)+b), as a function of the energy in c)+d), as a function of the polar angle in e)+f) and as function of the azimuthal angle in g)+h). Figure 5.17 shows the acceptance as a function of the more process dependant variables $|t|$ in a)+b), $\cos\vartheta^*$ in c)+d) and $|\varphi^*|$ in e)+f).

The acceptance exhibits only a weak dependence on the mass of the ω, namely it increases slightly with increasing $m_{\pi^0\gamma}$, since higher masses may produce higher relative transverse momenta increasing the acceptance.

In contrast to the above, the dependences on the energy E and the polar angle ϑ are much stronger. The reason for this behaviour is due to the kinematics of the decay: higher energetic mesons decay more strongly collimated, i.e. the decay products themselves have smaller transverse momenta. But the smaller the transverse momenta are, the nearer to the beam pipe they are and the less is the chance to detect and/or accept the photons.

For the azimuthal angle φ the acceptance is flat as expected.

Also for the $|t|$-distribution the acceptance rises for larger $|t|$ because the transverse momentum of the ω adds to the transverse momentum of the decay products which results effectively in larger transverse distances such that probability for the trigger to accept an event rises.

The behaviour of $\alpha(\cos\vartheta^*)$ and $\alpha(|\phi^*|)$ mainly reflects the interplay of geometrical acceptance and decay kinematics: A decay with $|\cos\vartheta^*|$ near unity means that the analyser has only little transverse momentum and travels nearly along the z-axis of this particular reference frame. Since the production occurs predominantly at small transverse momenta the Lorentz-transformation from the laboratory frame into the meson rest-frame, where $\cos\vartheta^*$ is measured, merely reduces to a boost along the z-axis leaving the transverse components essentially unaffected. Thus, if a decay occurs with $|\cos\vartheta^*| \approx 1$ this means that also $|\cos\vartheta| \approx 1$. But the H1-detector has no acceptance for $|\cos\vartheta|$ near unity, since there is the beam-pipe. The acceptance for $|\varphi^*|$ is not flat, as naively anticipated. This can be explained, remembering that the angle φ^* measures the angle between the planes stretched by the incoming proton and meson (in the hadronic centre of mass) and the plane given by the products of the decay of the meson (see figure 1.17). If the two planes are more or less parallel i.e. $|\varphi^*| \lesssim 0.75$ rad or $|\varphi^*| \gtrsim 2.5$ rad the decay plane intersects the inner ring of the SpaCal and then it might happen that one of the decay products escapes through this inner ring reducing the acceptance for this angular range.

5.4 Resolutions

Figures 5.18, 5.19 and 5.20 show the correlations between the generated and reconstructed quantities on the left and their respective relative resolutions $\Delta x/x_{\mathrm{gen}} = (x_{\mathrm{gen}} - x_{\mathrm{rec}})/x_{\mathrm{gen}}$ on the right. The resolutions shown are for the mass, the energy and Σ in figure 5.18, the polar and azimuthal angle in figure 5.19 and the more process-dependant quantities $|t|$, $\cos\vartheta^*$ and $|\varphi^*|$ in figure 5.20. Table 5.2 summarises the relative and absolute resolutions of the above quantities. In order to improve the resolution of the mass, a mass constrained fit to the pion-candidates was attempted. This fit varies the components of the pion- four momentum within the range of their resolutions till the mass fits the nominal pion mass of 135 MeV. The fit is taken from the analyses package of the ARGUS-collaboration [67]. The procedure failed in the sense that the width of the reconstructed ω did not shrink,

x	$\Delta x/x_{\text{gen}}$ [%]	Δx
m	7.5	58.9 MeV
E	3.0	0.3 GeV
Σ	3.0	1.7 GeV
ϑ	0.1	3.4 mrad
φ	18.7	0.17 rad
$\lvert t\rvert$	32.9	0.03 GeV^2
$\cos\vartheta^*$	12.19	0.04
$\lvert\varphi^*\rvert$	11.4	0.14 rad
	relative resolution	absolute

Table 5.2: Summary of the resolutions for the ω: *The table lists the relative and absolute resolutions of the mass, the energy and Σ as shown in figure 5.18, the polar and azimuthal angle shown in figure 5.19 and of $\lvert t\rvert$, $cos\vartheta^*$ and $\lvert\varphi^*\rvert$ shown in figure 5.20*

although the pion-candidate was successfully constrained to the pion mass. The reason for this is the ignorance of the true interaction point, which introduces a large uncertainty in the reconstruction of the four momenta. And although the pion-candidate is constrained, the third photon-candidate is not affected and its uncertainty stays as large as before. It was further tried to infer the true interaction point by intersecting the plane stretched by the three-momentum of the fitted pion-candidate and the vector between the pion-clusters and the z-axis. If the fitted pion momentum were the true momentum the point of intersection would be the true interaction point. But the Monte Carlo-distribution of the difference of the generated and inferred interaction point, $\Delta z = z_{\text{gen}} - z_{\text{infer}}$, follows a Gaussian with a width of ~ 11 cm, which reflects the distribution implemented in the simulation (see figure 4.5). Thus, this method is not suited to infer the true interaction point which is needed to improve the resolution of the $\pi^0\gamma$-mass significantly. Hence, in the following the unconstrained pion candidates are used.

5.5 Results

5.5.1 Cross Section

The cross section $\sigma(\gamma p \to \omega p)$ is determined by fits to the $\pi^0\gamma$ mass spectrum as shown in figure 5.8.

Two methods are used to get independent approaches for the background:

(i) A relativistic P-wave Breit-Wigner function is convoluted with the resolution as shown in figure 5.18 with the height as the only free parameter. The background is parameterised by a phase-space like ansatz.

The Breit-Wigner function is given by

$$S(x) = A\frac{x m_\omega \Gamma_\omega(x)}{(x^2 - m_\omega^2)^2 + m_\omega^2\Gamma_\omega^2(x)}\,, \tag{5.10}$$

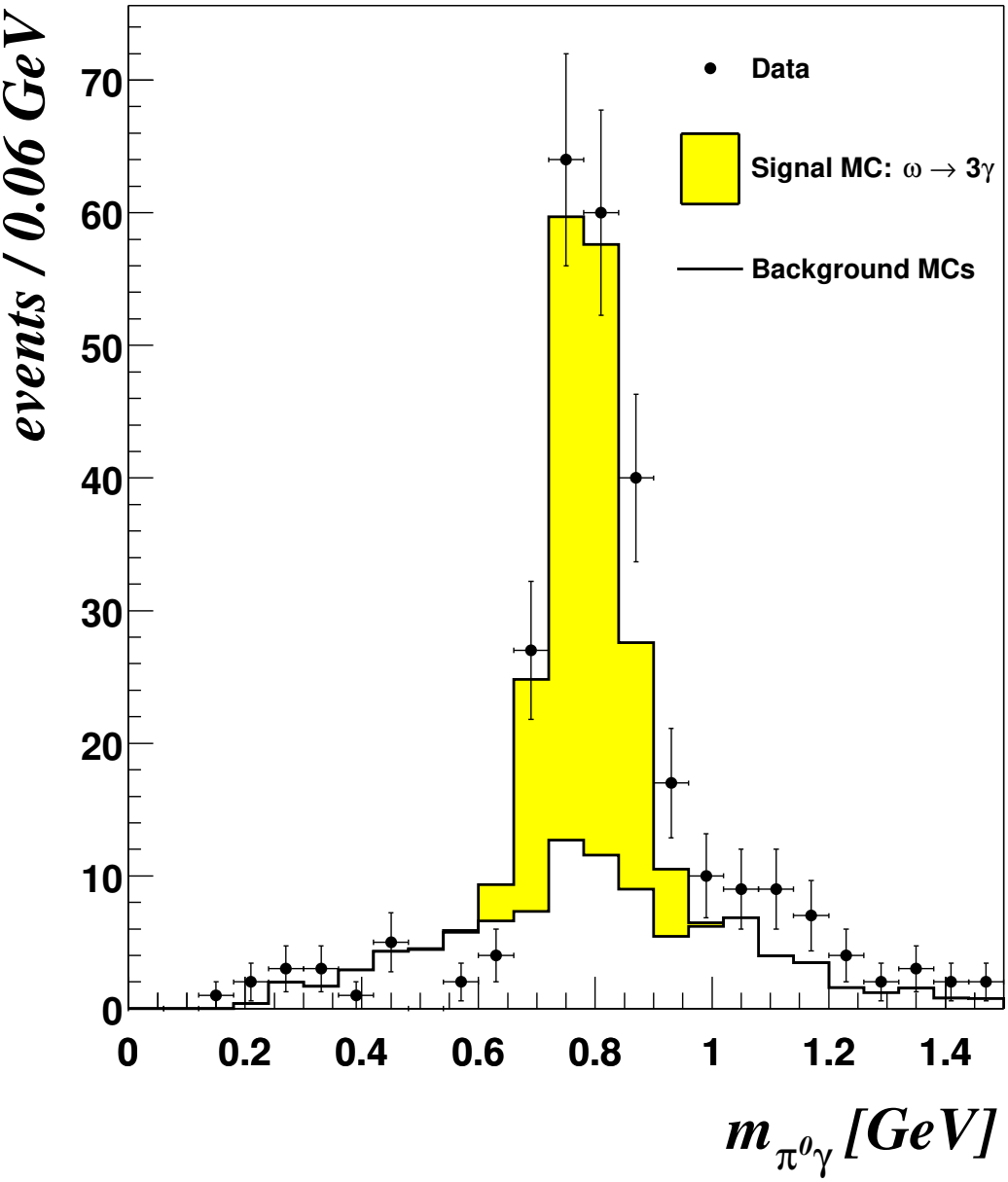

Figure 5.8: Mass distribution of the $\pi^0\gamma$-sample: *The distribution of the invariant mass of a neutral pion and a photon is shown with the cuts (5.3), (5.5), (5.6) and (5.7) applied. The dots represent the data and the histogram shows the Monte Carlo, where the greyly filled component represents the contribution of the signal process $\omega \to \pi^0\gamma \to 3\gamma$ as predicted by* DIFFVM *while the open part corresponds to the background which is assumed to be the sum of* PYTHIA*(mod) and b_1 with its final states 5γ and $\pi^+\pi^-4\gamma$, respectively.*

where x is used for brevity for the pion-photon mass[5] $m_{\pi^0\gamma}$, while $m_\omega = 783$ MeV is the nominal mass taken from [32]. The mass-dependent width $\Gamma_\omega(x)$ is described by

$$\Gamma_\omega(x) = \Gamma_\omega^0 \left(\frac{q^*}{q_0^*}\right)^3 \frac{2}{1+(q^*/q_0^*)^2}\,, \tag{5.11}$$

where $q^* = \frac{1}{2}(x - m_{\pi^0}^2/x)$ and q_0^* are the momenta of the decay products in the rest frame of the ω and for $x = m_\omega$, respectively. The resolution is described by a Gaussian $G(x, m_{\pi^0\gamma}) = \exp[\frac{1}{2}(x - m_{\pi^0\gamma} - \mu_R)^2/\sigma_R^2]$, where $\mu_R = 11.9$ MeV is a shift in the resolution and σ_R is the width. The signal observed is described by

$$\mathcal{S}_{(i)}(m_{\pi^0\gamma}) = \int \mathrm{d}x\, S(x) G(x, m_{\pi^0\gamma}) \equiv (S \otimes G)(m_{\pi^0\gamma})\,. \tag{5.12}$$

To describe the background the function

$$\mathcal{B}_{(i)}(m_{\pi^0\gamma}) = p_0 e^{-p_1 m_{\pi^0\gamma}} \sqrt{m_{\pi^0\gamma} - m_{\pi^0}} \tag{5.13}$$

is used. The fit of the sum of equations (5.12) and (5.13) to the data is shown in the left part of figure 5.9. For the fit m_ω and Γ_ω^0 were fixed to their measured values of 783 MeV and 8.4 MeV, respectively.

From the result of the fit a ρ^0-contribution of $\sigma(\gamma p \to \rho^0 p) \cdot \Gamma(\rho^0 \to \pi^0\gamma)/\mathcal{L} = 13.6\,\mu\mathrm{b} \cdot 6.8 \cdot 10^{-4}/\mathcal{L} = 12$ events ($\sim 10\,\%$) is subtracted, where the former number is taken from [12] and the latter from [32].

(*ii*) A Gaussian function

$$\mathcal{S}_{(ii)}(m_{\pi^0\gamma}) = A \exp\left[\frac{1}{2}\frac{(m_{\pi^0\gamma} - \mu(m_{\pi^0\gamma})^2)}{\sigma(m_{\pi^0\gamma})^2}\right] \tag{5.14}$$

is fitted to the signal and the background is subtracted assuming that it is properly described by the Monte Carlo. This sample, to be subtracted is shown as the open histogram in figure 5.8 and is given by the following sum:

$$\mathcal{B}_{(ii)}(m_{\pi^0\gamma}) = \textsc{Pythia}(\mathrm{mod}) + (b_1 \to 5\gamma) + (b_1 \to \pi^+\pi^- 4\gamma)\,. \tag{5.15}$$

The ρ^0-contribution needs not to be subtracted in this case, since it is included in PYTHIA(mod).

From the fits one can derive the number of events $\mathcal{N}$ as described by the signal assumption which is turned into a cross section by

$$\sigma(\gamma p \to \omega p) = \frac{(1-\kappa)\mathcal{N}}{\alpha\, \Gamma_{\omega\to 3\gamma}\, \mathcal{L}\, \mathcal{F}_{\gamma/e}}\,, \tag{5.16}$$

where $\alpha = 2.2$ % is the total acceptance including the trigger efficiency and geometry, $\Gamma_{\omega\to 3\gamma} = 8.5\,\% \cdot 98.8\,\% = 8.41\,\%$ is the branching ratio for the decay $\omega \to \pi^0\gamma \to 3\gamma$, $\mathcal{L} = 5.41$ pb^{-1} is the integrated luminosity collected for the year 1996 and the subtrigger 50 and $\mathcal{F}_{\gamma/e} = 1.36 \cdot 10^{-2}$ is the flux of photons stemming from the electron as given by the integral over y and Q^2 of equation (1.34). The factor $(1-\kappa)$ accounts for the remaining contamination of 11 % proton-dissociative events.

The parameters found by the fits are listed in table 5.3 together with the χ^2 per degree of freedom. The last row of the table displays the cross sections determined by means of

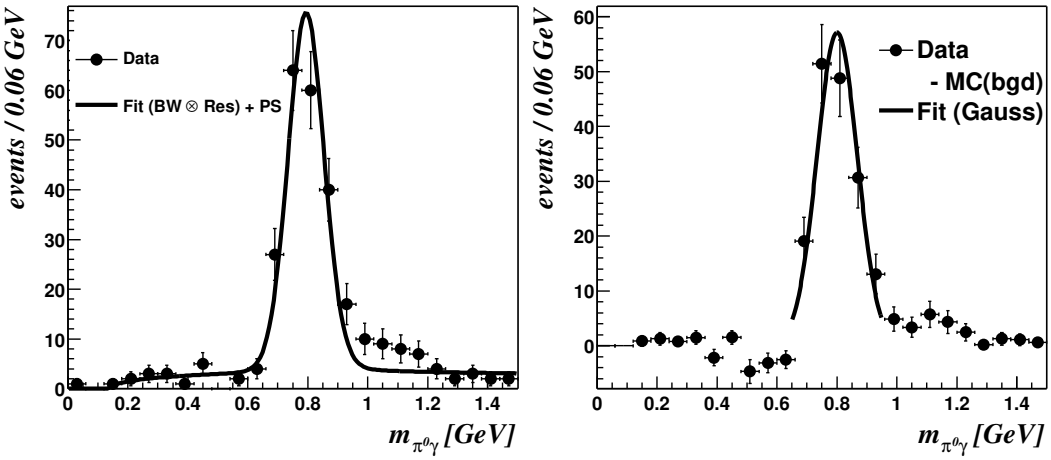

Figure 5.9: Fits to the mass distributions to determine the cross section: *The left part shows a fit of $\mathcal{S}_{(i)} + \mathcal{B}_{(i)}$ to data. The right part shows the mass distribution with $\mathcal{B}_{(ii)}$ subtracted and $\mathcal{S}_{(ii)}$ fitted to the signal in the range of $m_{\pi^0\gamma} \in (0.65, 0.95)$ GeV. The parameters and cross-sections obtained by the fits are given in table 5.3*

	Fit (i)			Fit (ii)	
A	83.9±6.6	μb/GeV	A	57.2±5.7	μb/GeV
p_0	6.6±2.1	μb/GeV	$\mu(m_{\pi^0\gamma})$	800±5	MeV
p_1	0.63±0.3	GeV^{-1}	$\sigma(m_{\pi^0\gamma})$	67.1±4.4	MeV
χ^2/N_{df}	28.2/20		χ^2/N_{df}	14.3/3	
$\sigma(\gamma p \to \omega p)$	1.34±0.11	μb		1.26±0.16	μb

Table 5.3: Parameters found by fits (i) and (ii): *The table lists the parameters and their errors found by the fits together with their respective χ^2 per degree of freedom. The last row gives the cross section obtained by equation (5.16).*

equation (5.16) The average of the two values extracted by the fits (*i*) and (*ii*) is taken as the value for the cross section, since this value is assumed to bear the least uncertainty concerning the background:

$$\sigma(\gamma p \to \omega p) = (1.3 \pm 0.2(\text{stat}))\,\mu\text{b} \tag{5.17}$$

The error was calculated adding the relative errors of the amplitudes of fits (*i*) and (*ii*) and the errors on the Gaussian of fit (*ii*) in quadrature. The difference will be included in the systematic error (section 5.6).

5.5.2 Measurement of the Diffractive Slope

From the differential distribution in $|t|$ one can measure the diffractive slope b by fitting an exponential $\propto e^{-b|t|}$. To do this, first ω-like events are selected by cutting on the invariant mass:

$$\boxed{m_{\pi^0\gamma} \in (0.60, 0.95)\ \text{GeV}}\,. \tag{5.18}$$

The resulting $|t|$-distributions is shown in the left part of figure 5.10.

To extract the true value of b, the $|t|$-distribution as it is measured has to be corrected for acceptance (and to some extent for resolution effects): The correction for a measured distribution $f(x)$ is obtained by means of Monte Carlo events. The true (generated) distribution $\hat{f}_{\text{MC}}(x)$ is divided by the distribution $f_{\text{MC}}(x)$ obtained after applying the cuts and after the detector-simulation:

$$C(x) := \frac{\hat{f}_{\text{MC}}(x)}{f_{\text{MC}}(x)}\,, \tag{5.19}$$

hence, the corrected distribution $\tilde{f}(x)$ is obtained by multiplying the measured one, $f(x)$, by the correction defined in equation (5.19):

$$\tilde{f}(x) = C(x) \cdot f(x)\,. \tag{5.20}$$

Applying this correction — shown in the right part of figure 5.10 — and fitting the result with

$$\tilde{f}(t) = Ae^{-b|t|}\,, \tag{5.21}$$

yields a slope of

$$b = (10.7 \pm 1.1)\,\text{GeV}^{-2}\,, \tag{5.22}$$

with a $\chi^2/N_{\text{df}} = 9.6/15$. The parameter $A = (1655 \pm 273)\ \text{GeV}^{-2}$ is directly proportional to the elastic cross section in the forward direction $\text{d}\sigma(t=0)/\text{d}|t|$, the constant of proportionality is essentially the denominator of equation (5.16) but with the acceptance α replaced by the bin-width δ_t of the t-distribution, since the distribution has already been corrected and only the finite bin-width has to be taken into account:

$$\begin{aligned}\left.\frac{\text{d}\sigma}{\text{d}|t|}\right|_{t=0} \equiv \sigma_0' &= \frac{A}{\delta_t \Gamma_{\omega\to 3\gamma}\mathcal{L}\mathcal{F}_{\gamma/e}} \\ &= (12.2 \pm 2.1(\text{stat}))\,\frac{\mu\text{b}}{\text{GeV}^2}\,.\end{aligned} \tag{5.23}$$

[5] This is the mass that would be measured without any imperfections that lead to finite resolution effects.

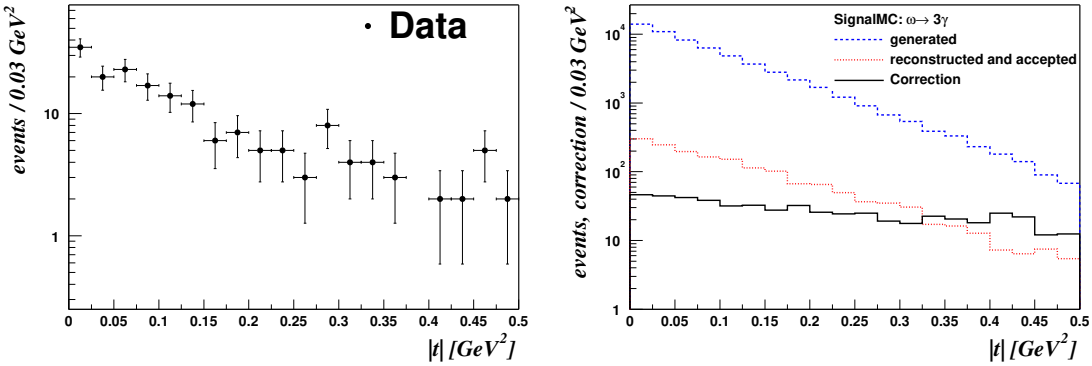

Figure 5.10: The $|t|$-distribution of selected ω-events and its correction: *In the left Part the distribution $\Delta N/\Delta|t|$ for events with $m_{\pi^0\gamma} \in (0.60, 0.95)$ GeV is shown. The right part of the figure shows the correction to be applied as full line. The distribution as it was generated is shown as dashed histogram and the dotted one is the corresponding distribution on detector level after application of the cuts.*

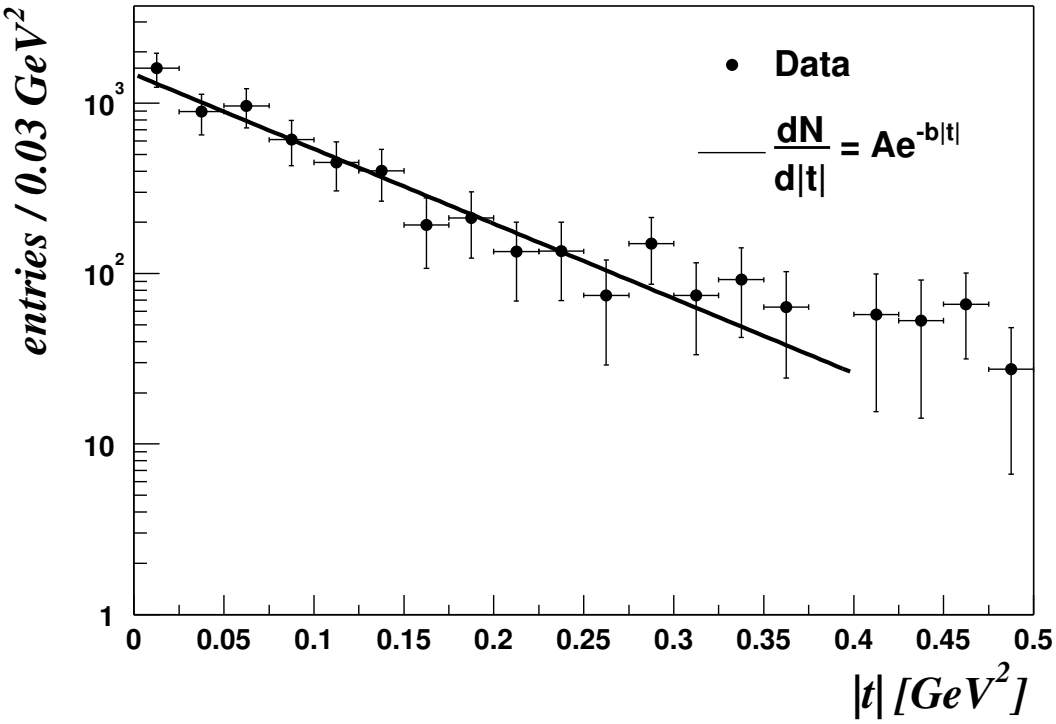

Figure 5.11: A fit to the corrected $|t|$-distribution of selected ω-events: *The acceptance corrected distribution $\Delta N/\Delta|t|$ for events with $m_{\pi^0\gamma} \in (0.60, 0.95)$ GeV is fitted with an exponential.*

Taking the values of σ_0' and b, one can integrate the differential cross section over $|t|$ and obtains another measurement of the elastic cross section $\sigma(\gamma p \to \omega p)$:

$$\begin{aligned} \sigma(\gamma p \to \omega p) &= \sigma_0' \int_0^\infty \mathrm{d}|t| e^{-b|t|} = \frac{\sigma_0'}{b} \\ &= (1.1 \pm 0.2(\mathrm{stat}))\,\mu\mathrm{b}\,. \end{aligned} \tag{5.24}$$

The lower limit of integration was set to zero, while the upper limit was set to infinity, since for the given precision there is no difference, between $e^{-b}0.5$ or $e^{-\infty}$. This value agrees well with the cross section given in equation (5.17).

In figure 5.12 a comparison of the data with a prediction of the SVM is shown. The prediction was calculated for ρ^0-photoproduction and is taken from [68]. The values are scaled by a factor 1/9 which is the only difference the SVM makes between the ω and the ρ^0. Since the calculations are carried out at a photon proton centre of mass energy of 20 GeV a further scale factor of 2 is applied to account for the energy dependence present in Pomeron induced processes. The points are obtained by subtracting the background as given by the Monte Carlo analogous to fit (*ii*) in section 5.5.1 followed by the correction as described above and finally the event numbers per bin are converted into cross sections by a scale factor of $(1-\kappa)/(\Gamma_{\omega\to 3\gamma}\mathcal{L}\mathcal{F}_{\gamma/e})$.

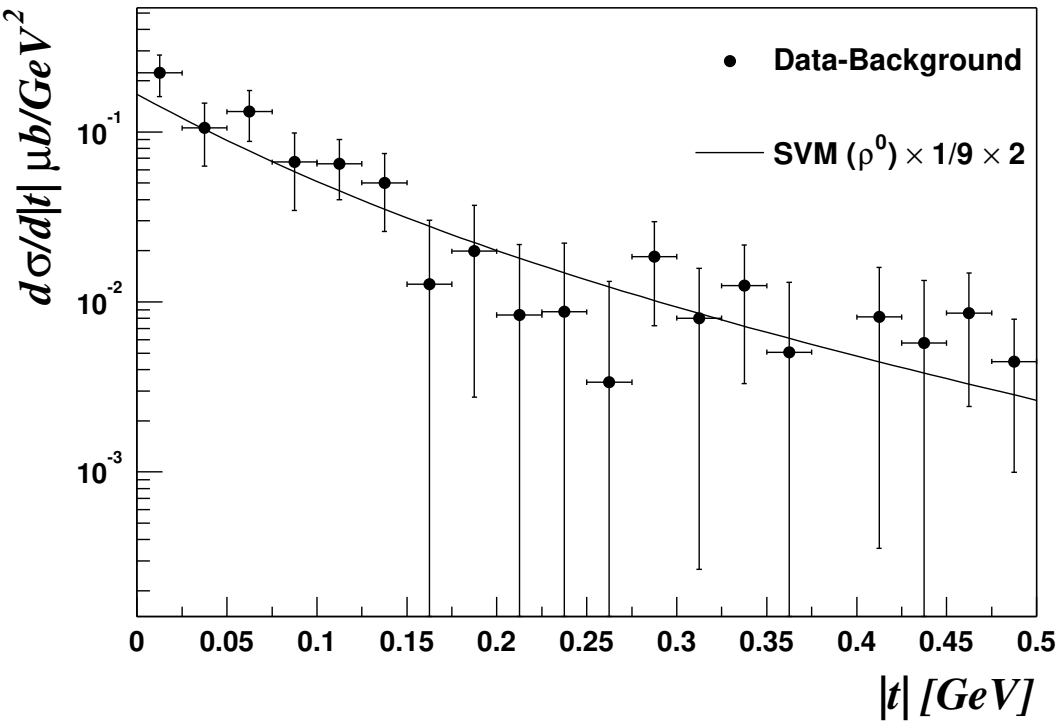

Figure 5.12: Comparison of the corrected $|t|$-distribution with a SVM prediction: *The background reduced and acceptance corrected distribution $\Delta\sigma/\Delta|t|$ for events with $m_{\pi^0\gamma} \in (0.60, 0.95)$ GeV is compared to a prediction of the SVM for ρ^0-photoproduction scaled by a factor 2/9.*

As can be seen by comparing figures 5.12 and 5.11 both the SVM-prediction and a simple

exponential shape describe the measured distribution equally well, although the error bars of the former are larger compared to the latter due to the background subtraction.

5.5.3 Decay Angular Distributions

In principle there are two distributions that can be analysed, but the correction of $\cos\vartheta^*$ as shown in figure 5.13 a) makes it hardly possible to correct the distribution properly, as the corrections reach $\mathcal{O}(10^3)$ for $|\cos\vartheta^*| \to 1$, and therefore the two bins at $|\cos\vartheta^*| = 1$ are not included in the fit. Fitting the expectations for SCHC $W(\cos\vartheta^*) = A(1+\cos^2\vartheta^*)$

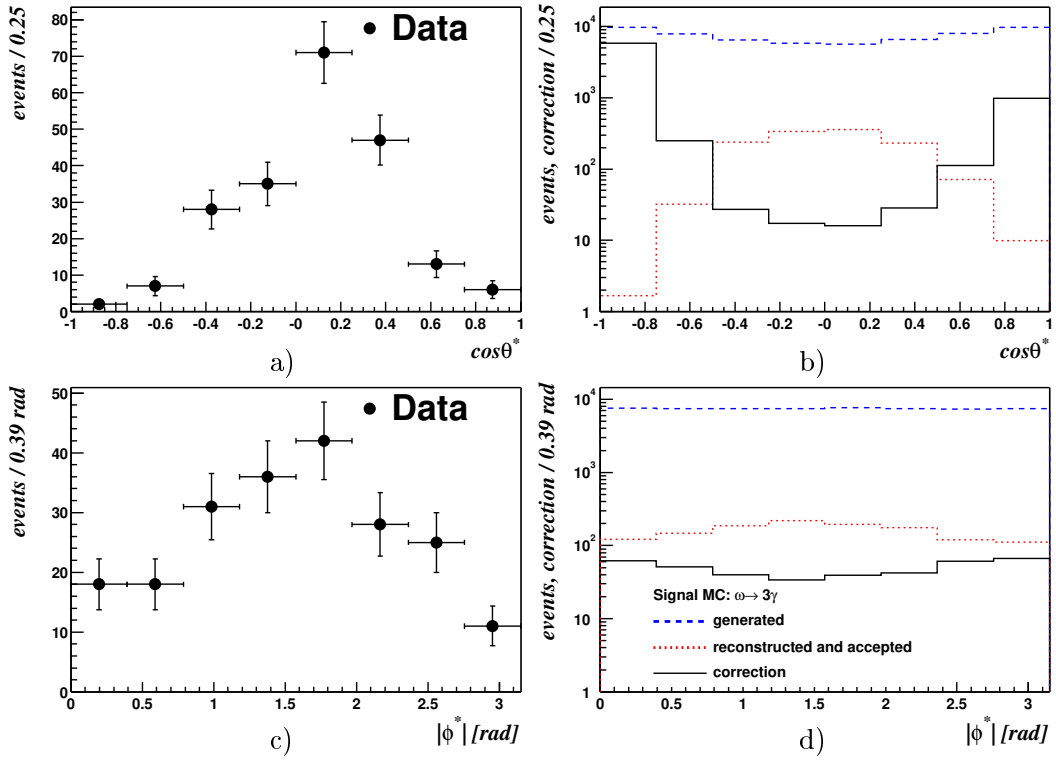

Figure 5.13: Decay angular distributions and their corrections: *Parts a) and c) show the $\cos\vartheta^*$- and the $|\varphi^*|$ distributions before the correction is applied. Parts b) and d) show respectively the Monte Carlo distributions as they were generated (upper dashed histogram) and how they are reconstructed after application of the cuts (lower dashed histogram). The full histogram is the correction to be applied to data.*

and $W(|\varphi^*|) = \text{const}$ to the respective distributions one obtains

$$A = \frac{3}{8\pi}\rho_{+1+1} = 0.10 \pm 0.01 \tag{5.25}$$

$$\text{const} = 0.73 \pm 0.07\,, \tag{5.26}$$

which is well compatible with the expectations from SCHC. The fits are shown in figure 5.14, where the respective distributions are normalised to unity.

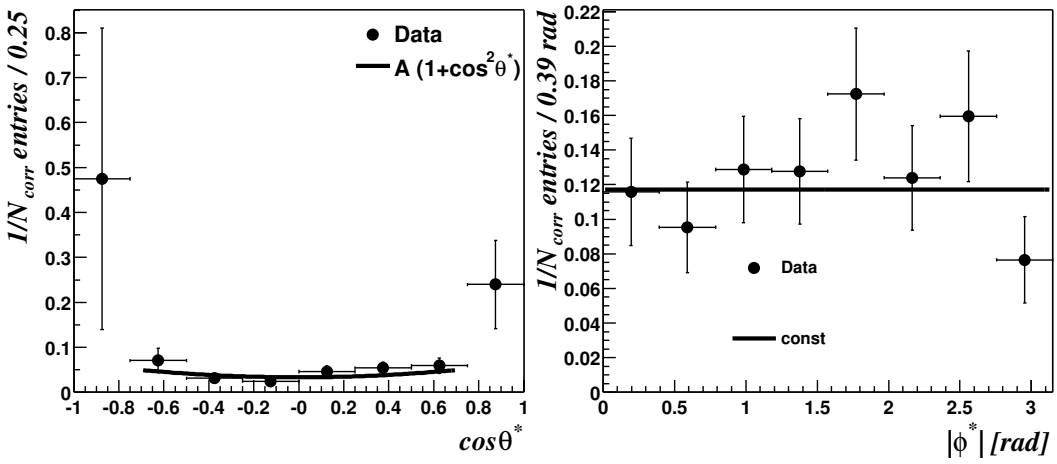

Figure 5.14: Fits to the decay angular distributions: *The left panel shows the to fit to the* $\cos\vartheta^*$ *distribution and the right panel shows the fit to the* $|\varphi^*|$ *distribution*

5.6 Systematics

The systematic uncertainties for the cross section and the slope are estimated by

		$\Delta\sigma_{\text{syst}}$	Δb_{syst}
(1)	Varying the cuts	11 %	15 %
(2)	Varying the energy scales of the SpaCal and the electron tagger within the values quoted for absolute calibration	3 %	9 %
(3)	Reweighting of Monte Carlo distributions (t, $\cos\vartheta^*$)	3 %	2 %
(4)	Changing the binning ($m_{\pi^0\gamma}$, t) and different fits	4 %	9 %
(5)	Using different parameterisation for the trigger simulation	3 %	0.3 %
(6)	Difference of the fits (i) and (ii)	6 %	—
(7)	Uncertainty of luminosity measurement [66]	1.3 %	—
	(1) – (7) added in quadrature	14 %	20 %

For each of the classes (1) – (6) the changes were applied equally to the data sample and the Monte Carlo samples, then the cross section was determined as the average of the results of fits (i) and (ii). The slope was determined by a fit of $Ae^{-b|t|}$ to the corrected $|t|$-distribution. The values determined for each class have a certain spread giving the uncertainty. As a measure for this uncertainty the root mean squared of those values is used.

In (1) the cuts defining the photon- and pion-candidates were varied and the cuts applied to prepare the ω sample were also varied.

For item (2) the energy scale of the SpaCal was varied by ± 4 % and the for the electron tagger a variation of ± 2 % was used.

In (3) the diffractive slope b_{gen} of the ω-Monte Carlo was changed by ± 2 GeV^{-2} and the decay angular distribution was reweighted to follow $1-\cos^2\vartheta^*$ and to be flat, respectively.

For item (4) as additional test for the stability of the fit to the mass distribution, the sum $\mathcal{S}_{(ii)} + \mathcal{B}_{(i)}$ is fitted and the cross section is calculated from the number of ω's as found by this description of the line-shape. Furthermore the binning was varied for all three fits.

The stability of the value extracted for the slope was checked also by varying the binning and also another fit was performed. This fit took into account a contribution of $p_{pd} = 11$ % for proton dissociative events with a slope b_{pd} restricted to the range between two and five GeV^{-2}. In addition, the function was constructed such that the integral yields the actual number of events:

$$\begin{aligned}\frac{\mathrm{d}N}{\mathrm{d}|t|} &= N\left[p_{el}b\frac{e^{-b|t|}}{e^{-b|t|_{\min}} - e^{-b|t|_{\max}}} + p_{pd}b_{pd}\frac{e^{-b_{pd}|t|}}{e^{-b_{pd}|t|_{\max}} - e^{-b_{pd}|t|_{\min}}}\right] \\ &\approx N\left[p_{el}be^{-b|t|} + p_{pd}b_{pd}e^{-b_{pd}|t|}\right] ,\end{aligned}$$

where in the last step $|t|_{\min} = 0$ was inserted and $e^{-b|t|_{\max}} \approx 0$ was assumed. For all the checks the different fits for b yielded the same values for the slope within a few per cent.

In (5) The uncertainty due to the description of the trigger efficiency was studied by a different parameterisation of the acceptance of the electron tagger where a fourth order polynomial was used instead of the tabulated values. For the `IET`-part checks were done using

$$\epsilon(E,d) = \frac{1}{\pi^2}\frac{\sqrt{p_0q_0}}{\left[\arctan\left(\frac{E-p_1}{p_2}\right)+\frac{\pi}{2}\right]\left[\arctan\left(\frac{d-q_1}{q_2}\right)+\frac{\pi}{2}\right]} \quad \text{and}$$

$$\epsilon(E,d) = \frac{1}{4}\frac{\sqrt{p_0q_0}}{\left[\mathrm{erf}\left(\frac{E-p_1}{p_2}\right)+1\right]\left[\mathrm{erf}\left(\frac{d-q_1}{q_2}\right)+1\right]}$$

to describe the efficiency.

The items (6) and (7) affect only the systematic uncertainty of the cross section.

5.7 Summary

In this chapter measurements of elastic ω photoproduction at a mean photon-proton centre of mass energy of 200 GeV have been presented. The quantities measured are the cross section $\sigma(\gamma p \to \omega p)$ and the diffractive slope b:

$$\sigma(\gamma p \to \omega p) = (1.3 \pm 0.2(\mathrm{stat}) \pm 0.2(\mathrm{syst}))\,\mu\mathrm{b} \tag{5.27}$$

$$b = (10.7 \pm 1.1(\mathrm{stat}) \pm 2.0(\mathrm{syst}))\,\mathrm{GeV}^{-2} \tag{5.28}$$

The decay angular distributions have been found to be compatible woth SCHC, though the first and the last bin of the $\cos\vartheta^*$-distribution had to be excluded from the fit to the SCHC prediction, since in these bins the corrections exceeds values of 1000. The third angle ψ^* has not been accessible at all, since the four momentum of the scattered electron is not measured but only the energy.

Comparison with other Measurements

The values found for the cross section and the slope fit well into the picture of Regge theory and its predictions for both of them, as can be seen in figure 5.15 where the above measurements are compared to other measurements at lower energies and the expectation from Regge theory.

The slope measurements in the lower part of the figure can in turn be used to fit the slope of the Pomeron trajectory anew by means of equation (1.65) with $\alpha'_{I\!P}$ as free parameter. For $s_0 = 10$ GeV^2 one obtains a value of

$$\alpha'_{I\!P} = (0.15 \pm 0.08)\,\text{GeV}^{-2} \tag{5.29}$$

with a χ^2 per degree of freedom of $10.16/13 = 0.78$, which is within two standard deviations in accordance to the standard value of 0.25 GeV^{-2}. The corresponding value of b_0 increased as compared to table 1.3 slightly from (6.6 ± 0.1) GeV^2 to (6.9 ± 0.3) GeV^{-2}.

Comparing the cross section obtained in this chapter with measurements of other vector mesons, one can immediately compare with the ρ^0 [12] since this measurement was performed practically at the same photon proton centre of mass energy, and of course with a measurement of the ω at lower W [10].

$$\sigma(\gamma p \to \rho^0 p) = (13.6 \pm 0.8(\text{stat}) \pm 2.4(\text{syst}))\,\mu\text{b} \qquad \langle W \rangle = 187\,\text{GeV} \tag{5.30}$$

$$\sigma(\gamma p \to \omega p) = (1.2 \pm 0.1(\text{stat}) \pm 0.2(\text{syst}))\,\mu\text{b} \qquad \langle W \rangle = 80\,\text{GeV} \tag{5.31}$$

For the ratio of the vector-photon couplings f_V^2 one expects the ratio [45]

$$f_{\rho^0}^{-2} : f_\omega^{-2} : f_\phi^{-2} = 9 : 1 : 2 \tag{5.32}$$

where for this measurement only the first of the above ratios can be calculated, as for the ϕ there exists only one measurement [69] performed by the ZEUS collaboration at lower energies (70 GeV). For the ρ^0 and the ω the ratio of the couplings equals the ratio of the cross sections assuming validity of the additive quark-model (cf. section 1.6.4 and equations (1.77) and (1.78)). For the ϕ things would be more complicated, since in this case $\sigma_{\text{tot}}^{\phi p} \neq \sigma_{\text{tot}}^{\omega p}$, but as there is no measurement of the ϕ-cross section at $W \approx 200$ GeV, there is no need to go into those details.

The ratio of the couplings in photoproduction at HERA at $\langle W \rangle \approx 200$ GeV is experimentally found to be

$$\begin{aligned} f_{\rho^0}^{-2} : f_\omega^{-2} &= \sigma(\gamma p \to \rho^0 p) : \sigma(\gamma p \to \omega p) \\ &= (10.5 \pm 1.72(\text{stat}) \pm 2.45(\text{syst})) : 1\,, \end{aligned} \tag{5.33}$$

what is quite good agreement with equation (5.32).

Comparing the measurement at lower energies ($W \gtrsim 10$ GeV) the rise of the cross section is only marginal and could be as well fitted by a logarithm or a logarithm squared as proposed in other Pomeron parametrisations (cf. appendix A).

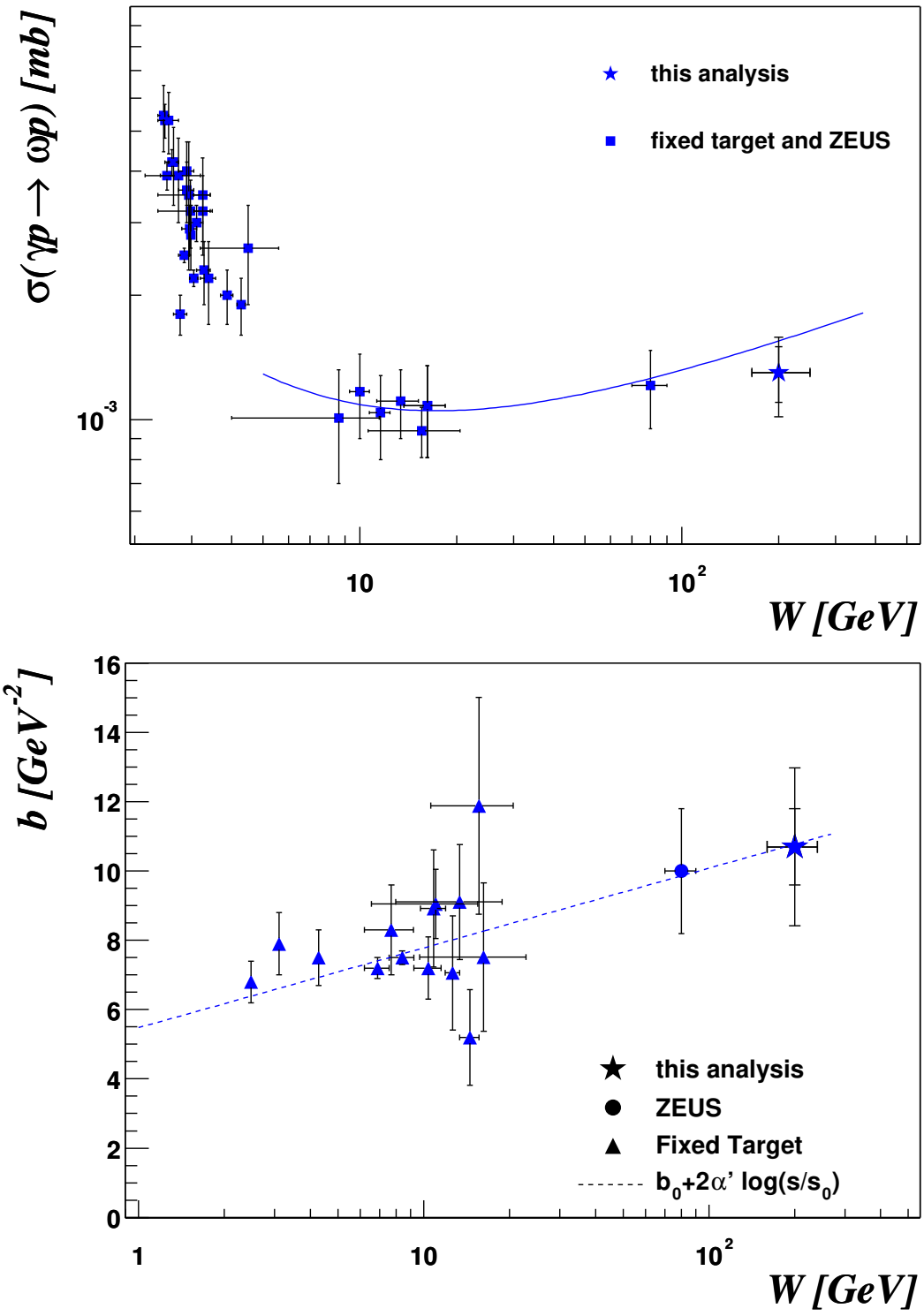

Figure 5.15: Comparison of the $\sigma(\gamma p \to \omega p)$ and b with other measurements: *The upper figure shows the measurement of the elastic ω-photoproduction cross section measured in this analysis at $\langle W \rangle = 200$ GeV together with other measurements at lower energies. The line shows a Regge theory based prediction (see section 1.6.4).*
The lower figure shows the diffractive slope measured in this analysis — again — together with measurements at lower energies and a Regge-based prediction (see section 1.6.1)

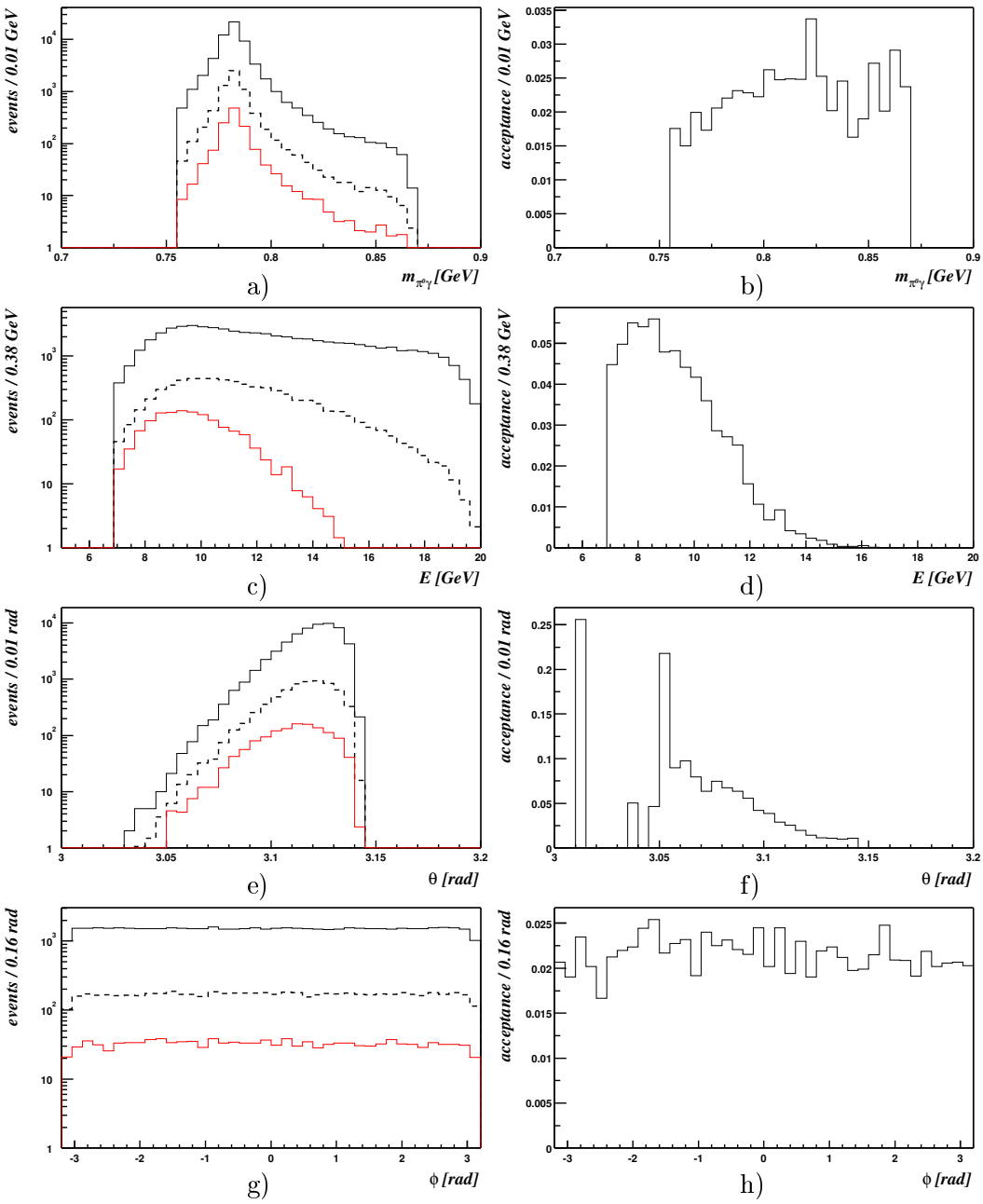

Figure 5.16: Acceptances for the ω (I): *The panels on the left show distributions as they were generated (upper most solid line), how they are affected by the trigger (dashed line) and as they are accepted after application of the cuts (bottom most solid line). The right-hand panels display the respective acceptances, defined as the ratio of the solid lines. The distributions shown are (from top to bottom) the mass, the energy, the polar angle and the azimuthal angle.*

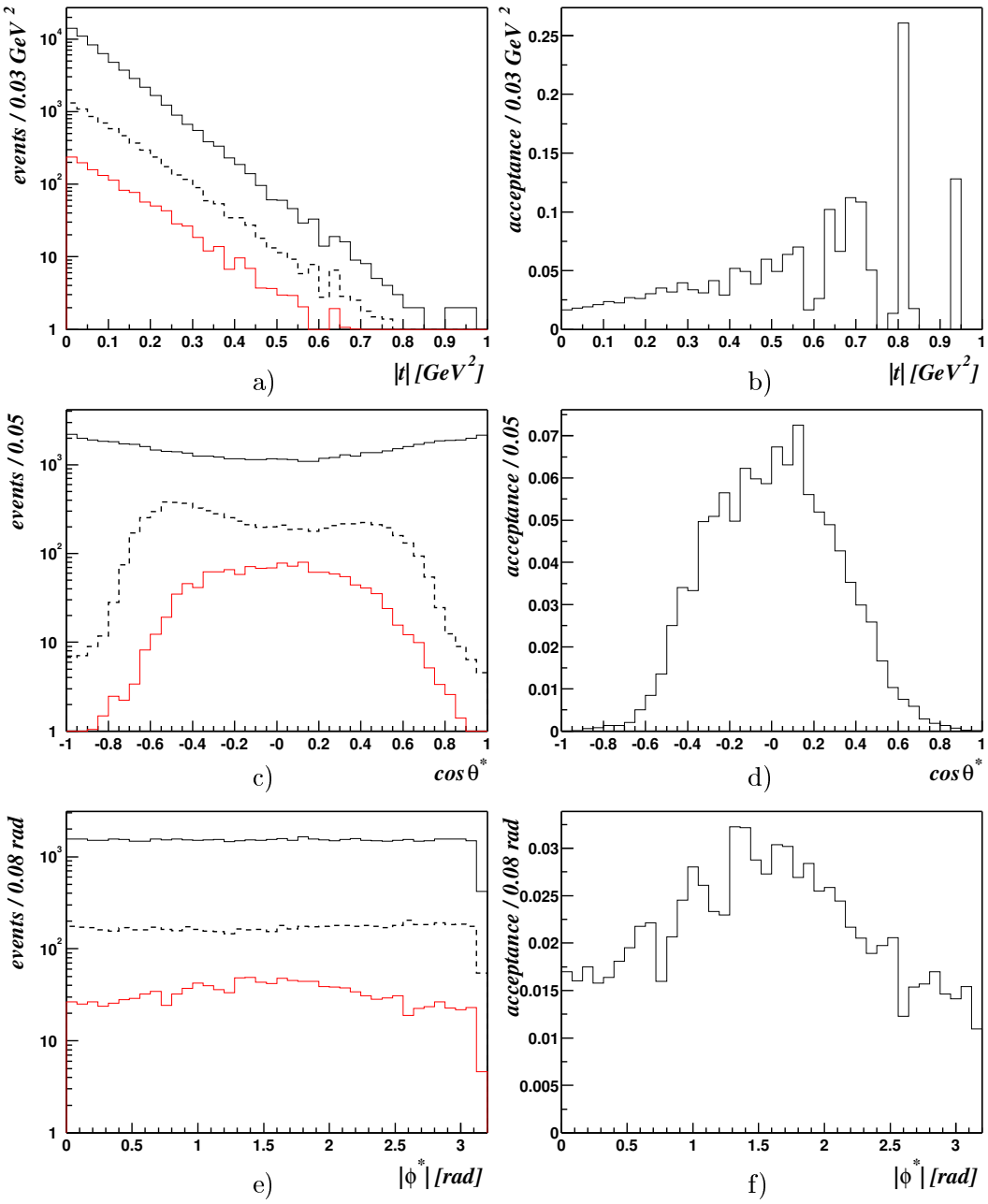

Figure 5.17: Acceptances for the ω (II): *The figure shows the same as in figure 5.16 but for the momentum transfer squared at the proton vertex* $|t|$ *and the decay angular distributions* $\cos\vartheta^*$ *and* $|\varphi^*|$.

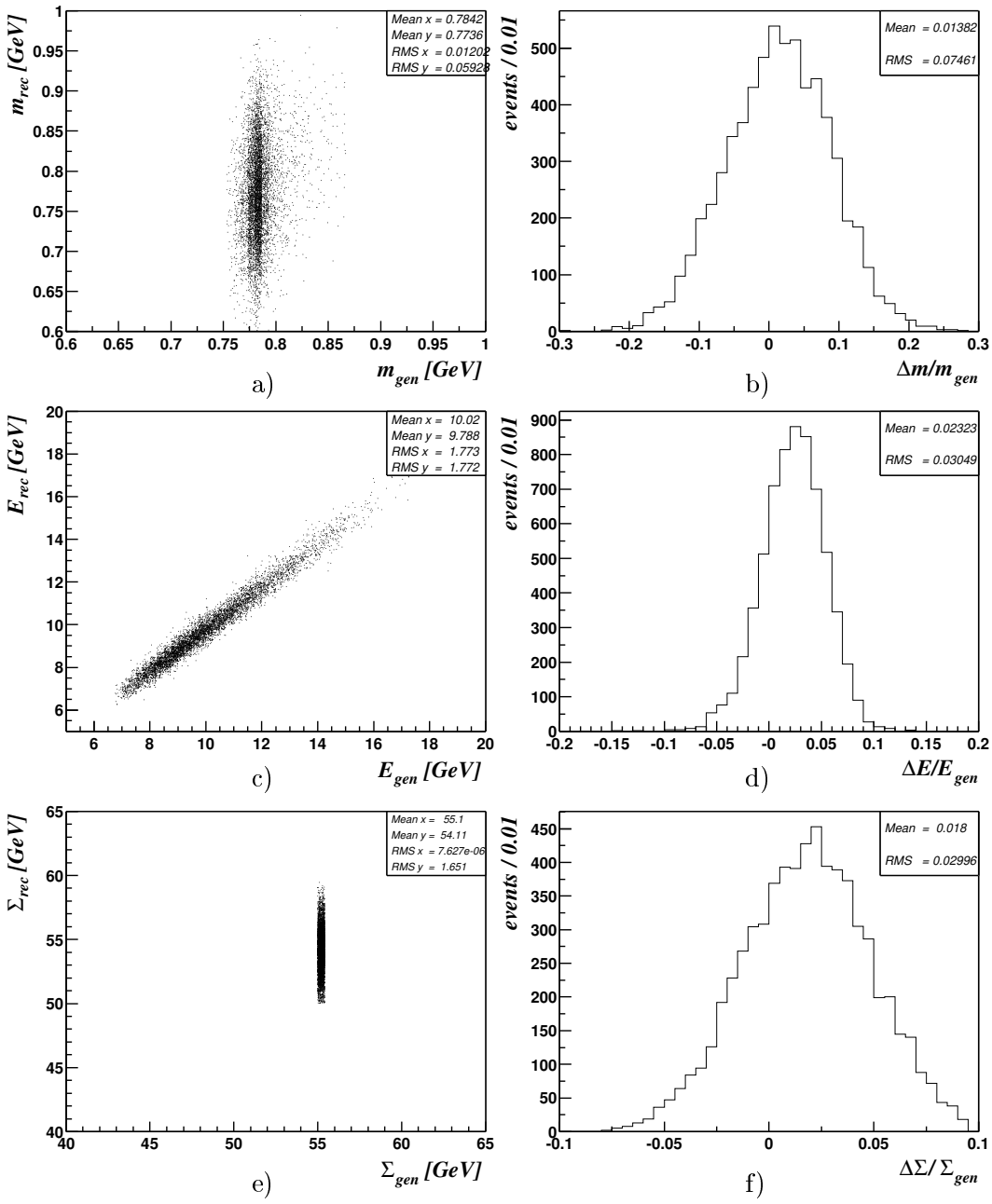

Figure 5.18: Resolutions for the ω (I): *The panels on the left hand side show the correlations of reconstructed quantities with their generated values. The right hand side panels show the relative resolutions. From top to bottom one can see the correlation and relative resolution of the mass $m_{\pi^0\gamma}$ a)+b), the energy E c)+d) and the light-cone minus component Σ e)+f).*

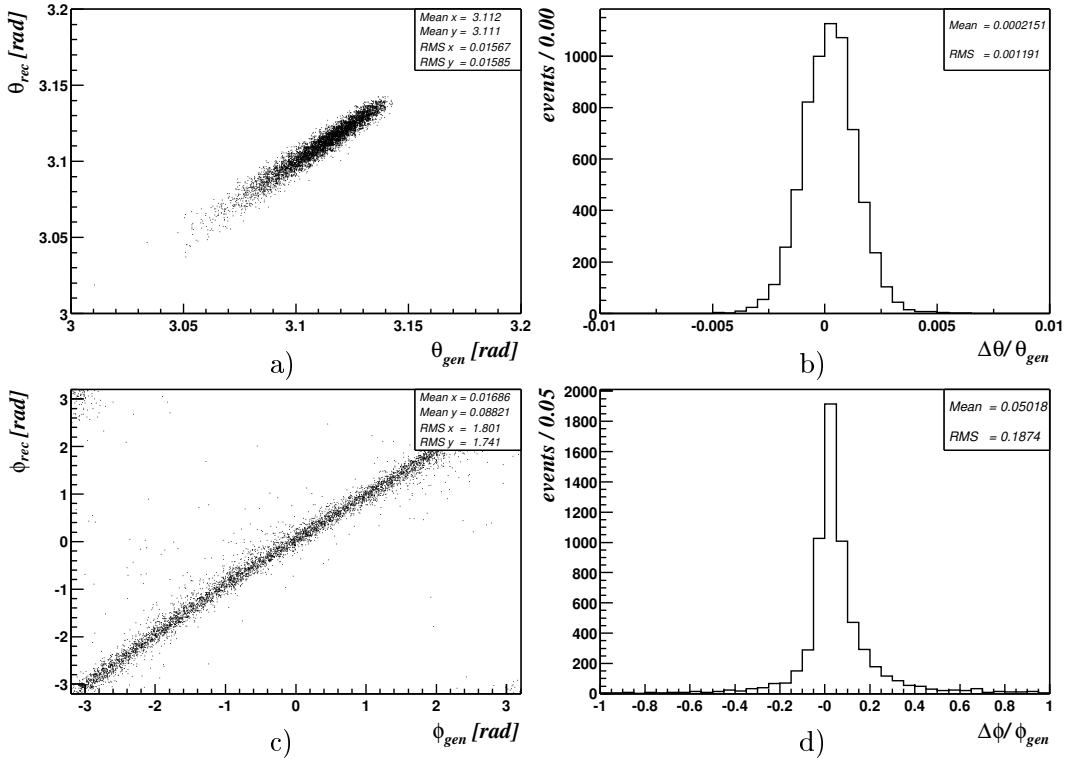

Figure 5.19: Resolutions for the ω (II): *The figure shows the same as in figure 5.18 but for the angles ϑ a) + b) and φ c)+d).*

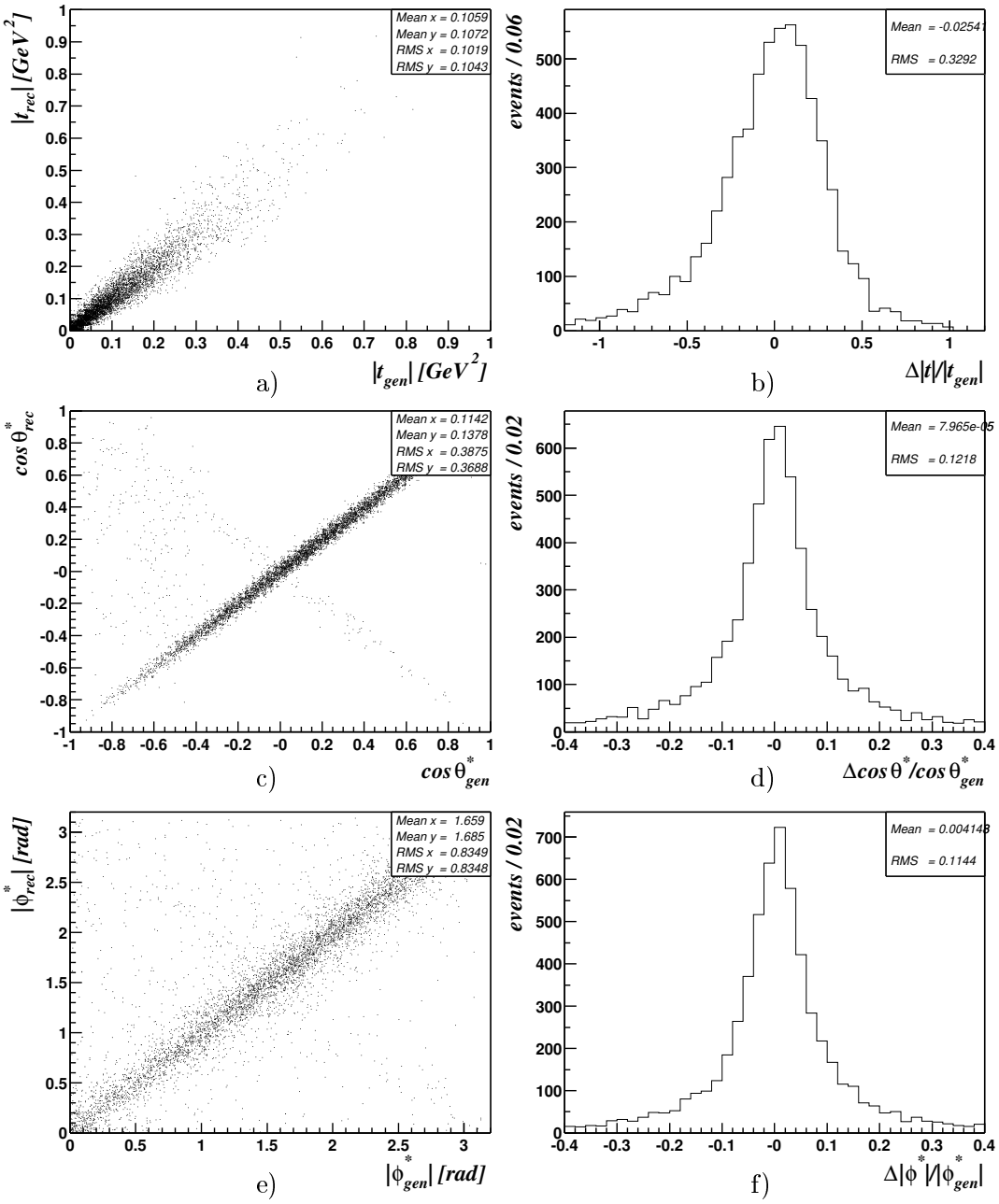

Figure 5.20: Resolutions for the ω (III): *The figure shows the same as in figure 5.18 but for the momentum transfer squared |t| a)+b), the decay-angular distributions* $\cos\vartheta^*$ *c)+d) and* $|\varphi^*|$.

Chapter 6

Exclusive f_2 Photoproduction at HERA

6.1 Preparation of the f_2 Sample

The analysis of the $f_2 \to \pi^0\pi^0 \to 4\gamma$ proceeds along analogous lines as for the ω, especially the selection of photon- and pion-candidates is identical as described in 5.1, so the cuts are just repeated briefly, for details the reader is referred to section 5.1.

$$E_i > 100\,\mathrm{MeV} \tag{6.1}$$

$$R_i \in (0,3)\,\mathrm{cm} \tag{6.2}$$

$$f_i^{(h/e)} < 0.01 \tag{6.3}$$

$$d_i \in [8,75]\,\mathrm{cm} \tag{6.4}$$

As in chapter 5 a cluster is neglected if it fails to pass cut (6.1) and events are rejected if one cluster does not satisfy the criteria (6.2) – (6.4). The correction for low energetic clusters, developed in [48], is applied here as well. The definition of pion-candidates is also the same as in chapter 5, namely

$$|m_{\gamma\gamma} - m_{\pi^0}| < 40\,\mathrm{MeV}\,, \tag{6.5}$$

with $m_{\pi^0} = 135$ MeV [32], which is justified as can be seen in figure 6.1. The values found by fitting the two-photon mass spectra of both data and Monte Carlo are listed in table 6.1.

	Data	Monte Carlo
μ [MeV]	133.8±1.0	133.9±0.2
σ [MeV]	14.7±1.3	15.6±0.2
χ^2/N_{df}	3.81/6	8.19/6

Table 6.1: Parameters fitted for pion-candidates: *The table shows the mean value, the width and the χ^2 per degree of freedom found by the fit for data and Monte Carlo (*0*I*PIUM*).*

The major differences between the ω- and the f_2-sample are the number of photon- and pion-candidates selected:

$$\boxed{N_\gamma = 4} \tag{6.6}$$

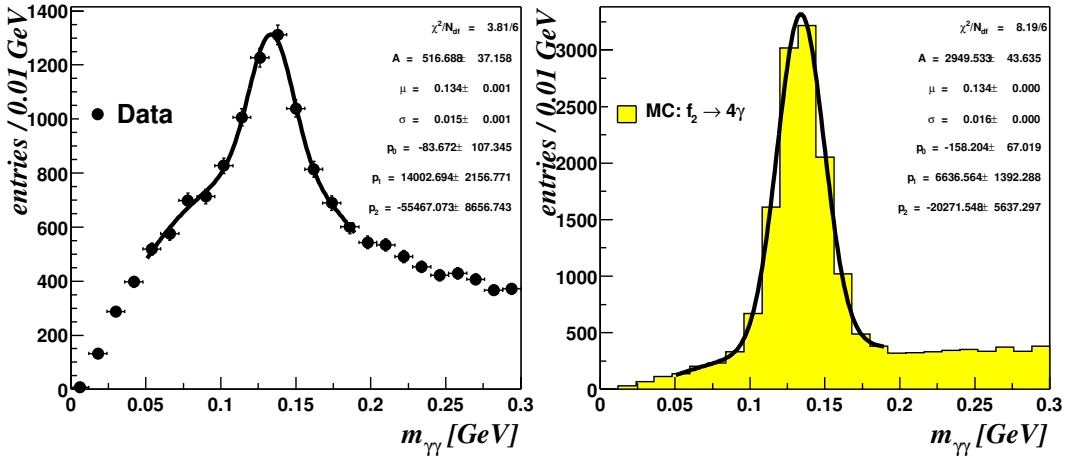

Figure 6.1: Pion-candidates as seen in data and Monte Carlo: *The spectra of photon-photon masses are shown for data in the left and Monte Carlo (*DIPSIUM *$f_2 \to \pi^0\pi^0$) in the right. The curve shows fits of a Gaussian together with third order polynomial.*

and

$$\boxed{N_{\pi^0} \geq 2}. \tag{6.7}$$

In addition to this, the requirement for elastic production is dropped, since the SVM explicitely requires proton excitations into $\{2P\}$ states (see section 1.7.2). And the remaining cut to be applied is

$$\boxed{\Sigma_{\pi^0\pi^0+\mathrm{eTag}} \in [50, 60]\ \mathrm{GeV}}. \tag{6.8}$$

The right part of figure 6.2 shows the Σ-distribution for the four-photon sample and in contrast to the corresponding figure (fig. 5.2) in the three photon final state, here is no shoulder of exclusive events visible, though the expectation as shown in the right part is completely analogous to the ω case.

If the f_2 and the a_2 are produced according to the predictions of the SVM, there have to be neutral pions (and η's) to be visible in the $\gamma\gamma$-mass spectra, especially if one looks at the spectrum of photon pairs (k, l) when the other pair (i, j) is accepted by the pion cut (6.5). If $p_{4\gamma}$ denotes the sum of the four momenta of the four photons and $p_{ij} = p_i + p_j$ the two photon four momentum, the four momentum of the remaining two photons is given by $p_{kl} = p_{4\gamma} - p_{ij}$. This system is said to "recoil against the pair (i, j)" and in particular, if $|m_{ij} - m_{\pi^0}| < 40$ MeV it "recoils against a π^0". Figure 6.3 shows on the left hand side in panels a) and c) all combinations of the $\gamma\gamma$-masses, where in a) the signal Monte Carlo in grey is the f_2 and the a_2^0 is included in the background shown as the open histogram below the signal. In c) the rôles of f_2 and a_2^0 are interchanged. The panels on the right show those combinations when a pair is in the pion window indicated by the dashed lines of the left part. In b) one can see the expectation for the second π^0 of the f_2 decay in grey on top of the background and in d) it is the expectation of the η that is shown in grey. The dashed lines in parts b) and d) correspond to the pion-window (6.7) and to the η-window used in [2].

Cut (6.7) is to be understood in the sense, that an event to be accepted as f_2-candidate, has to have at least two photon pairs where one pair also lies in the region given by the

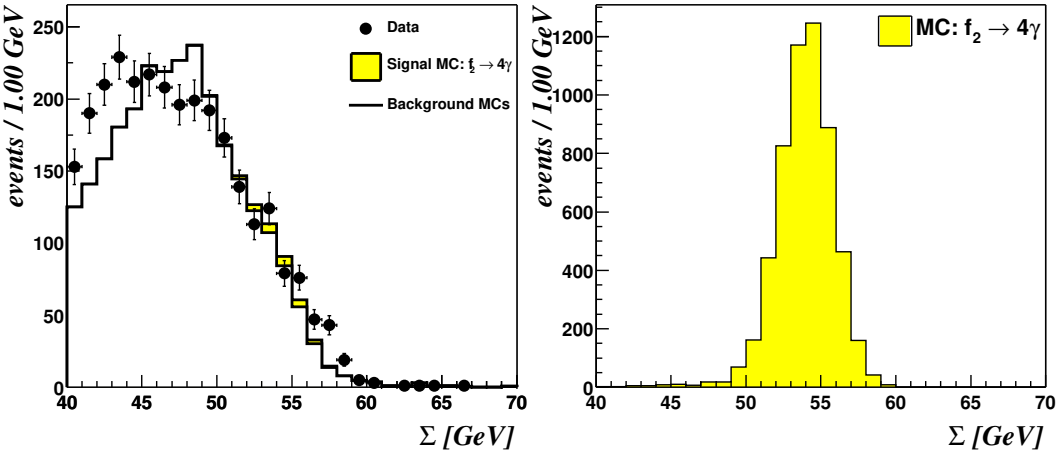

Figure 6.2: The variable Σ for four photons selected: *The right part of the figure shows Σ having selecting four photon-candidates. The rise towards small values is due to events where only a fraction of the final state is detected in the SpaCal. The expectation of $f_2 \to \pi^0\pi^0$ is shown on top of the assumed background. The right part shows the expected distribution of Σ as given by* PYTHIA.

dashed lines in the part b) of figure 6.3.

Already from this figure, especially from part d), one can anticipate that the prediction of the SVM is not likely to be confirmed, as it is obvious that the SVM expectation overshoots the data (shown as the dots).

6.2 Comparison of Monte Carlo with data

Figure 6.4 compares the energies (leftmost column), the distances from the beam-pipe (middle) column and the radii of the clusters of data with the expectation given by the Monte Carlos. As in chapter 5 the photons are sorted such that $E_1 > E_2 > E_3 > E_4$ from the top to the bottom. Here and in the following the cuts (6.6), (6.7) and (6.8) are applied.

The agreement of the Monte Carlo description with the data is quite satisfactory, though the contribution of the f_2 appears not really to be needed and it seems to be possible to describe the spectra shown also be means of the background alone. This becomes also apparent in figure 6.5, where properties of the di-pion system are shown. Also in this figure the distributions are described quite well by the Monte Carlo simulations. Figure 6.6 gives the single processes as they contribute to the mass spectrum. In part a) the signal process $f_2 \to \pi^0\pi^0$ (31 events) is shown in grey and for $m_{\pi^0\pi^0} \gtrsim 1.2$ GeV the f_2 alone describes the data well, but the background contributions shown in b) PYTHIA(mod) (34), c) $b_1 \to \omega\pi^0 \to (\pi^0\gamma)\pi^0 \to 5\gamma$ (15) and d) $b_1 \to \omega\pi^0 \to (\pi^+\pi^-\pi^0)\pi^0 \to \pi^+\pi^-4\gamma$ (17) are expected to be present as well. The $a_2 \to \pi^0\eta \to 4\gamma$ (< 1) shown in e) and the $\omega \to \pi^0\gamma \to 3\gamma$ (1) shown in f) hardly contribute at all. The numbers in brackets are the expectations from the respective Monte Carlos. To PYTHIA(mod) ρ^0_{diff}-states contribute with 50 %, ω-mesons with their three pion decay with 25 %, ρ^0's with 12 %, ϕ-mesons

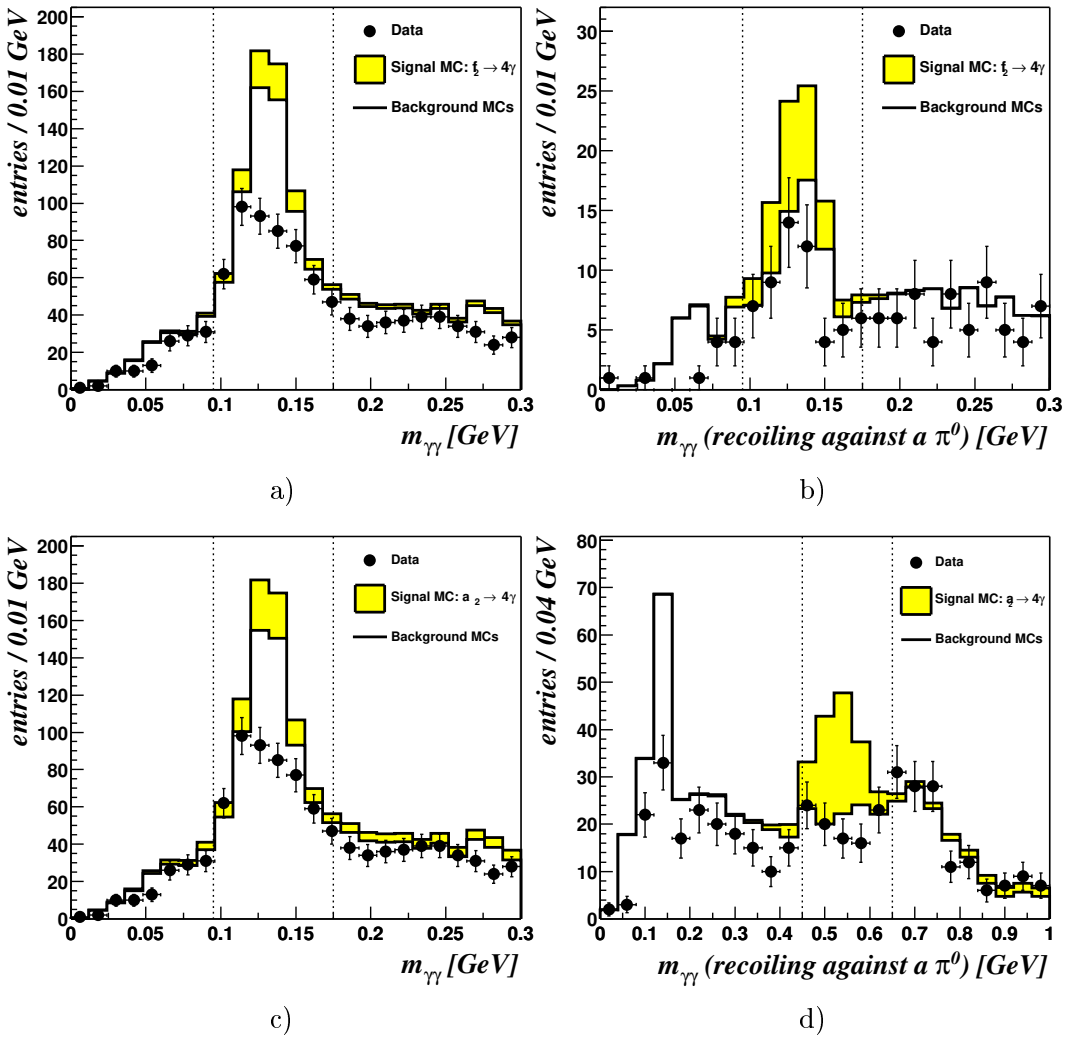

Figure 6.3: $\gamma\gamma$-masses in the four photon sample: *The left panels shows all combinations of the photon-photon masses where in a) the f_2 is shown in grey and in c) the a_2^0. For those events with a pair in the pion window the recoil mass is shown on the right hand side for the f_2 in b) and in d) for the a_2^0. The dashed lines indicate the window from which the pion-candidates are selected in the case of this analysis or η-candidates for the a_2^0-search.*

still with 8 % via the chanel $\phi \to \rho^{\pm}\pi^{\mp}$. Some other states are present with less than five per cent in total. Summing the data histogram yields 53 events compared to 68 expected from the background Monte Carlos.

6.3 Acceptances

The geometrical acceptance for f_2-mesons is found to be larger than for the ω, namely

$$\alpha_{\text{geom}} = 28.8\,\% \pm 0.1\,\% \tag{6.9}$$

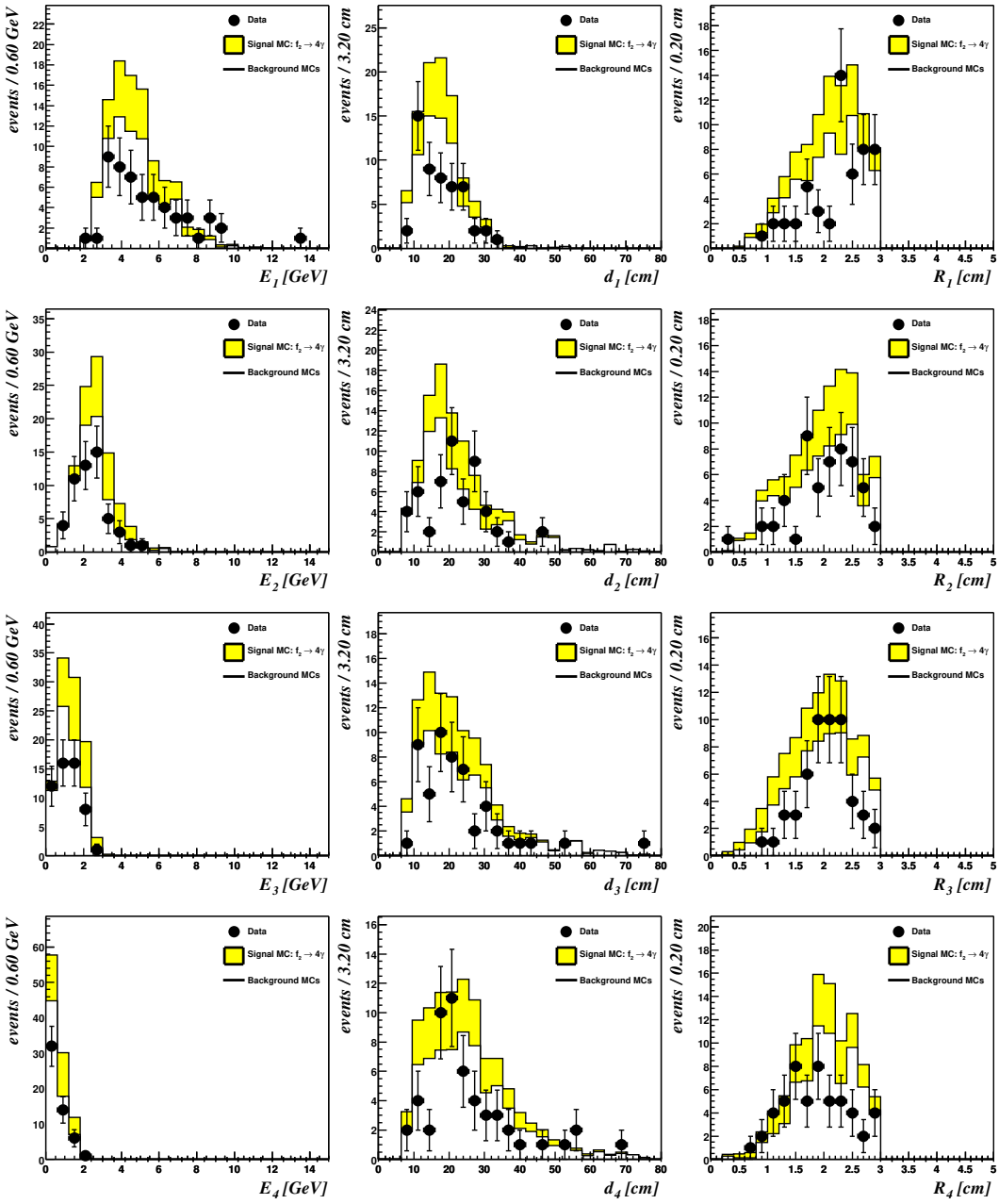

Figure 6.4: Properties of the photons of the four photon sample: *The left column shows the energies of the photon candidates in decreasing order from top to bottom. The middle column shows the transverse distances of these photons and the right column shows their cluster radii.*

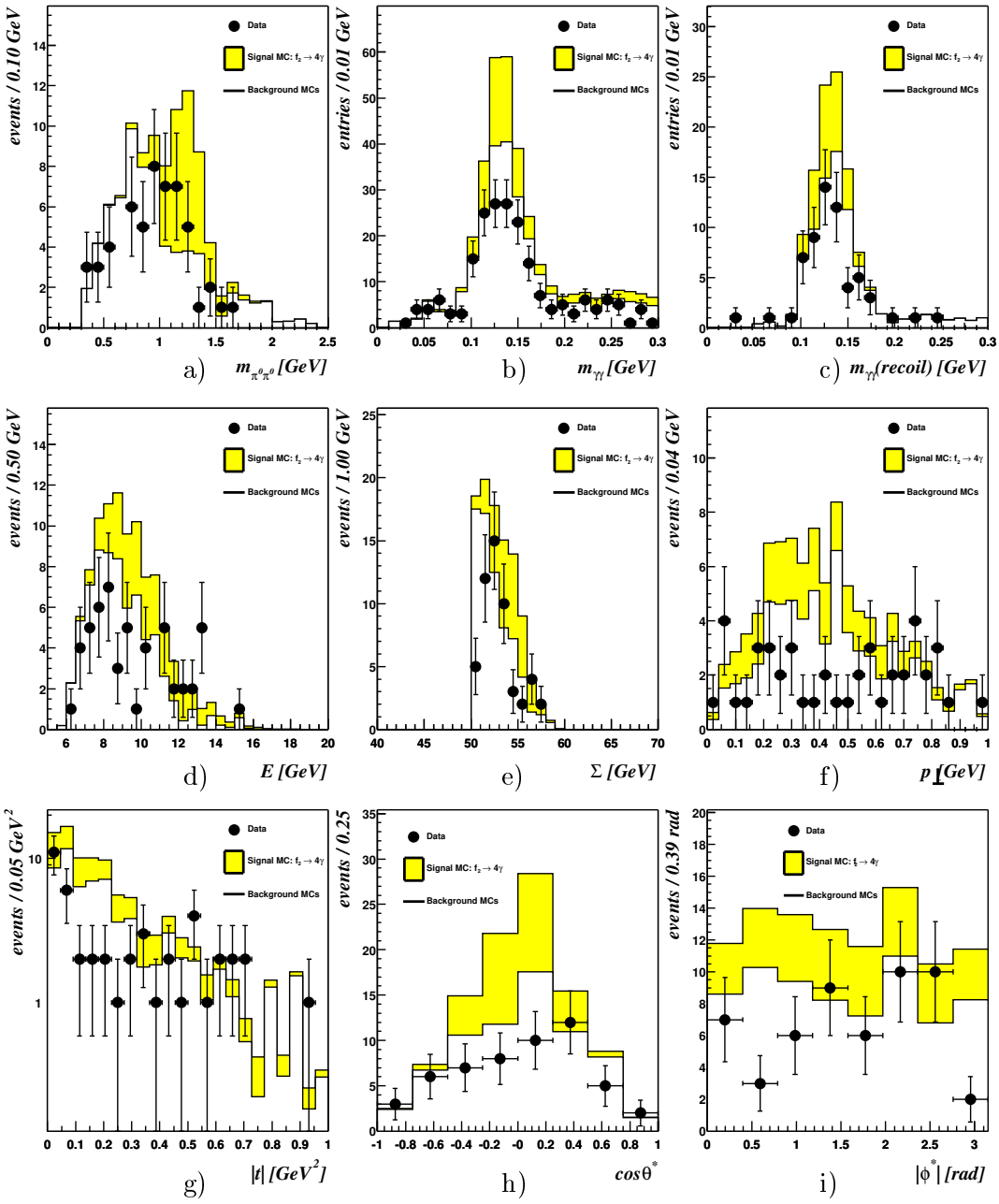

Figure 6.5: Properties of the di-pion system: *Spectra of quantities of the selected four photon sample are shown. Part a) shows the invariant mass, b) the invariant mass of all $\gamma\gamma$ combinations, c) the invariant mass of the two photons recoiling against a pion, d) the total energy, e) the quantity Σ, f) the transverse momentum, g) the momentum transfer squared $|t|$, and the two decay angular distributions $\cos\vartheta^*$ h) and $|\varphi^*|$ i).*

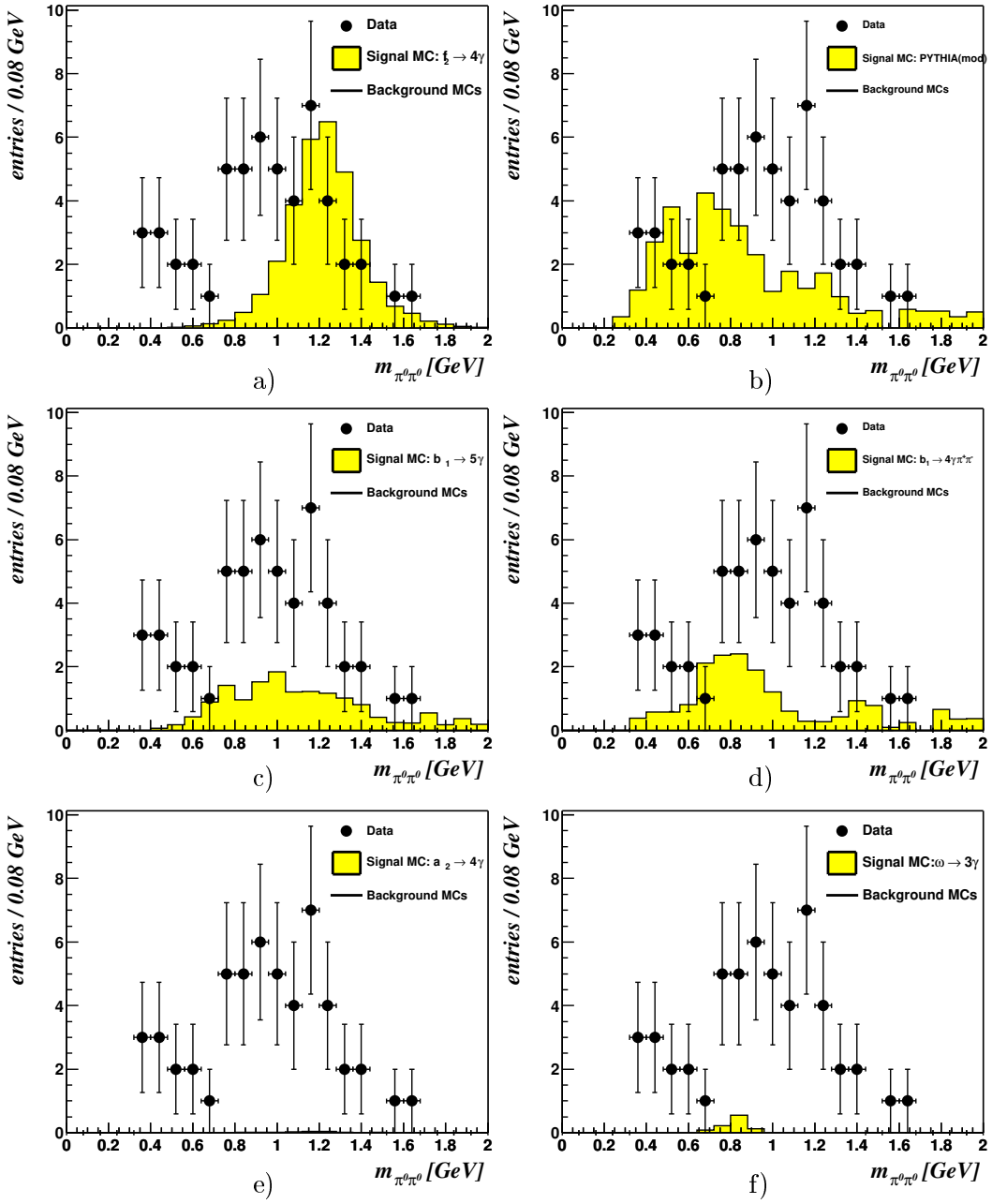

Figure 6.6: Contributions of the Monte Carlos: *The mass distributions of the Monte Carlos contributing to the $\pi^0\pi^0$ sample are shown separately together with data. Part a) shows the signal process $f_2 \to \pi^0\pi^0$, part b) shows the dominant background as predicted by* PYTHIA*(mod). The two panels in the middle c) and d) show the b_1 decaying purely into photons $b_1 \to \omega\pi^0 \to (\pi^0\gamma)\pi^0 \to 5\gamma$ and $b_1 \to \omega\pi^0 \to (\pi^+\pi^-\pi^0)\pi^0 \to \pi^+\pi^-4\gamma$, and panels e) and f) show respectively how the $a_2^0 \to \pi^0\eta$ and the $\omega \to \pi^0\gamma$ contribute.*

compared to only 11 %. Including the response of the trigger results in a reduced total acceptance of

$$\alpha = 6.6\,\% \pm 0.1\,\%\,. \tag{6.10}$$

Figures 6.9 and 6.10 show the acceptance of the f_2 for the decay into two neutral pions as a function of various variables. The left panels show the distributions $f_{\mathrm{gen}}(x)$ as they were generated as full line, the effect of the trigger is visualised by the dashed line and the lowest lying curve finally shows the distributions $f_{\mathrm{acc}}(x)$ of the events accepted. The differential acceptance $\alpha(x) = f_{\mathrm{acc}}(x)/f_{\mathrm{gen}}(x)$ is displayed in the right panels.

A rise of the acceptance in figure 6.11a) as a function of the mass is clearly visible and stronger compared to the ω. And the reason for this behaviour is the very same as for the ω, namely larger masses produce larger relative transverse momenta so the decay photons hit the SpaCal at larger distances evading the distance threshold of the trigger (L2).

This also gives rise to a better acceptance at higher energies, as shown in parts c) and d) where one can see the best acceptance is obtained for energies around 11 GeV and also the energies accessible, are higher.

The acceptance as a function of the polar angle extends further out into the SpaCal (or towards smaller angles) compared to the ω. This is caused on the one hand, by the fact that the f_2 itself is produced with larger $|t|$'s and thus with larger transverse momenta and on the other hand, again, by the fact the f_2 is more massive than the ω. The azimuthal acceptance is flat as expected.

The acceptance of the momentum transfer squared at the proton vertex is nearly independent of $|t|$ and exhibits only a slight declension with increasing $|t|$. Fitting a constant exactly reproduces the acceptance given in equation (6.10) together with the error, and a line-fit yields an intercept of (6.8 ± 0.1) % and the slope turns out to be (-0.8 ± 0.4) %/GeV^{-2}, i. e. within two standard deviations compatible with zero.

One of the origins of the better overall performance is visible in the acceptance of $\cos\vartheta^*$, namely there where the acceptance is largest most of the events are produced, namely at $\cos\vartheta^* \sim 0$ or $\vartheta^* \approx \vartheta \sim \pi/2$.

For $|\varphi^*|$ the acceptance is better around $\pi/2$ than for $|\varphi^*| \approx 0$ and π, though the effect is not as pronounced as for the ω, the reason is the same as described in section 5.3

6.4 Resolutions

Applying the same mass constrained fit to the two pion-candidates as in chapter 5, here improves indeed the quality of the reconstruction of the mass. This is shown in figure 6.7 for Monte Carlo events, where on the left hand side the mass spectrum for di-pion masses $m_{\pi^0\pi^0}$ is shown when the pions were *not* subject to the mass constrained fit, while the pions used to reconstruct the masses $\widehat{m}_{\pi^0\pi^0}$ shown in the right part of the figure, were fitted. And indeed a (Gaussian) fit to the two distributions yield widths of 166 MeV and 155 MeV, respectively with errors of 2.5 MeV only. I.e. the the distribution of constrained pion-candidates is significantly narrower than the corresponding distribution where the pions have not been fitted. This becomes also apparent, comparing parts b) and d) of figure 6.11, where the relative resolutions of the masses[1] $\Delta m_{\pi^0\pi^0}/m_{\mathrm{gen}}$ and $\Delta\widehat{m}_{\pi^0\pi^0}/m_{\mathrm{gen}}$ are shown, and the resolution of the former is 29 % broader than the latter. And looking at the correlations in a) and c) of the figure one sees, that the correlation of $\widehat{m}_{\pi^0\pi^0}$ with the generated mass is also better than the correlation for $m_{\pi^0\pi^0}$ in part a).

[1] The symbol Δ refers to the difference of generated and reconstructed quantity, here the mass $\widehat{m}_{\pi^0\pi^0}$.

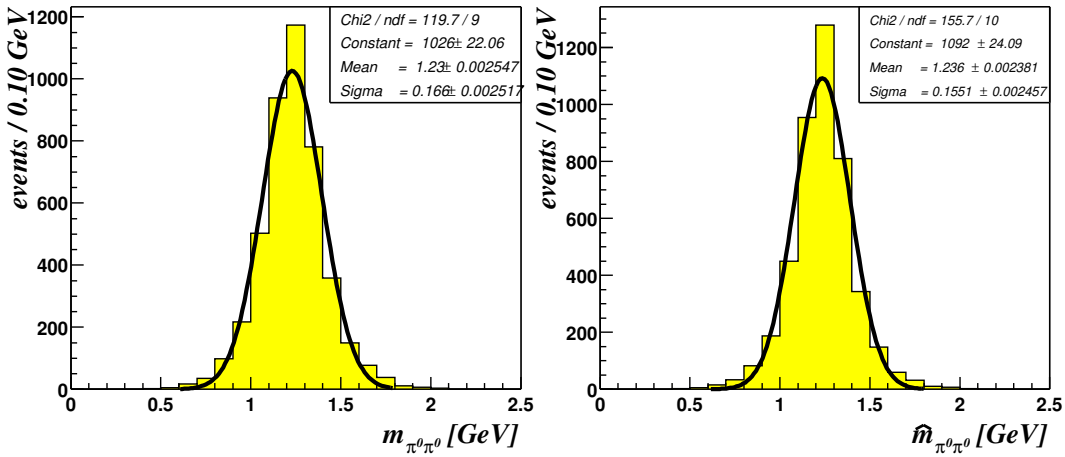

Figure 6.7: Di-pion mass spectrum without and with kinematic fit: *A comparison of Monte Carlo $m_{\pi^0\pi^0}$ spectra is shown where in the left part the pions were not constrained to the nominal pion mass in contrast to the right part where both pion-candidates were subject to a kinematic fit.*

Figures 6.12 – 6.14 show the respective correlations of the generated quantities x_{gen} versus reconstructed values x_{rec} on the left hand side and the relative resolutions $\Delta x/x_{\text{gen}}$ on the right for $x = E, \Sigma, \vartheta, \varphi, |t|, \cos\vartheta^*$ and $|\varphi^*|$.

x	$\Delta x/x_{\text{gen}}$ [%]	Δx
$m_{\pi^0\pi^0}$	7.1	88.3 MeV
$\widehat{m}_{\pi^0\pi^0}$	5.46	68.9 MeV
E	2.9	0.3 GeV
Σ	2.9	1.6 GeV
ϑ	0.2	4.1 mrad
φ	17.4	0.16 rad
$\|t\|$	30.1	0.05 GeV^2
$\cos\vartheta^*$	14.1	0.13
$\|\varphi^*\|$	14.4	0.14 rad
	relative resolution	absolute

Table 6.2: Summary of the resolutions for the f_2: *The table lists the relative and absolute resolutions of the mass, the energy and Σ as shown in figure 6.11, the polar and azimuthal angle shown in figure 6.12 and of $|t|$, $cos\vartheta^*$ and $|\varphi^*|$ shown in figure 6.13*

Table 6.2 summarises the relative and absolute resolutions for the above variables. The resolutions of $\cos\vartheta^*$ and $|\varphi^*|$ are actually better than they appear in the table, since, looking at the correlations in figure 6.13c) and d) one sees a clear correlation and an *anti*-correlation that spoils the values for the resolutions. The reason for this is the assignment

of the analyser that differs for the quantities generated and reconstructed. For the former the first generated pion is chosen, irrespective of its energy, while for the latter the first photon-pair that fulfils the pion-criterion is chosen, but here the energies of the photons are ordered. This results in the observed picture that in ca. 50 % of the cases the analysers (generated and reconstructed) really belong to each other and the rest of the cases the reconstructed analyser corresponds to the second generated pion.

6.5 Result

The mass spectrum shown in figure 6.8 is not suited for the measurement of a cross section, since no clear signal is observable in the data. The invariant mass has been calculated by means of the kinematically constrained pion-four-momenta. The dashed lines visualise an f_2 window

$$\boxed{\widehat{m}_{\pi^0\pi^0} \in (1.0, 1.6)\ \text{GeV}}, \tag{6.11}$$

chosen such that the ratio of signal to background does not become too small and which is used to define the region where the f_2 is expected. Counting the events inside this window, one obtains

$$N_{\text{data}} = 23 \tag{6.12}$$
$$N_{\text{background}} = 19 \tag{6.13}$$
$$N_{f_2} = 28\,, \tag{6.14}$$

which hardly leaves any space for an exclusive f_2-contribution. To quantify this "hardly any space" a procedure is to be applied yielding the minimum and maximum values allowed for a given confidence level. One such procedure is presented in [70], where the construction of confidence belts is described, where for a measured value x_0 the upper and lower bounds, $\mu_{\max}$ and $\mu_{\min}$ are given, in which the true and unknown value μ is likely to be at a given probability α. I.e. if x_0 follows a particular (normalised) probability distribution $f(x|\mu)$ the limits $\mu_{\min}$ and $\mu_{\max}$ are chosen such that

$$\int_{\mu_{\min}}^{\mu_{\max}} \mathrm{d}x\, f(x|\mu) = \alpha\,.$$

This means that the probability that the true value μ is found inside the interval $[\mu_{\min}, \mu_{\max}]$ is α. This method was implemented into a programme in [71] for Poisson processes with known background b. In [72] a method is described how to incorporate a systematic uncertainty σ_{syst} into an upper limit. The new limiting value μ_i', where i stands for either the lower (i =min) or upper (i =max) limit, is given by

$$\mu_i' = \frac{1}{2}\left(\frac{\mu_i + b - x_0}{\mu_i + b}\right)(\mu_i\sigma)^2\,.$$

These methods yield for $x = N_{\text{data}} = 23$, $b = N_{\text{background}} = 18$ and a systematic uncertainty of $\sigma_{\text{syst}} = 23.9$ % that with $\alpha = 95$ % the number of exclusive non-background pion pairs in the f_2 region is

$$N_{\pi^0\pi^0} < 17\,, \tag{6.15}$$

with a lower limit of zero. The systematic uncertainty is discussed in section 6.6. The effect of this uncertainty is rather weak: $[0, 15.0] \xrightarrow{\text{syst}} [0, 17.0]$. Comparing the inequality (6.15) with the number of events expected from f_2-mesons as predicted by the SVM in equation

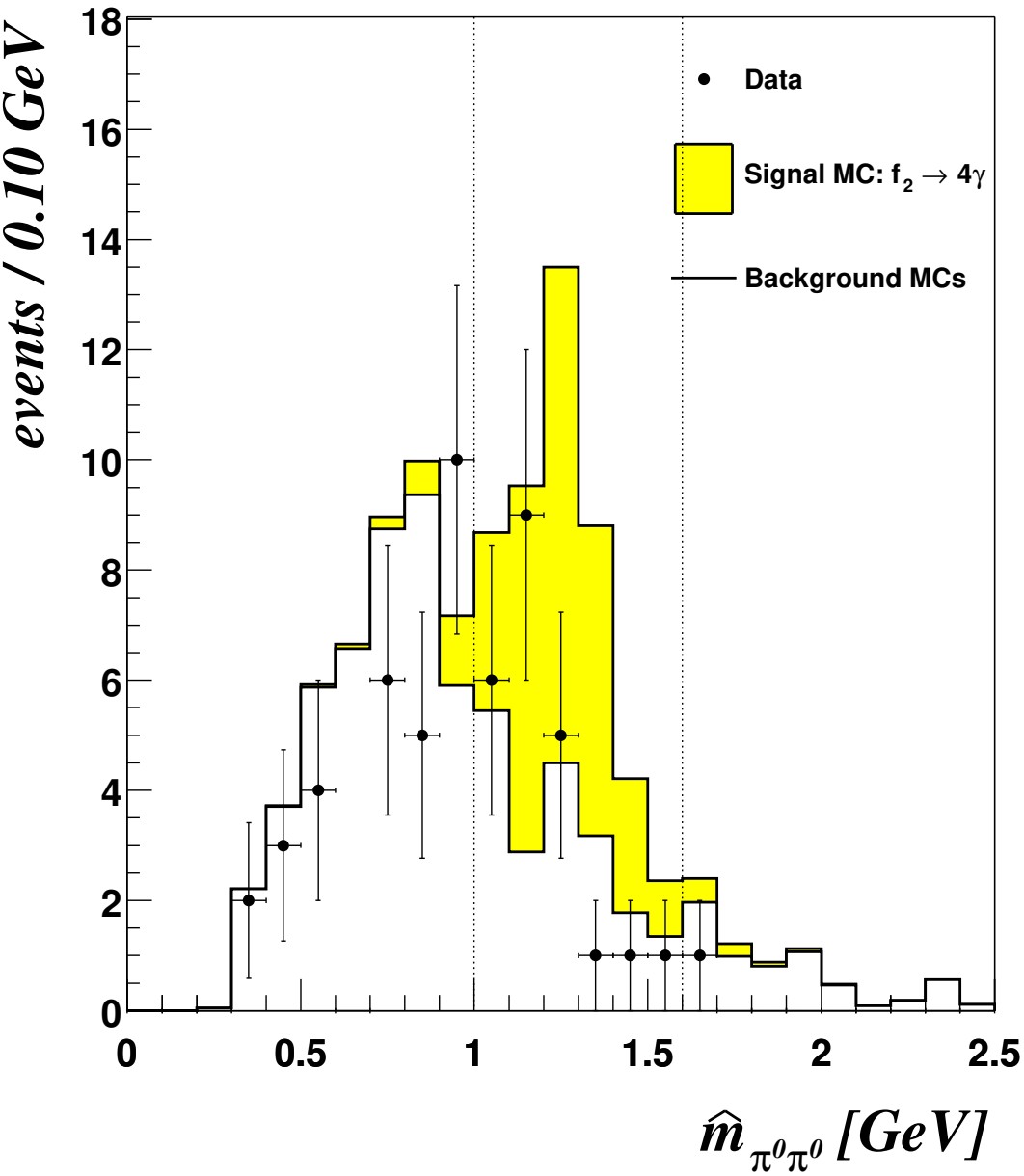

Figure 6.8: Mass distribution of the $\pi^0\pi^0$-sample: *The distribution of the invariant mass of two neutral pions is shown with the cuts (6.6), (6.7) and (6.8) applied. The pion-candidates are constrained to the nominal pion mass by a mass constrained fit. The dots represent the data and the histogram shows the Monte Carlo, where the greyly filled component represents the contribution of the signal process $f_2 \to \pi^0\pi^0 \to 4\gamma$ as predicted by* ØIPIUM *while the open part corresponds to the background which is assumed to be the sum of* PYTHIA*(mod), b_1 with its final states 5γ and $\pi^+\pi^-4\gamma$, and hardly contributing the a_2 and the ω in their four- and three photon final states, respectively.*

(6.14), one sees that the result is not compatible with exclusive f_2 photoproduction by Odderon exchange.

The limit (6.15) can be converted into a corresponding limit on the cross section by means of

$$\sigma(\gamma p \to f_2 X) < \frac{N_{\pi^0\pi^0,\max}}{\alpha\,\Gamma_{f_2\to\pi^0\pi^0}\,\mathcal{L}\mathcal{F}_{\gamma/e}} = 12.4\,\mathrm{nb}\,, \tag{6.16}$$

where $\alpha = 6.6$ % is the total acceptance, $\Gamma_{f_2\to\pi^0\pi^0} = \frac{1}{3}84.6$ % is the ratio for an f_2 to decay into two neutral pions, $\mathcal{L} = 5.41$ pb^{-1} is the integrated luminosity collected by subtrigger S50 in 1996 and $\mathcal{F}_{\gamma/e} = 1.36 \cdot 10^{-2}$ is the integrated photon flux. This limit on the cross section is to be compared with the value given for the production of f_2-mesons in [44] which is 21 nb.

6.6 Systematics

The systematic uncertainty needed to evaluate the confidence belt in the previous section is determined similarly as for the ω.

The checks for model dependences i.e. reweighting of the t- and $\cos\vartheta^*$ distribution of the signal Monte Carlo were not done, since for the determination of the limit (6.15) the model does not enter. But in addition the dependence on the width of the mass window was examined explicitely As in the corresponding section of the ω-chapter the variations were applied to data and Monte Carlo equally, and from the respective number of events inside the f_2-window the mean value and the root mean squared is given in the rows for the classes (1) – (4) for data and the background assumed.

		Data	Bgd-MC
(1)	Varying cuts (γ, π^0-definition, etc.)	22.4±5.0	19.7±5.6
(2)	Varying the energy scales of the SpaCal and the electron tagger within the values quoted for absolute calibration	22.6±1.0	18.2±1.0
(3)	Using different parameterisation for the trigger simulation and the acceptance of the electron tagger.	—	17.9±0.8
(4)	Varying the bounds of the mass window alone	24.7±6.0	19.9±5.5
	mean and RMS of (1) – (4)	22.9±5.0	19.4±5.1
	RMS/mean	21.7 %	26.2 %
		23.9 %	

For item (1) the cuts defining the photon- and pion-candidates were changed, and the window in Σ used to select exclusive events was varied.

To estimate the uncertainty of the absolute energy-scales of the SpaCal and the electron tagger in (2), the energies were varied by ±4 % and ±2 %, respectively.

Item (3) examines the uncertainty due to the parametrisation of the trigger efficiency and the electron tagger and thus affects only the Monte Carlo samples. The parametrisations are the same as in section 5.6.

In (4) explicitely the dependence on the width of the mass window is tested.

Using the ratio of the root mean square and the mean value for all the changes applied, one obtains a relative systematic uncertainty of

$$\sigma_{\mathrm{syst}} = 23.9\,\%\,, \tag{6.17}$$

combining data the background Monte Carlo. As in chapter 5 the background due to beam-gas interactions is negligible. The arguments follow the same lines with the same result as in section 5.1.1

6.7 Summary

In this chapter an attempt to find exclusive f_2-mesons in photoproduction with a mean photon-proton centre of mass energy of 200 GeV has been presented. This attempt failed in the sense that no signal of the expected magnitude has been observed and a limit on the cross section has been given instead on a 95 % confidence level including systematic uncertainties. Table 6.3 summarises the number of events for exclusive di-pion systems

	N	$\sigma(\gamma p \to f_2 X)$ [nb]
data-background	4	2.9
95% limit	17	12.4
SVM	28	20.4

Table 6.3: Summary of event numbers and cross sections for exclusive f_2-photoproduction: *The first column gives the "method" used to extract the values given in the second and third column, respectively. The second column gives the event-numbers and the third column the cross section obtained therewith.*

with masses in the f_2 region and cross sections for f_2 photoproduction assuming that all pion-pairs stem from f_2 decays. In the first row directly the difference of events observed and expected from background Monte Carlo is used, the second row gives the respective upper limit on the maximum compatible value with a probability of 95 %. The last row are the values expected from the f_2 as predicted by COMPIUMrepresenting the expectation if the SVM.

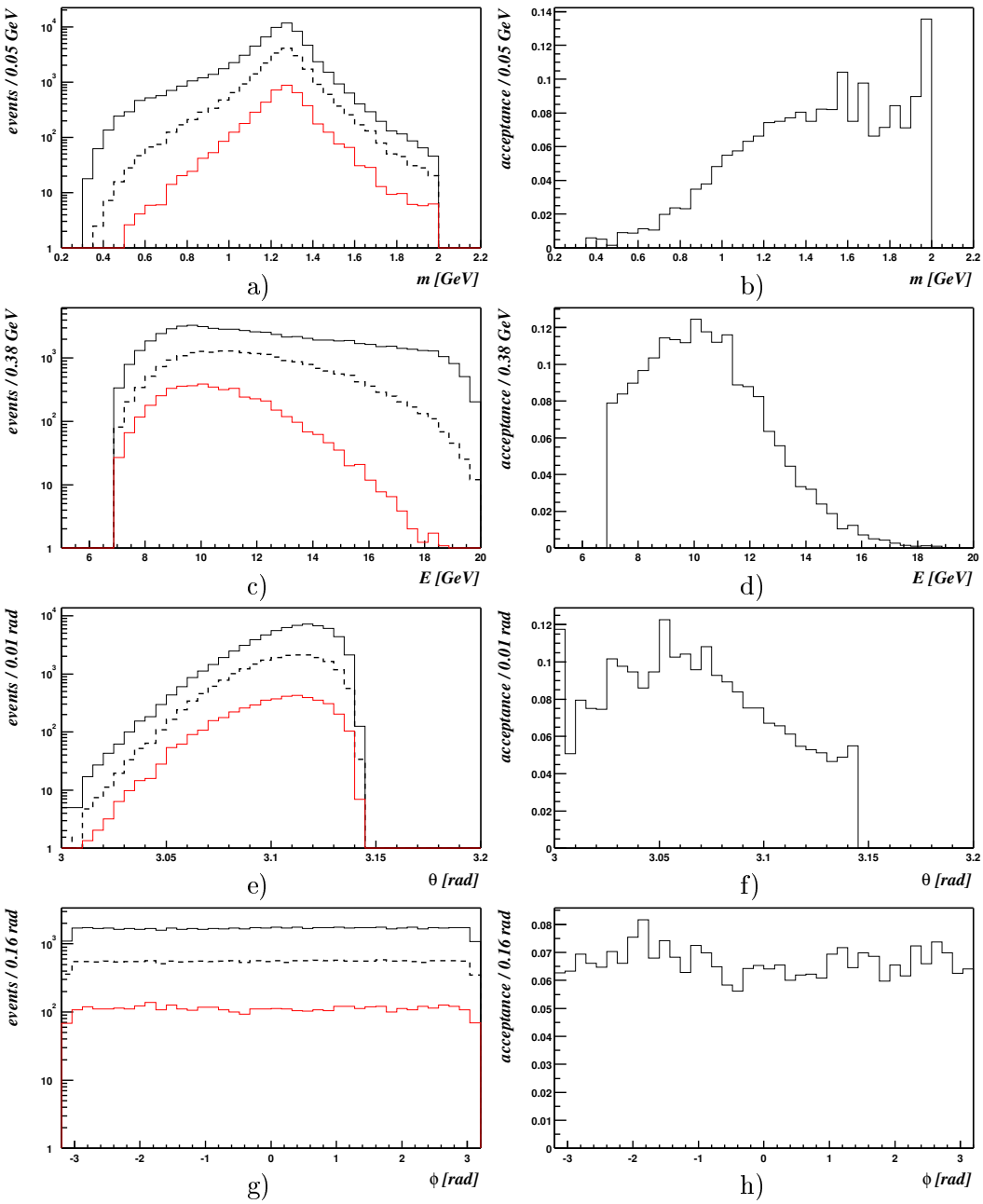

Figure 6.9: Acceptances for the f_2 (I): *The panels on the left show distributions as they were generated (upper most solid line), how they are affected by the trigger (dashed line) and as they are accepted after application of the cuts (bottom most solid line). The right-hand panels display the respective acceptances, defined as the ratio of the solid lines. The distributions shown are (from top to bottom) the mass, the energy, the polar angle and the azimuthal angle.*

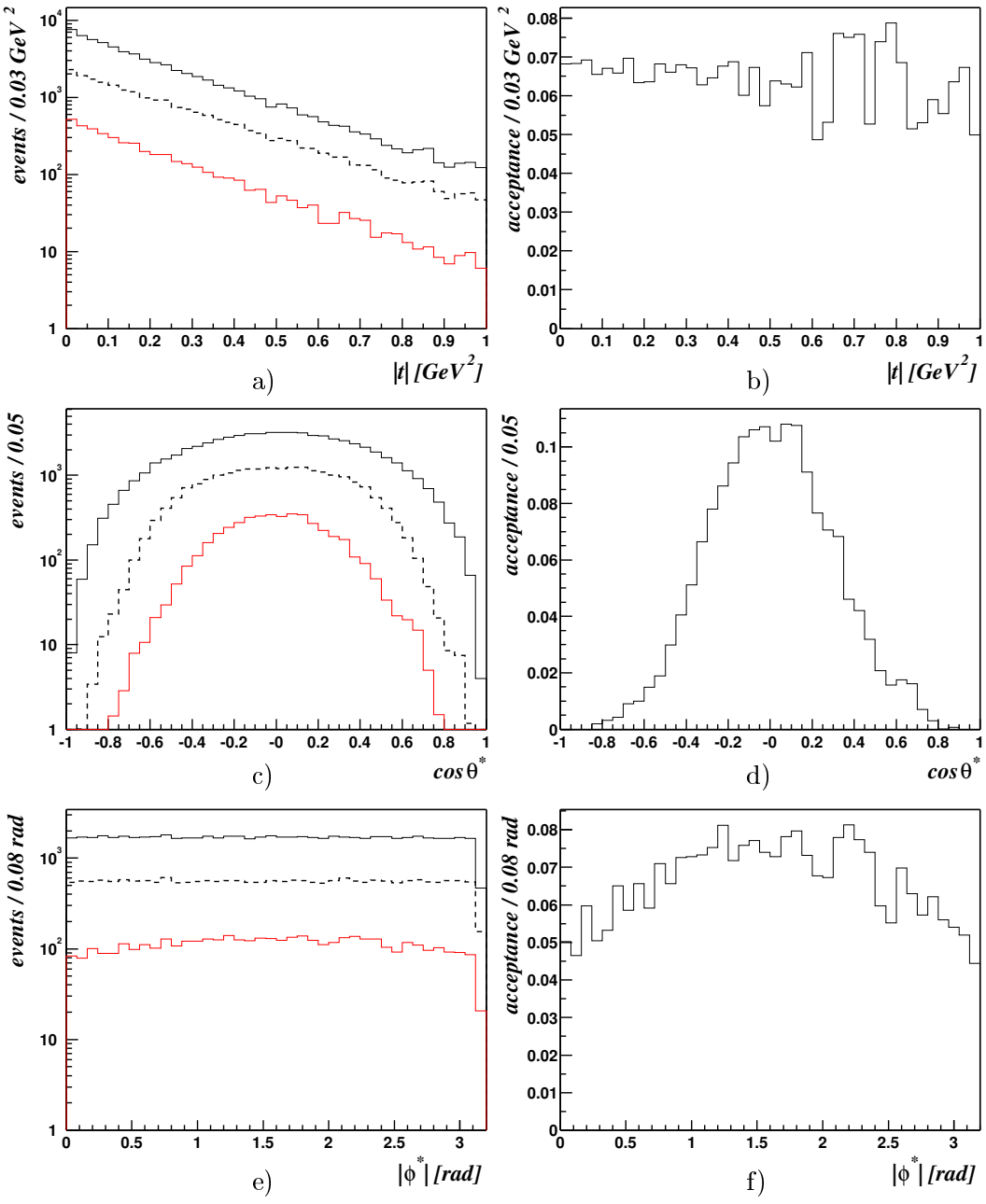

Figure 6.10: Acceptances for the f_2 (II): *The figure shows the same as in figure 6.9 but for the momentum transfer squared at the proton vertex $|t|$ and the decay angular distributions $\cos\vartheta^*$ and $|\varphi^*|$.*

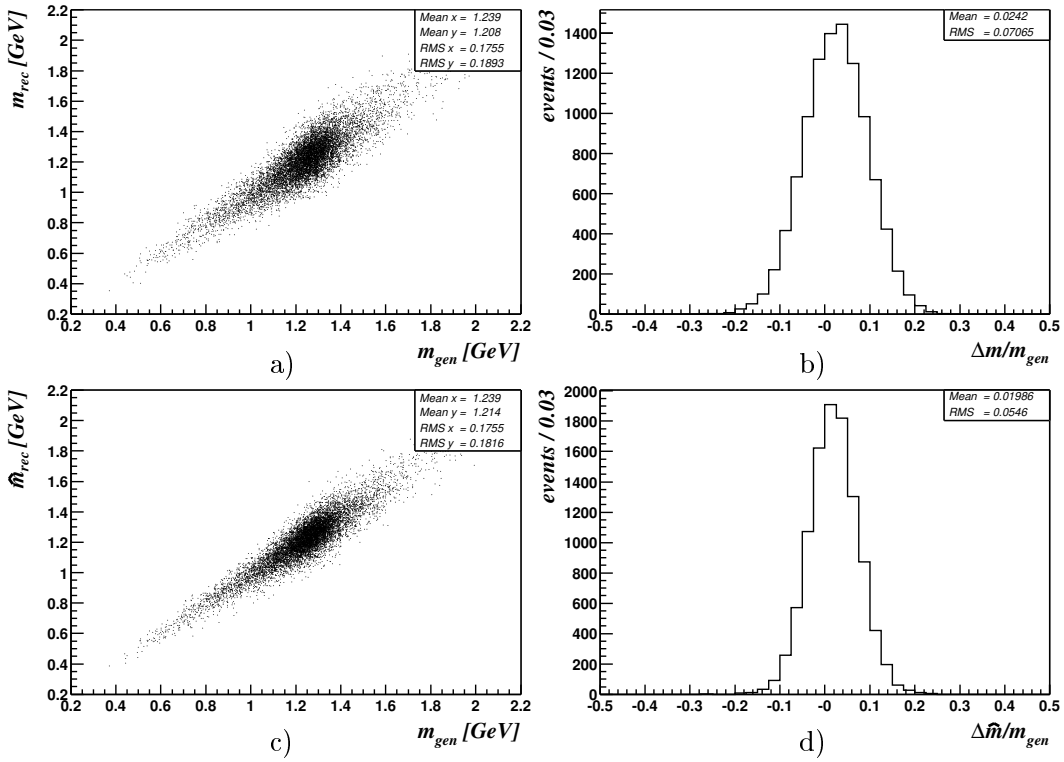

Figure 6.11: Resolutions for the f_2 (I): *The panels on the left hand side show the correlations of reconstructed quantities with their generated values. The right hand side panels show the relative resolutions. In parts a)+b) one can see the correlation and relative resolution of the mass $m_{\pi^0\pi^0}$ when the two pions had not been subject of a mass constrained fit and in c)+d) when this was the case.*

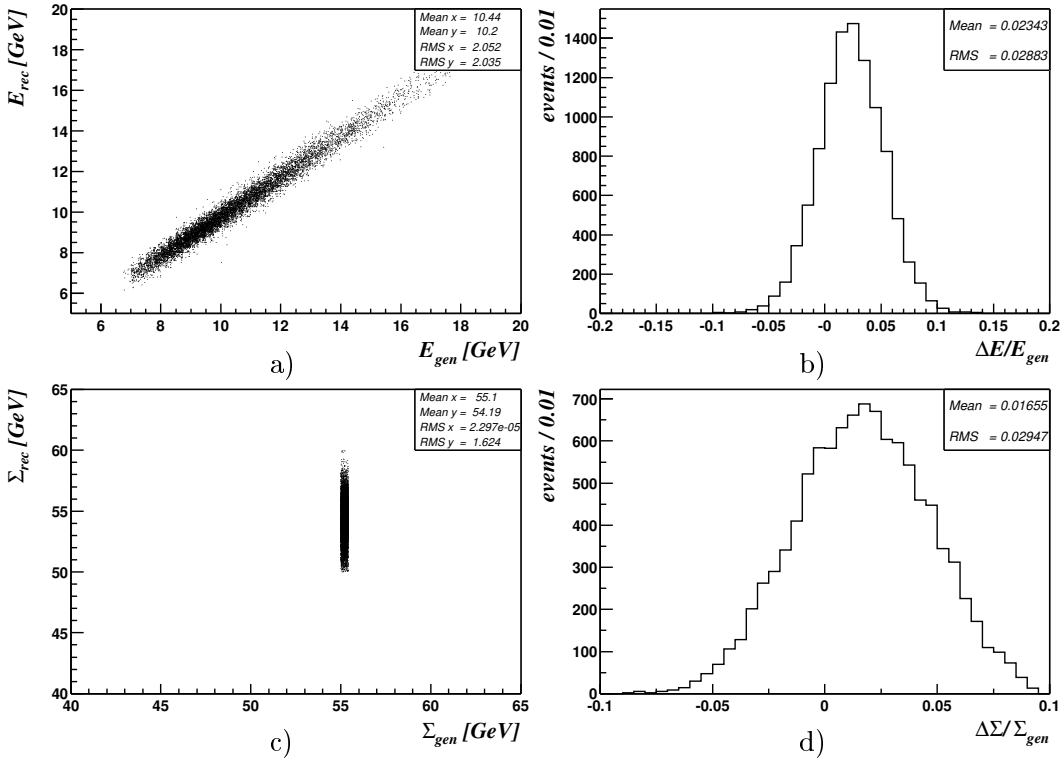

Figure 6.12: Resolutions for the f_2 (II): *The figure shows the same as in figure 6.11 but for the energy E a)+b) and the light-cone minus component Σ c)+d).*

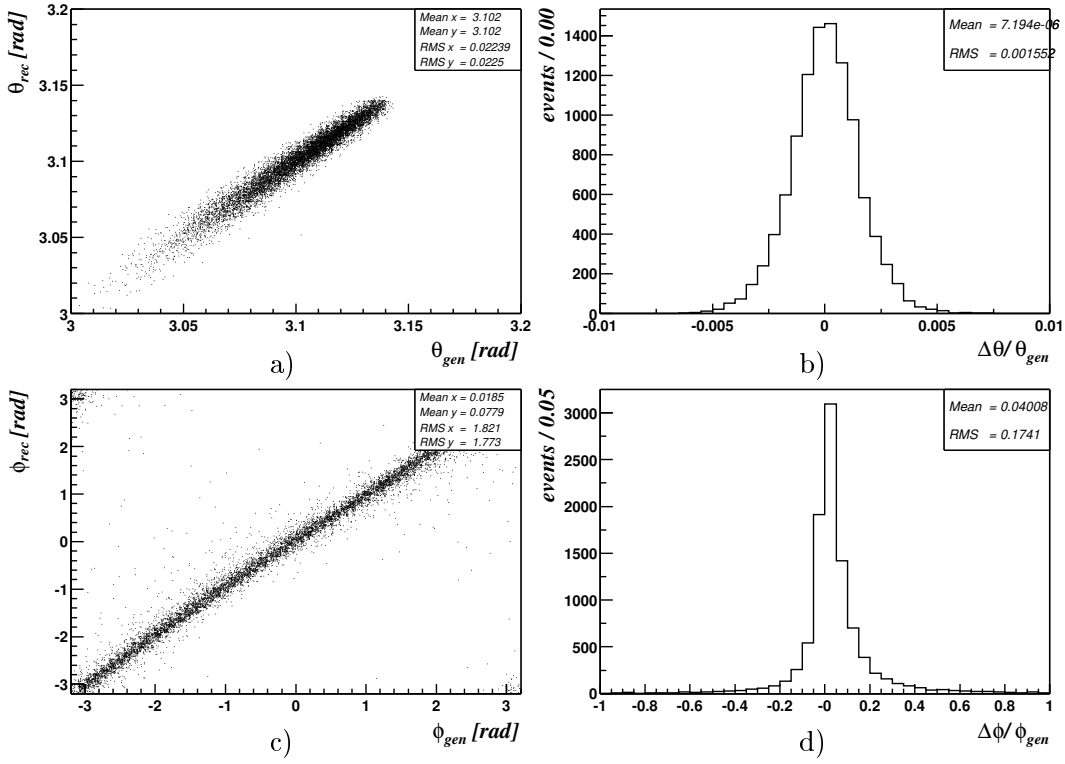

Figure 6.13: Resolutions for the f_2 (III): *The figure shows the same as in figure 6.11 but for the angles ϑ a) + b) and φ c)+d).*

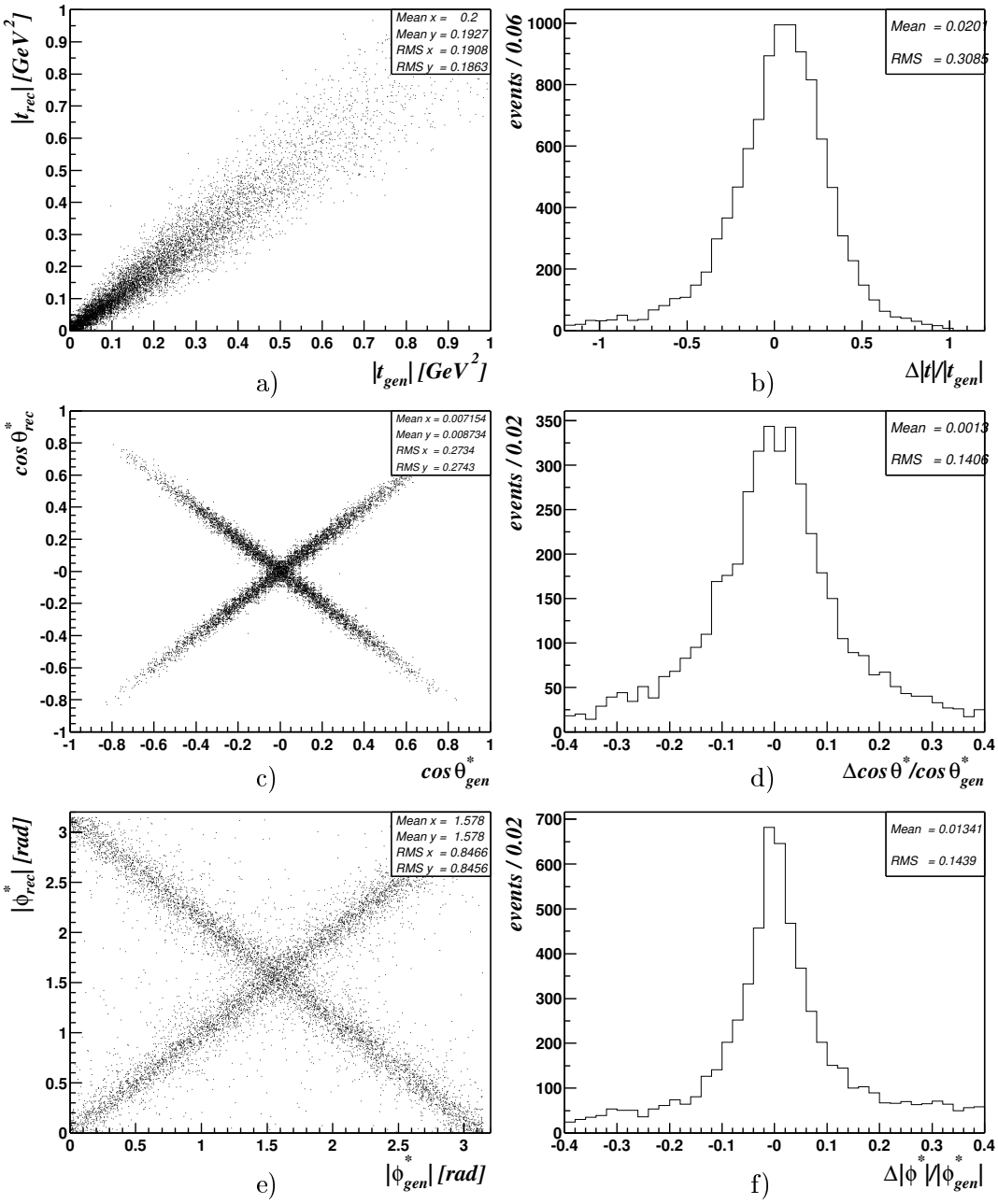

Figure 6.14: Resolutions for the f_2 (IV): *The figure shows the same as in figure 6.11 but for the momentum transfer squared $|t|$ a)+b), the decay-angular distributions $\cos\vartheta^*$ c)+d) and $|\varphi^*|$.*

Chapter 7

Summary, Conclusions and Perspectives

In the previous two chapters analyses have been presented in which two aspects of soft strong interactions have been studied at photon-proton-centre of mass energies around 200 GeV and vanishingly small photon virtualities. The measurements of the cross section and the slope are the first ones performed for the ω-meson at these energies.

The first analysis presented deals with the elastic photoproduction of ω-mesons. In this case the hadronic process is thought to be mediated by the exchange of a Pomeron which couples to the hadronically interacting photon. The values obtained for the cross section and the diffractive slope of $\sigma(\gamma p \to \omega p) = (1.3 \pm 0.2(\text{stat}) \pm 0.2(\text{syst}))\,\mu\text{b}$ and $b = (10.7 \pm 1.1(\text{stat}) \pm 2.0(\text{syst}))\,\text{GeV}^{-2}$, respectively, are in good agreement with what one expects from Regge theory as shown in figure 5.15. The differential cross section shown in figure 5.12 is compared to a prediction of the Stochastic Vacuum Model (SVM) for the ρ^0-meson scaled by a factor 2/9. The agreement is quite satisfactory and demonstrates again that the SVM is indeed capable to describe soft hadronic interactions. The decay angular distributions have been found in accordance with s-channel helicity conserving decays of a vector particle into another vector particle and a scalar. To analyse these distributions a simple approach for real photons has been pursued, since for $Q^2 < 0.01$ GeV^2 this is still a very good approximation. This approach predicts a quadratic dependence on $\cos\vartheta^*$, namely $\mathrm{d}\sigma/\mathrm{d}\cos\vartheta^* \propto 1 + \cos^2\vartheta^*$, and a flat behaviour in φ^*: $\mathrm{d}\sigma/d\varphi^* = \text{const}$. Both expectations valid for real photons in the absence of s-channel helicity violating matrix elements have been confirmed.

This first part has nicely confirmed Regge theory and the notion of the (soft) Pomeron as tools to describe soft hadronic interactions at high energies. And in addition the hypotheses of quark additivity and vector meson dominance that have been used to calculate the Regge-expectation for meson photoproduction are also supported a posteriori by this measurement through its success. This analysis has not the lever arm to shed light on the nature of the Pomeron or to distinguish between models, since to do this both the cross section and the slope ought to be measured as functions of W and Q^2.

Another way to gain some more insight in the Pomeron would be to measure the cross section at larger $|t|$, since there a deviation from the simple exponential decrease is expected, but due to lack of statistics at $|t| > 0.5$ GeV^2 this has not been possible.

What came to some surprise in [2] was the observation of a strong $\omega\pi^0$ exclusive final state at $\langle W \rangle = 200$ GeV, that can be described nicely with a diffractively produced b_1 together with some non-resonant $\omega\pi^0$ production. The cross section was found to be

$\sigma(\gamma p \to \omega\pi^0 X) = (1.07 \pm 0.2(\text{stat}) \pm 0.02(\text{syst}))$ μb. Although it has not been possible to confirm strictly that the signal is due to the presence of a b_1 as due to the limited acceptance in $|\cos\vartheta^*| \approx 1$ a spin-parity analysis has not been performed. But measurements at lower energies [58, 59] reporting a dominant b_1 contribution in $\omega\pi^0$-photoproduction, indicate that a sizeable b_1 contribution is also to be expected at HERA. If the dominance of the b_1 can be confirmed this will pose a challenge to some of the Pomeron models, where the coupling of the Pomeron is assumed to be photon-like; but diffractive production of a $^1P_1$-state from $^3S_1$ is hardly or not all possible.

A further approach to test Pomeron models would be to go to ultra-high energies, since only at very high energies the various models fitted to low and medium energy data start to become significantly different. This is exemplified in appendix A, where three models are compared and fitted to data. In addition a single constant is fitted successfully for $W > 10$ GeV, which is compatible with constant cross section for the energies available so far. But even at energies that may be achieved at THERA[1] where electrons of energies of $E_e = 250$, 400 or 800 GeV from the TESLA machine are brought to collision with protons of $E_p = 920$ GeV from HERA, we are far from "asymtotia", as the photon proton centre of mass energies for $y = 0.5$ are, respectively $W = 480$, 606 and 860 GeV, and the gain in lever arm will not be sufficient to favour or disfavour any of the models on the basis of diffractive vector meson photoproduction. The energy range where this lever arm may be reached is beyond 10^6 GeV, which is hardly foreseeable to be realised in a collider experiment. And the only sources that may serve as a sufficient high energetic beam, are cosmic rays with maximum energies as high as 10^{11} GeV/nucleus. Utilising cosmic ray photons with $E_\gamma \sim 10^{10}$ GeV in a fixed target experiment would give rise to a centre of mass energy of $W \sim 1.5 \cdot 10^5$ GeV for a proton target. But the "luminosity" expected for this kind of experiment is really prohibitive.

The second analysis is concerned with the search for the production of f_2-mesons in the same kinematical regime as the ω-meson, but here the interaction is assumed to be due to the exchange of an Odderon, that couples to the quarks "inside" the photon. But in contrast to the ω it has not been possible to measure a cross section, but only an upper limit of $\sigma(\gamma p \to f_2 X) < 12.2$ nb at a confidence level of 95 % has been given, that seems to rule out the prediction of the SVM of 21 nb. But one has to bear in mind that the cross sections quoted in [43] and [44] have an uncertainty of a factor of two, and for an expectation of $\frac{1}{2}21$ nb the model is no longer ruled out. But this argument does not hold for other channels that have been analysed, namely the exclusive production of π^0-mesons [1, 3] and the iso-vector a_2^0 [2] have also been investigated, and in these channels the findings are very clear: The mass spectra observed are fully compatible with the background and the limits derived are given and compared to the predictions of the SVM in table 7.1 together with the limit derived in this work. Two remarks have to be made on the π^0 values: first, the SVM value is the cross section for the t-region accessible by the experiment and second, in contrast to the publication an intercept of exactly one has been assumed leading to a constant cross section. And here a factor of two cannot save the model prediction.

And second, an argument one may object against this model uncertainty of a factor two is, that in other applications of the SVM the agreement of the model with the data is remarkably good, as shown in figure 5.12 or for example the ρ^0-electroproduction and J/ψ-photoproduction [73][2]. Further examples where the SVM works well are $\gamma^{(*)}\gamma^{(*)}$-reactions [74]: the modified structure function $\tilde{F}_2^\gamma$ of real photons and the total cross

[1] acronym for TESLA×HERA

[2] The mismatch in the case of the ϕ is attributed to wave-function effects.

channel	limits	SVM
	(all values in nb)	
$\gamma p \to f_2 X$	12	21
$\gamma p \to \pi^0 N^*$	38	200
$\gamma p \to a_2^0 X$	62	190

Table 7.1: Comparison of limits on Odderon induced contributions to theory: *The results of the analyses on exclusive pion production [3, 1] and exclusive a_2-production [2] are compared to the predictions of the SVM.*

section for real photons are both very well described by the model, or in the case of γp scattering a variant of the model can nicely describe the energy- and Q^2-dependence of elastic vector meson production and the proton structure function F_2 [75].

Another delicate question concerns the energy dependence of the cross section, although the model – as it is – has no energy dependence i.e. corresponds to a trajectory with unit-intercept, in a wide range of applications, e.g. [74, 75, 76, 77, 78] and [43] the model cross section is modified to rise with W like $(W/W_0)^{2\epsilon}$, where $\epsilon = \alpha(0) - 1$, since — it is argued — the size of the dipole rises with W. If that were true, the size of the dipoles in Odderon induced reactions should increase in the same way as for Pomeron induced processes or γp interactions in general, and thus also their cross section should rise with energy.

In turn the limits given in table 7.1 can be used to gain some information of the intercept by solving

$$\sigma(s) = \sigma_0 \left(\frac{s}{s_0}\right)^{\epsilon}$$

for ϵ, where σ_0 is the SVM cross section at $s_0 = (20\,\mathrm{GeV})^2$ and $\sigma(s)$ is the limit on the cross section measured at $s = W^2$. The results for the three channels are given in table 7.2. These limits lend support to the statement given in [79], where it is claimed that the

	f_2	π^0	a_2^0
$\epsilon_{I\!P} <$	-0.12	-0.35	-0.24

Table 7.2: Limits on the Odderon intercept: *Upper limits on $\epsilon_{I\!P} = \alpha_{I\!P}(0) - 1$ derived from the limits on the cross sections for the exclusive production of f_2- π^0- and a_2^0-mesons.*

Odderon intercept should be very small, $\alpha_{I\!P}(0) \approx -1.6$ based on calculations in the very same model dealing with glueball masses that were found to be in gross accordance with lattice calculations. The reason for the low intercept would be the analogy of a three-gluon system with a baryon, i.e. $gg \leftrightarrow q\bar{q}$ and $ggg \leftrightarrow qqq$, having in mind that the meson- and baryon trajectories are parallel (as are the Pomeron- and the Odderon trajectories) but with largely differing intercepts.

A completely different argument that has been given [80] to explain the absence of the pion is due to its Goldstone boson nature. If the pion were the Goldstone boson of chiral

symmetry, this would imply that the quark model used to construct the pion wave function would not be applicable and the calculation were based on partially wrong assumptions.

A different model for the Odderon [81] was tested in [82] but as the cross section predicted for π^0-, η- and η'-photoproduction are in the range of 50 – 120 pb, only limits on the cross section could be given. The limits on the cross sections on a 90 % confidence level for η- and η' are compared in table 7.3 with the expectations given in [81] for different Odderon couplings $c_{\mathbb{O}}$. A vanishing value of $c_{\mathbb{O}}$ implies no Odderon contribution at all and corresponds to the pure $\gamma\gamma$-process, while for finite values this parameter expresses the Odderon coupling in terms of the Pomeron coupling multiplied by a phase-factor. A nice

	limit	$c_{\mathbb{O}} = 0$	$c_{\mathbb{O}} = -0.05$	$c_{\mathbb{O}} = 0.05$
		(all values in pb)		
η	171	56.4	73	55
η'	79	83.6	92	80

Table 7.3: Limits on other Odderon induced processes: *Limits on the exclusive production of η and η'-mesons obtained in [82] are compared to model predictions [81] for three values of the Odderon coupling $c_{\mathbb{O}}$.*

feature of this particular model is the fact that the cross section is calculated directly as the square of the sum of the two contributing $\gamma\gamma$- and $\gamma\mathbb{O}$-amplitudes and thus automatically includes the interference that manifests for negative $c_{\mathbb{O}}$ as a dip in the $p_\perp$-distribution, and given a signal of any of the pseudoscalar mesons with enough statistics would allow for a clear statement.

From the above findings one can draw two conclusions: (1) The Odderon does not couple (or only weakly) to the the above mesons (or to the proton) at all, or (2) the intercept is too small to see contributions at high energies with the accuracy of the analyses that have been carried out so far. In order to settle this point, one would have to increase statistics which should not be a problem with the advent of HERA II. The magnitude of the Odderon intercept could be measured if successful measurements were carried out at lower energies. This option is feasible in the future as well, in two ways. If the electron is not tagged, one has photon proton centre of mass energies in the range of 40 to 90 GeV; or if the electron is tagged in the 44-m electron tagger, W will be in the range from 46 to 150 GeV. This latter option is in principle the better one, since the range covered in W is larger and it is possible to keep the cut on Σ to select exclusive events easily, but the acceptance of this detector has been rather poor in the last years, so this detector would need significant improvement before it may be used for a high statistics analysis.

Again, as for the vector mesons the THERA option of the TESLA accelerator could be awaited, but if the Odderon intercept really lies below unity, this may turn out as a dead end. On the other hand for the relativistic heavy ion collider (RHIC) it is discussed to replace one gold-beam with a proton-beam. And operated in a mode were the particles do not collide but pass each other at impact parameters of about one nuclear radius, the gold-nuclei serve as a high intensity source of photons which subsequently may interact hadronically with a proton, in the same way as it occurs at HERA. Processes of this kind have already been observed by the STAR-Collaboration [83], namely diffractive ρ^0-production. Assuming that the photon proton centre of mass energy may be calculate analogously as in ep-scattering, one has for $y = 0.5$ centre of mass energies of $W = 8$ GeV for nucleon nucleon centre of mass energies of $\sqrt{s_{NN}} = 130$ GeV. So one would go back to

fixed target energies with a high intensity "photon-beam". In this energy range already a number of experiments have been carried out, so that this option cannot be regarded as a most promising one to gain new insight concerning the Odderon problem.

One could go even one step further and install a complete new experiment in the HERA tunnel. This hypothetical experiment would be mounted with an array of detectors to detect the scattered electron to provide the largest possible coverage in W. And keeping the strategy of purely photonic final states, one would build the calorimeter to detect the photons at a rather large distance from the interaction point, minimising the error induced by the lack of tracks needed to reconstruct the interaction point. And a larger distance simultaneously increases the angular acceptance that may eventually allow for spin parity analyses on more solid grounds.

Having gone through the experimental programme suggested above, be it an extended version of the analysis presented in this thesis or the ones presented in [1] and [2] with larger statistics and W range, or, be it the proposed experiment, one should finally be able to confirm or reject one of the above statements, whether the Odderon couples at all or whether the intercept is small. Any outcome is interesting by itself and will hopefully trigger further interest and discussion.

Assuming for the moment, it turns out that the Odderon does not couple at all in soft processes, then the following question arises immediately: Why is there a Pomeron in both soft and hard processes but the Odderon appears only in hard processes? Since in perturbative QCD the two-gluon exchange and the three-gluon exchange appear on equal footing. And the Odderon *is* needed to reproduce the angular distributions in the dip-region and at large $|t|$ [84] in pp and $\bar{p}p$ scattering. And it turns out that in all[3] perturbative calculations the intercept of the Odderon turns out to be close to unity [85, 86, 87]. Though also the intercept calculated for the so-called BFKL-Pomeron shrinks from ~ 1.4 down to 1.09 when going from a hard regime to soft scattering, it appears not particular likely that a shrinkage – if present – should be that strong to push the intercept of the Odderon below a value out of experimental vicinity. If that were the case the notion of the Odderon as "leading trajectory with $C = -1$" would be no longer appropriate, since for $\alpha_{\mathcal{O}}(0) < 0.5$ the leading trajectory with $C = -1$ would be the ω. In this context, further experimental verification of the perturbative Odderon is urgently needed, and there is a number of publications [88, 89, 90, 91] dealing with the exclusive production of mesons in a perturbative regime. In most of these publications the hard scale is provided by the mass of the charm quark in the case of the η_c. But some present calculations for light mesons in particular for the π^0, η, f_2 and the a_2^0 but with the hard scale provided by the momentum transfer, either Q^2 or t larger than a few GeV^2. The cross section reported there range from $\sim 1 - 100$ pb, but hope is uttered that due to corrections at NLO large corrections are to be applied, giving rise to a factor of $4 - 5$, similar to the NLO-correction in the BFKL-case, though there, the corrections turned out to be negative.

So, if the Odderon will not be found, or even proven not to exist, QCD owes an explanation. But on the other hand, if it is finally found, the community will lean back with relief and say "So, what? We all knew it has to be there."

[3] at least to the knowledge of the author

Appendix A

Cross Sections and the Pomeron: Simple Pole versus Untitarised Models

A brief review of the three approaches presented in [34] is given, concentrating on total cross sections and their application to vector meson-photoproduction.

Total hadron hadron cross section may be equally well parametrised by the following formula[1]:

$$\sigma_{\mathrm{tot}}^{\overset{(-)}{A}B} = a_i^{AB} + Y_+^{AB} s^{-\eta_+} \mp Y_-^{AB} s^{-\eta_-} \tag{A.1}$$

with

$$a_i^{AB} = \begin{cases} X^{AB} s^{\epsilon} & i=0 \quad I\!P \text{ as a simple pole} \quad \text{(RRP)} \\ \lambda^{AB}\left[A + B\ln(s/s_0)\right] & i=1 \quad \text{(RRL)} \\ \lambda^{AB}\left[A + B\ln^2(s/s_0)\right] & i=2 \quad I\!P \text{ fully unitarised} \quad \text{(RRL2)} \end{cases} \tag{A.2}$$

The parameter λ^{AB} in the above equation is a measure of the interaction in terms of the pp-cross section and quantifies to some extend the quality of the additive quark model (AQM), that states, that the meson-proton cross section should roughly scale with proton-proton cross section like the number of quarks involved $\sigma_{\mathrm{tot}}^{\pi p}/\sigma_{\mathrm{tot}}^{pp} = 2/3$. This assumption is found to be nicely confirmed in [34].

Applying,

$$\sigma_{\mathrm{tot}}^{\rho^0 p} \approx \sigma_{\mathrm{tot}}^{\omega p} \approx \frac{1}{2}\left(\sigma_{\mathrm{tot}}^{\pi^+ p} + \sigma_{\mathrm{tot}}^{\pi^- p}\right) \text{ and} \tag{A.3}$$

$$\sigma_{\mathrm{tot}}^{\phi p} \approx \sigma_{\mathrm{tot}}^{K^+ p} + \sigma_{\mathrm{tot}}^{K^- p} - \sigma_{\mathrm{tot}}^{\pi^- p}\,, \tag{A.4}$$

one obtains the respective parameters for X^{Vp} and $Y_{\pm}^{Vp}$ for the photoproduction case. These relations for $hp \to Vp$ are given in table A.1. In table A.2 one finds the numerical values for the three models RRP, RRL and RRL2, respectively.

Using equation (1.76) together with the parameters of table 1.3, the models can be fitted to data: Table A.3 lists the values one obtains when the parameters X^{Vp} and $Y_{\pm}^{Vp}$ are fitted for $W > 5$ GeV shown in the left part and for $W > 3$ GeV in the right. According to equation A.3 Y_+^{Vp} for both the ρ^0 and the ω were fixed to zero. If this constraint is dropped, the fit does not improve significantly but the values found have that large errors

[1] The respective real parts of the scattering amplitudes are given in [34].

	$\rho^0(\omega)$	ϕ
X	$X^{\pi p}$	$2X^{Kp} - X^{\pi p}$
Y_+	$Y_+^{\pi p}$	$2Y_+^{Kp} - Y_+^{\pi p}$
Y_-	0	$-Y_-^{\pi p}$

Table A.1: From $hp \to Vp$-scattering: *The table list the conversion rules for $hp \to Vp$-scattering. λ may be obtained by the replacement $X \to \lambda$.*

	$\rho^0(\omega)$	ϕ
	RRP	
X [mb]	12.08 ± 0.29	9.44 ± 0.54
Y_+ [mb]	26.2 ± 0.74	1.96 ± 1.36
Y_- [mb]	0	-7.63 ± 0.72
	RRL	
λ	0.68 ± 0.01	0.60 ± 0.01
Y_+ [mb]	61.2 ± 2.4	38.2 ± 5.4
Y_- [mb]	0	-5.8 ± 0.2
	RRL2	
λ	0.64 ± 0.01	0.51 ± 0.01
Y_+ [mb]	21.2 ± 0.6	-2.2 ± 1.6
Y_- [mb]	0	-7.5 ± 0.7
	using AQM	

Table A.2: Summary of model parameters: *The parameters are obtained by applying the additive quark model to parameters fitted in [34] in hadron-hadron scattering for three parametrisations for the total cross section.*

	ρ^0	ω	ϕ	ρ^0	ω	ϕ
			RRP			
X [mb]	12.93 ± 0.51	11.74 ± 2.07	9.21 ± 0.61	12.57 ± 0.39	10.67 ± 0.98	8.36 ± 0.24
Y_+ [mb]	27.9 ± 5.3	27.3 ± 21.9	0 ± 87.2	32.4 ± 1.7	41.3 ± 3.6	0 ± 11.1
Y_- [mb]	0	0	-20.6 ± 14.4	0	0	0.65 ± 2.70
			RRL			
λ	0.71 ± 0.04	0.64 ± 0.15	0.50 ± 0.18	0.70 ± 0.03	0.54 ± 0.09	0.59 ± 0.10
Y_+ [mb]	65.1 ± 1.6	60.6 ± 4.4	43.6 ± 13.9	65.6 ± 0.8	63.8 ± 2.1	33.4 ± 3.5
Y_- [mb]	0	0	-52.4 ± 65.4	0	0	-3.0 ± 13.6
			RRL2			
λ	0.69 ± 0.03	0.62 ± 0.11	0.50 ± 0.17	0.67 ± 0.02	0.56 ± 0.05	0.53 ± 0.07
Y_+ [mb]	21.7 ± 5.2	21.6 ± 22.2	-4.1 ± 83.9	26.6 ± 1.8	36.2 ± 3.9	-28.7 ± 23.3
Y_- [mb]	0	0	-20.0 ± 163.4	0	0	-35.4 ± 32.4
	fitted for $W > 5$ GeV			fitted for $W > 3$ GeV		

Table A.3: Summary of fitted model parameters: *The values of the models RRP, RRL and RRL2 for the three light vector mesons for fits with $W > 5$ GeV (left) and $W > 3$ GeV (right).*

that they are essentially undetermined. This is also visible for the ϕ where there has no such constraint been imposed. This can partly be cured by lowering the lower limit of the fit, as has been done successfully by $W_{\min} = 5$ GeV $\rightarrow$ 3 GeV.

It has to be noted that the point of the ω at $W = 200$ GeV has not been included in the fit.

Concluding, one may remark, that the additive quark model works rather fine and the deviations one obtains by fitting the model parameters does not change them compared to the simple assumptions in equations (A.3) and (A.4).

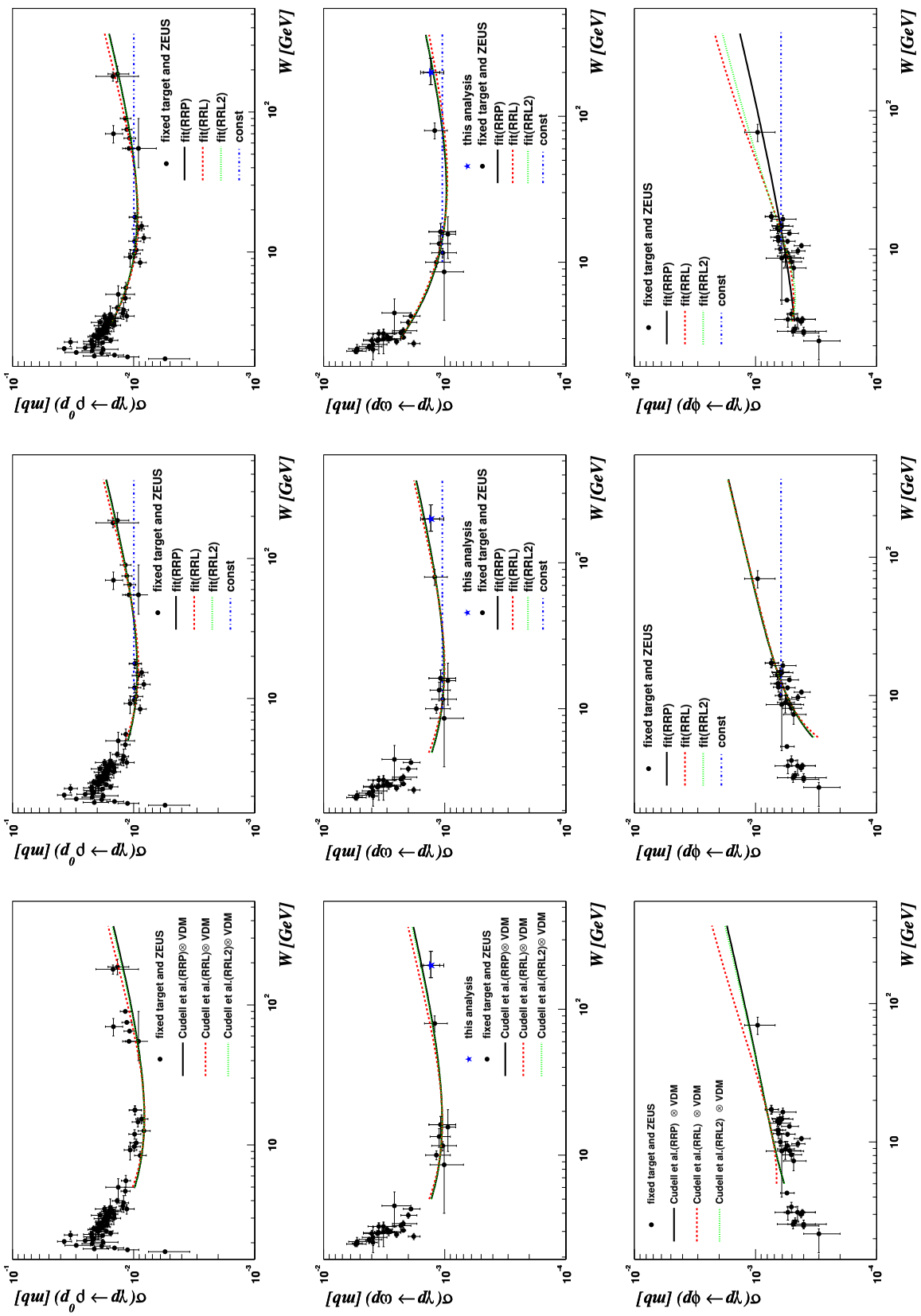

Figure A.1: Comparison of prediction and fits to the RRP, RRL and RRL2 models: *For the three light vector mesons ρ^0, ω and ϕ the three left-most plots compare the predictions of the models RRP, RRL and RRL2 to data. The middle row shows the results of the fits for $W > 5$ GeV and the right row for $W > 3$ GeV*

Appendix B

Cross Sections in a Dipole Model

To evaluate cross sections in a dipole model, one needs the wave functions of the initial and final states. If one is only interested in the total γp cross section the square of the photon wave function is sufficient, and in leading order it is given by [38]

$$|\psi_{\gamma,T}(z,r)|^2 = \frac{3\alpha}{4\pi^2}\sum_q e_q^2\left[(z^2+\bar{z}^2)\epsilon_f^2 K_1^2(\epsilon_q r)+m_q^2 K_0^2(\epsilon_q r)\right] \tag{B.1}$$

$$|\psi_{\gamma,L}(z,r)|^2 = \frac{3\alpha}{2\pi^2}\sum_q e_q^2\left[4Q^2z^2\bar{z}^2 K_0^2(\epsilon_q r)\right]\,, \tag{B.2}$$

where the sum runs over the light quark flavours u, d, s with charges e_q and masses m_q, the momentum fraction of the anti-quark is $\bar{z}=1-z$ and $K_0(x), K_1(x)$ are the McDonald-Bessel functions. The quantity $\epsilon_q = z\bar{z}+m_q^2$ plays the rôle of an energy.

For vector meson production the corresponding meson wave function in the final state is needed. In [40] a model for the vector meson wave functions is presented. The z-dependence is modelled according to a Wirbel-Stech-Bauer ansatz [92], and in r a Gaussian behaviour for a harmonic oscillator is assumed. The product $\psi_V^\dagger\psi_{\gamma,\lambda}$ can be written in the factorised form

$$\psi_{V,\lambda}^\dagger(z,r)\psi_{\gamma,\lambda}(z,r) = e\gamma_V f_{V,\lambda}(z)g_{V,\lambda}(r)h_{V,\lambda}(z,r)\,, \tag{B.3}$$

where γ_V is related to the photon-meson coupling $f_V^2/4\pi$ via $\gamma_V = m_V/f_V$ and with

$$f_{V,\lambda}(z) = \mathcal{N}_{V,\lambda}\sqrt{z\bar{z}}\exp\left[-\frac{1}{2}\frac{M_V^2}{\omega_{V,\lambda}^2}(z-1/2)^2\right] \tag{B.4}$$

$$g_{V,\lambda}(r) = \exp\left[-\frac{1}{2}\omega_{V,\lambda}^2 r^2\right] \tag{B.5}$$

$$h_{V,\lambda}(z,r) = \begin{cases} -2(z\bar{z})^2 Q K_0(\epsilon r) & \text{for } \lambda = L \\ \dfrac{1}{M_V}\left[\omega_{V,\lambda}^2\epsilon r(z^2+\bar{z}^2)K_1(\epsilon r)+m^2K_0(\epsilon r)\right] & \text{for } \lambda = T \end{cases} \tag{B.6}$$

The oscillator frequencies $\omega_{V,\lambda}$ and the normalisations $\mathcal{N}_{V,\lambda}$ are calculated, solving the following set of coupled equations:

$$\omega_{V,\lambda} = \frac{\pi\gamma_V}{\sqrt{2N_c}\hat{e}_V}\left[\int \mathrm{d}z\,\chi_{V,\lambda}(z)f_{V,\lambda}^2(z)\right]^{1/2} \tag{B.7}$$

$$1 = \mathcal{N}_{V,\lambda}\int \mathrm{d}z\,\tilde{f}_{V,\lambda}(z)\tilde{\chi}_{V,\lambda}(z) \tag{B.8}$$

where $f_{V,\lambda}(z)$ is the same as in equation (B.4), defining $\tilde{f}_{V,\lambda}(z)$ and the auxiliary functions $\chi_{V,\lambda}(z)$, $\tilde{\chi}_{V,\lambda}(z)$:

$$
\begin{aligned}
f_{V,\lambda}(z) &= \mathcal{N}_{V,\lambda}\tilde{f}_{V,\lambda}(z) \\
\chi_{V,\lambda}(z) &= \begin{cases} z^2\bar{z}^2 & \text{for } \lambda = L \\ \dfrac{(z^2+\bar{z}^2)\omega_{V,T}^2 + m^2}{M_V^2} & \text{for } \lambda = T \end{cases} \\
\tilde{\chi}_{V,\lambda}(z) &= \begin{cases} z\bar{z} & \text{for } \lambda = L \\ \dfrac{(z^2+\bar{z}^2)\omega_{V,T}^2 + \frac{1}{2}m^2}{z\bar{z}M_V^2} & \text{for } \lambda = T \end{cases}
\end{aligned}
$$

The resulting frequencies and normalisations are listed in table B.1.

$V(M_V)$ [GeV]	$\hat{e}_V$	γ_V [MeV]	$\omega_{V,L}$	$\mathcal{N}_{V,L}$ [GeV]	$\omega_{V,T}$	$\mathcal{N}_{V,T}$ [GeV]
$\rho(770)$	$1/\sqrt{2}$	153	0.33	4.477	0.21	4.865
$\omega(782)$	$1/3\sqrt{2}$	45.8	0.30	4.546	0.21	4.854
$\phi(1019)$	$1/3$	79.1	0.37	4.587	0.27	5.703
$J/\psi(3097)$	$2/3$	270	0.68	5.127	0.57	2.915

Table B.1: *Parameters for the vector meson wave functions.*

B.1 The Dipole Cross Section of Forshaw et al.

The specific model utilised here is the model of Forshaw et al. [38], where HERA photo- and electroproduction ($Q^2 > 0$) data were fitted to fix the model parameters. The model itself is given by

$$\hat{\sigma}(s,r) = \hat{\sigma}_{\text{soft}}(s,r) + \hat{\sigma}_{\text{hard}}(s,r) \tag{B.9}$$

with

$$\hat{\sigma}_{\text{soft}}(s,r) = a_0^s \left(1 - \frac{1}{1+(a_1^s r + a_2^s r^2)^2}\right)(r^2 s)^{\lambda_s} \tag{B.10}$$

$$\hat{\sigma}_{\text{hard}}(s,r) = (a_1^h r + a_2^h r^2 + a_3^h r^3)(r^2 s)^{\lambda_h} e^{-\nu_h^2 r} \tag{B.11}$$

where $\hat{\sigma}_{\text{soft}}(s,r)$ describes the soft interaction at high energies (i.e. photoproduction) and $\hat{\sigma}_{\text{hard}}(s,r)$ the high-energy electroproduction data. Both the soft and hard components are to be convoluted with photon wave functions to obtain the total γp-cross section. In addition to this high energy part a Reggeon component is added to accommodate the rise of the cross section at low energies. The parameters found in [38] are listed in table B.2.

For the evaluation of the vector meson cross sections only equations (B.10) and (B.11) were used and the Reggeon part was thus neglected. The comparision of the total γp-cross section and the elastic vector meson cross sections with data is shown in figure 1.12.

soft		hard		auxiliary	
a_0^s	30.05(fixed)	a_1^h	0.99±0.07	B	6.4±2.40
a_1^s	0.12±0.01	a_2^h	0.7±0.1	c^2	0.205±0.004
a_2^s	−0.202±0.005	a_3^h	−6.23±0.08	R	6.46±0.03
λ_s	0.06(fixed)	λ_h	0.386±0.005	m^2	0.08(fixed)
		ν_h^2	−4.36±0.02		

Table B.2: Fit parameters: *Given are the paramters fitted to HERA photo and electroproduction data. (Taken from [38])*

Appendix C

Decay Angular Distributions

When studing decay angular distributions, one usually starts with the incoming photon expressed in terms of the spin density matrix $\rho_{\lambda\lambda'}$. The spin density matrix is related with the lepton tensor $L_{\mu\nu}$ introduced in equation (1.12) via a change of coordinates: $L_{\mu\nu} \to \rho_{\lambda\lambda'}(\gamma) = \epsilon^{\mu}_{\lambda}\epsilon^{\nu *}_{\lambda'}L_{\mu\nu}$, with the polarisation vectors of equation (1.29). If the interaction leading to the final state meson (either vector meson (V) or tensor meson (T)) is expressed by the amplitude A, the corresponding spin density matrix is given by

$$\rho(M) \propto A\rho(\gamma)A^{\dagger}\,. \tag{C.1}$$

Let D denote the operator describing the decay, then the decay angular distribution is given as the expectation value of D:

$$\langle A\rangle \equiv W = \ \mathrm{Tr}\rho(M)D\,. \tag{C.2}$$

As well as the photon, both the density matrix and the decay operator are naturally expressed in terms of helicities:

$$\rho(M) = \rho_{\alpha\beta}(M) \quad \text{and} \quad D = D_{\alpha\beta}\,, \tag{C.3}$$

where the helicity indices α and β may take values of $-J, -J+1, \ldots, J$ where J is the spin of a state decaying into two particles with helicities λ_1 and λ_2. As already mentioned above the results of the measurement are given in terms of[1] ϑ and φ, so a transformation from the helicity base to a base of the observables is needed. This transformation is given by the Wigner rotation functions [93, 94]:

$$D_{\alpha\beta} \to D_{\alpha\beta}(\vartheta,\varphi) = \frac{2J+2}{4\pi}\frac{\sum_{\lambda_1\lambda_2}|T_J(\lambda_1,\lambda_2)|^2 e^{-i(\alpha-\beta)\varphi}d^J_{\alpha\Lambda}(\vartheta)d^J_{\beta\Lambda}(\vartheta)}{\sum_{\lambda_1\lambda_2}|T_J(\lambda_1,\lambda_2)|^2}\,, \tag{C.4}$$

with $\Lambda = \lambda_1 - \lambda_2$. The decay matrix and the spin density matrix are both hermitian

$$\rho_{\alpha\beta} = \rho^*_{\beta\alpha} \quad \text{and} \quad D_{\alpha\beta} = D^*_{\beta\alpha} \tag{C.5}$$

and obey the following symmetry relations

$$\rho_{-\alpha-\beta} = (-1)^{\alpha-\beta}\rho_{\alpha\beta} \quad \text{and} \quad D_{-\alpha-\beta} = (-1)^{\alpha-\beta}D^*_{\alpha\beta}\,, \tag{C.6}$$

reducing the number of independent matrix elements significantly. The functions $T_J(\lambda_1,\lambda_2)$ are given in table C.1. For a precise and thorough discussion the reader is referred to [94]. The Wigner functions $d^J_{\alpha,\Lambda}(\vartheta)$ can be read off the tables given in [32] or [94], respectively.

[1] The superscripts '*' to indicate the hadronic centre of mass frame are dropped here, as there is danger of mixing coordinate systems.

Decay	$T_J(\lambda_1, \lambda_2)$
$0^+ \to 0^-0^-$	G_0
$1^- \to 0^-0^-$	$\sqrt{1/3}\ 2G_1 p$
$2^+ \to 0^-0^-$	$\sqrt{2/15}\ 4G_2 p^2$
$3^+ \to 0^-0^-$	$\sqrt{1/70}\ 16G_3 p^3$
$0^0 \to 1^-1^-$	$\delta_{\lambda_1\lambda_2}\lambda_1 gp\sqrt{s}$
$1^\mp \to 1^-0^\mp$	$\sqrt{1/3}\ \lambda_1 gp\sqrt{s}$
$2^+ \to 1^-0^-$	$\sqrt{1/10}\ \lambda_1 gp^2\sqrt{s}$
$1^- \to \frac{1}{2}\frac{1}{2}$	$-e/\sqrt{3}\ 2(m_1\delta_{\lambda_1\lambda_2} + \sqrt{s/2}\delta_{\lambda_1-\lambda_2})$

Table C.1: Decay factors: *$T^J(\lambda_1, \lambda_2)$ for various decays (taken from [94]).*

C.1 The Decay $\omega \to \pi^0\gamma$

For this decay the sixth row of table C.1 is needed to get $T_1(\lambda_1, \lambda_2)$. Identifying particle 1 with the photon and particle 2 with the pion, yields $\lambda_1 = \pm 1$ and $\lambda_2 = 0$. Assuming VMD the spin density matrix of the ω-meson is diagonal $\rho(\omega) = \mathrm{diag}(\rho_{+1+1}, \rho_{00}, \rho_{+1+1})$ and according to s-channel helicity conservation equals the photon spin density matrix. Therefore only the diagonal elements of the decay matrix $D_{\alpha\alpha}$ are needed. According to table C.1 $T_J(\lambda_1\lambda_2)$ is proportional to λ_1 and thus vanishes for $\lambda_1 = 0$ and further as only the squares are involved $|T_1(+1)|^2 = |T_1(-1)|^2$. Thus in equation (C.4) only two terms contribute, and one finds

$$\begin{aligned} D_{\alpha\alpha}(\vartheta, \varphi) &= \frac{3}{8\pi}\left(d^1_{\alpha 1}(\vartheta)^2 + d^1_{\alpha -1}(\vartheta)^2\right) \\ &= \frac{3}{16\pi}\mathrm{diag}\left((1+\cos^2\vartheta), 2\sin^2\vartheta, (1+\cos^2\vartheta)\right) \end{aligned} \tag{C.7}$$

where in the last step the explicite expressions for the d-functions were inserted. The decay angular distribution is thus given by

$$W(\vartheta, \varphi) = \frac{3}{8\pi}[\rho_{+1+1}(1+\cos^2\vartheta) + \rho_{00}\sin^2\vartheta] \tag{C.8}$$

For photoproduction, where the photons are nearly on-shell one expects longitudinal photons to contribute only marginally, i.e. $\rho_{00} \to 0$ in the limit $Q^2 \to 0$. From equation (C.8) follows in particular that there is no dependence on the azimuthal angle to be expected in the case of s-channel helicity conservation. This may occur if the photon-meson transition contains off-diagonal elements.

C.2 The Decay $f_2 \to \pi^0\pi^0$

According to [44] the f_2 is produced predominantly with helicities $\lambda = \pm 2$. This means for the density matrix $\rho(f_2)$ that all matrix elements vanish except for $\rho_{+2+2}(f_2)$ and $\rho_{-2-2}(f_2)$. Thus for the trace only the corresponding decay matrix elements D_{+2+2} and D_{-2-2} are needed.

For the decay into spinless particles equation (C.4) simplifies to

$$\begin{aligned} D_{\alpha\beta}(\vartheta,\varphi) &= \frac{5}{4\pi} e^{-i(\alpha-\beta)\varphi} d^2_{\alpha 0}(\vartheta) d^2_{\beta 0}(\vartheta) \\ &= Y^2_\alpha(\vartheta,\varphi)^* Y^2_\beta(\vartheta,\varphi) \end{aligned} \tag{C.9}$$

For the decay angular distribution only the case $\alpha = \beta = 2$ is needed: $Y^2_2(\vartheta,\varphi) = \sqrt{15/32\pi}\ \sin^2\vartheta e^{2i\varphi}$, and thus

$$D_{+2+2}(\vartheta,\varphi) = D_{-2-2}(\vartheta,\varphi) = \frac{75}{128\pi^2}\sin^4\vartheta\,. \tag{C.10}$$

Consequently, the decay angular distribution is given by

$$W(\vartheta,\varphi) = \frac{75}{64\pi^2}\rho_{+2+2}\sin^4\vartheta\,, \tag{C.11}$$

where $\rho_{+2+2} = \rho_{-2-2}$ was used.

Bibliography

[1] Tobias Golling. Search of Odderon Induced Contributions to Exclusive π^0 Photoproduction at HERA. Diplomarbeit, Univerität Heidelberg, 2001. HD-KIP-01-03.

[2] Christoph von Cube. Exklusive Photoproduktion der Mesonen b_1 und a_2 bei HERA. Diplomarbeit, Univerität Heidelberg, 2001.

[3] Oliver Nix. *Suche nach odderoninduzierten Beiträgen in exklusiver π^0-Produktion mit dem Detektor H1 bei HERA*. PhD thesis, Univerität Heidelberg, 2001. HD-KIP-01-05.

[4] F. Halzen and A. D. Martin. *Quarks and Leptons*. John Wiley and sons, 1984.

[5] Ch. Friberg and T. Sjöstrand. *JHEP 0009:100 (*`hep-ph/0007314`*)*, 2000.

[6] D. Schildknecht and H. Spiesberger. `hep-ph/9707447`, 1997.

[7] Amaldi et al. *Nucl. Phys.* **B166***:301*, 1980.

[8] A. V. Barnes et al. *Phys. Rev. Lett.* **37***:76*, 1976.

[9] ZEUS Collaboration, J. Breitweg, et al. *Eur. Phys. J.* **C14***:200*, 2000.

[10] ZEUS Collaboration, M. Derrick, et al. *Z. Phys,* **C72***:253*, 1997.

[11] ZEUS Collaboration, M. Derrick, et al. *Z. Phys,* **C72***:399*, 1996.

[12] H1 Collaboration, S. Aid, et al. *Nucl. Phys.* **B463***:3*, 1996.

[13] WIRE Collaboration, T. J. Chapin, et al. *Phys. Rev.* **D31***:17*, 1985.

[14] OMEGA Collab., D. Aston, et al. *Nucl. Phys.* **B209***:56*, 1982.

[15] W. Struczinski et al. *Nucl. Phys.* **B108***:45*, 1976.

[16] J. Ballam et al. *Phys. Rev.* **D7***:3150*, 1973.

[17] SPEC Collaboration, J. Busentitz, et al. *Phys. Rev.* **D40***:1*, 1989.

[18] LAMP Collaboration, D. P. Barber, et al. *Z. Phys.* **C26***:343*, 1984.

[19] OMEGA Collaboration, M. Atkinson, et al. *Nucl. Phys.* **B231***:15*, 1984.

[20] A. M. Breakstone et al. *Phys.Rev.Lett.* **47***:1782*, 1981.

[21] R. M. Egloff et al. *Phys. Rev. Lett.* **43***:1545;* Erratum-ibid **44***:690*, 1979; 1980.

[22] J. Abramson et al. *Phys. Rev. Lett.* **36***:1428*, 1976.

[23] D. P. Barber et al. *Phys. Lett.* **B79***:150*, 1978.

[24] H.-J. Behrend et al. *Phys. Lett.* **B56***:408*, 1975.

[25] OMEGA Collaboration, D. Aston, et al. *Nucl. Phys.* **B172***:1*, 1980.

[26] Omega Photon Collaboration, M. Atkinson, et al. *Z. Phys.* **C27***:233*, 1985.

[27] S. Nusinov. *Phys. Lett.* **34***:1286*, 1975.

[28] A. Donnachie and P. V. Landshoff. *Nucl. Phys.* **B311***:509*, 1989.

[29] J. Cudell. *Nucl. Phys.* **B336***:1*, 1990.

[30] H1 Collaboration, C. Adloff, et al. *Z. Phys.* **C76***:613*, 1997.

[31] L. Łukaszuk and B. Nicolescu. *Nuov. Ciem. Lett.* **8***:405*, 1973.

[32] D. E. Groom et al. *Eur. Phys. J.* **C15***:1*, 2000.

[33] A. Donnachie and P. V. Landshoff. *Nucl. Phys.* **B348***:297*, 1991.

[34] J. Cudell et al. *Phys. Rev.* **D61***:034019*, 2000.

[35] A. Donnachie and P. V. Landshoff. *Phys. Lett.* **B296** *227*, 1992.

[36] G. A. Schuler and T. Sjöstrand. *Nucl. Phys.* **B 407***:539*, 1993.

[37] Jörn Grosse-Knetter. *Measuremnt of Elastic ω Photoproduction at HERA.* PhD thesis, Universität Hamburg, (1997. DESY-F35-97-02.

[38] J. R. Forshaw, G. Kerley, and G. Shaw. *Phys. Rev.* **D50***:074012*, 1999.

[39] H. G. Dosch, E. Ferreira, and A. Krämer. *Phys. Rev.* **D50***:1992*, 1994.

[40] H. G. Dosch, T. Gousset, G. Kulzinger, and H. J. Pirner. *Phys. Rev.* **D55***:2602*, 1997.

[41] M. Rüter and H. G. Dosch. *Phys. Lett.* **B380***:177*, 1996.

[42] M. Rüter, H. G. Dosch, and O. Nachtmann. *Phys. Rev.* **D59***:014018*, 1999.

[43] E. Berger et al. *Eur. Phys. J.* **C9***:491*, 1999.

[44] E. Berger et al. *Eur. Phys. J.* **C14***:673*, 2000.

[45] D. H. Perkins. *Introduction to High Energy Physics.* Addison Wesley Publishing Company, 1987.

[46] Block et al. *Phys. Rev.* **D60***:054024*, 1999.

[47] H1 Collab., I. Abt, et al. The H1 detector. *DESY-preprint H1-96-01*, 1996.

[48] Martin Swart. *Mass Spectroscopy of Neutral Mesons in the Photon Hemisphere at HERA.* PhD thesis, Univerität Heidelberg, 2000. HD-KIP-00-17.

[49] B. Andrieu et al. *Nucl. Instr. and Meth.* **B350***:57*, 1994.

[50] T. Nicholls et al. *Nucl. Instr. and Meth.* **B374***:149*, 1996.

[51] R. D. Apphun et al. *Nucl. Instr. and Meth.* **B382***:395*, 1996.

[52] R. D. Apphun et al. *Nucl. Instr. and Meth.* **B386***:397*, 1997.

[53] J. Engelen, M. Klein, and R. Rückel. Reconstruction of (x, Q^2) and extraction of of structure functions in neutral current scattering at HERA. In *Physics at HERA*, volume 1, pages 23–43, 1991.

[54] B. List and A. Mastroberadino. DiffVM – A Monte Carlo Generator for Diffractive Processes in *ep* Scattering. In *DESY workshop on Monte Carlo Generators for HERA Physics*, `http://www.desy.de/~heramc/mclist.html`, 1998/99.

[55] Crystal Ball Collaboration, H. Marsiske, et al. *Phys. Rev.* **D41***:3324*, 1990.

[56] C. Adloff et al. *Eur. Phys. J.* **C14***:371*, 2000.

[57] T. Sjöstrand. *Computer Physics Commun.* **82***:74*, 1994.

[58] OMEGA Collaboration, M. Atkinson, et al. *Nucl. Phys.* **B243***:1*, 1984.

[59] J. E. Brau et al. *Phys. Rev.* **D37***:2379*, 1988.

[60] J. Meyer. *Guide to the Simulation Program H1SIM*, 1991. H1-Software Note.

[61] *GEANT User's Guide* . CERN Program Library Long Writeup W5013 Detector.

[62] Doug Jansen. *The H1 Reconstruction Program.* `http://www-h1.desy.de/h1/www/general/home/intra_home.html` .

[63] The H1 SpaCal Group. *DESY-report* **95-250**, 1995.

[64] V. Boudry et al. *H1-internal report* **H1-0395-430**, 1995.

[65] Barbara Clerbaux. *Electroproduction Elastique de Mésons ρ à HERA*. PhD thesis, Universit'e Libre de Bruxelles, 1999. DESY-THESIS-1999-001.

[66] S. Levonian. H1-homepage of the luminosity system. `http://www-h1.desy.de/h1/www/h1det/lumi`.

[67] H. Albrecht. ARGUS Kinematical Analysis Language (KAL). (unplished).

[68] G. Kulzinger, H.G.Dosch, and H.J.Pirner. *Eur. Phys. J.* **C7***:73*, 1999.

[69] ZEUS Collaboration, M. Derrick, et al. *Phys. Lett.* **B377***:259*, 1996.

[70] G. J. Feldman and R. D. Cousins. *Phys. Rev.* **D57***:3873*, 1998.

[71] J. A. Aguilar-Saavedra. *Computer Physics Commun* **130***:190*, 2000.

[72] R. D. Cousins and V. L. Highland. *Nucl. Instr. and Meth.* **A320***:331*, 1992.

[73] H. G. Dosch et al. *Phys. Rev.* **D55***:2602*, 1997.

[74] A. Donnachie, H. G. Dosch, and M. Rüter. *Eur. Phys. J.* **C 13***:141*, 2000.

[75] M. Rüter. *Eur. Phys. J.* **C7***:233*, 1999.

[76] A. Donnachie, H. G. Dosch, and M. Rüter. *Phys. Rev.* **D59***:074011*, 1999.

[77] A. Donnachie and H. G. Dosch. `hep-ph/0106169`, 2001.

[78] A. Donnachie and H. G. Dosch. *Phys. Lett.* **B502***:74*, 2001.

[79] A. B. Kaidalov and Yu. A. Simonov. *Phys. Lett.* **B477***:163*, 2000.

[80] H. G. Dosch. private communication.

[81] W. Kilian and O. Nachtmann. *Eur. Phys.J.* **C5***:317*, 1998.

[82] Thomas Berndt. Exklusive produktion der mesonen η, η' und ω in multi-photon-endzuständen bei hera. Diplomarbeit, Univerität Heidelberg, HD-IHEP 97-10.

[83] F. Meissner. Choherent Photon-Pomeron and Photon-Photon Interactions in Ultra-Peripheral Collisions at RHIC. In *Photon 2001*, 2001. (to appear in confernce proceedings).

[84] Desgrolard et al. *Eur. Phys. J.* **C16***:499*, 2000.

[85] P. Gauron, L. .N. Lipatov, and B.Nicolescu. *Z. Phys.* **C63***:253*, 1994.

[86] R. A. Janik and J. Wosiek. *Phys. Rev. Lett.* **82***:1092*, 1999.

[87] M. A. Braun, P. Gauron, and B. Nicolescu. *Nucl. Phys.* **B542***:329*, 1999.

[88] A. Schäfer, L. Mankiewicz, and O. Nachtmann. Diffractive $\eta_c, \eta, \eta', J/\psi$ and ψ' production in electron-proton collisions at HERA energies. In *Physics at HERA*, volume 1, pages 243–251, 1991.

[89] R. Engel, D. Yu. Ivanov, R. Kirschner, and L. Szymanowski. *Eur. Phys. J.* **C4***:93*, 1998.

[90] M. G.Ryskin. *Eur. Phys. J.* **C2***:239*, 1998.

[91] J. Bartels, L. N. Lipatov, and G. P. Vacca. *Phys. Lett.* **B477***:178*, 2000.

[92] M. Wirbel, B. Stech, and M. Bauer. *Z. Phys.* **C29***:637*, 1985.

[93] M. L. Perl. *High Energy Hadron Physics.* John Wiley & sons, 1973.

[94] H. M. Pilkuhn. *Relativistic Particle Physics.* Springer Verlag, 1979.

Acknowledgement

After four years of work (five including my diploma thesis) there is a host of people whom I owe gratitude, and I want to apologise right here if I have forgotten anyone. To name only a few, I want thank cordially:

- Prof. Karlheinz Meier for the interesting topic he offered and the opportunity to work on it. It has always been a pleasure to have the freedom to the research in my way, combined with his clever and wise guidance that has never lost the aim out of sight.
- And of course I want to thank Prof. Hans Günter Dosch for being so kind to take over the task to referee this thesis and for all the interesting, illuminating and helpful discussions we have had over the last two years.
- Dr. Jürgen Stiewe's endless supply of critical thoughts and questions combined with fruit gums (also of endless supply) have always been a great help, and all of it is gratefully acknowledged. I am deeply in debt for all what I have learned in his office in physics as well outside physics.
- Dr. Selvam Dhamotharan for his critical blink over my shoulder and "Was macht die Analyse?". It was a pleasure, a great help and a lot of fun to have him next door.
- Christoph von Cube and Tobias Golling, with whom I shared only the year of their Diploma theses, what is for sure not enough! Thanks, it's been a great time.
- Dr. Claus Beier, Dr. Martin Swart and Dr. Oliver Nix who willingly shared their knowledge, experience and wisdom. Thank you all for the good atmosphere in which we lived/worked.
- Dr. Richard Cavanaugh who left much too early.
- Kaffee-Runde: Elke Grimm, Irmtraut Spinnler, Lothar Voerg, Beatrice Bähr, Robert Weis, Frau Pieper, Prof. Kluge, Prof Putzer, ... thank you all for this institution in this institute and to fill it up with life and personal warmth.
- All the former PhD- and Diploma students of both the H1- and the Aleph(Atlas) group with whom I had the pleasure to have a nice time.
- Of course, I don't want to forget all at Philosphenweg 12 with whom I had the chance to work together, or just to get to know.
- Peter, Wolfgang, Steffen and Christoph for delightful and adventurous evenings full of might and magic.

- Gerd for the patience on Sunday evenings when he had to endure endless lessons on stuff he didn't bother about.
- And a great part of my mental health I owe my Volleyball team, naming in particular Marcus, Alex and Uwe, and the rest of course.
- My parents, for all (too much to give proper account of).
- Maren, for all the good times so far and still to come.

. . . and of course all the rest whom I have forgotten to mention.